NTNU
Norwegian University of
Science and Technology

Nonlinear Wave Loads on a Vertical Cylinder

Dennis Hallås Fimland

Marine Technology
Submission date: July 2018
Supervisor: Trygve Kristiansen, IMT

Norwegian University of Science and Technology
Department of Marine Technology

This page is intentionally left blank

Preface

This Master Thesis is inspired by the challenge left by Trygve Kristiansen and Odd Magnus Faltinsen, in their paper ***Higher harmonic wave loads on a vertical cylinder in finite water depth***, to develop an efficient and accurate load model capable of capturing viscous flow effects. The present report presents my work conducted during the spring and summer of 2018 to fulfill the graduation requirement at the Norwegian University of Science and Technology, Trondheim.

The work has been challenging yet rewarding. A considerable amount of time has been dedicated to understanding and implementing the Vortex-In-Cell algorithm. Working on the Vortex-In-Cell solver taught me a lot about numerical methods as well as general programming, how fun it can be, but also how hard it is to create a code without bugs. The latter I have yet to achieve. In addition, the work has given me greater insight into the complex nature of the interaction of waves and marine units, a topic I find quite interesting.

I would like to express my greatest gratitude to Trygve Kristiansen for his excellent guidance and support during this project. I consider myself lucky to have such a dedicated and knowledgeable supervisor. I also wish to thank my fellow students at office A1.007 for all the support and motivation you have given me this last year of our studies.

Finally, I want to direct special appreciation towards my good friends Håvard Ola Eggen, Christoffer Skjulstad and Erlend Flatøy for all your help and for all the joy you have brought into my life.

I hope you enjoy your reading

Trondheim, July 26, 2018

Dennis Fimland

Abstract

Several authors have indicated discrepancies in the third load harmonic obtained by the inviscid FNV theory for computing higher order wave loads on vertical, non-moving, surface-piercing circular cylinders. The present master thesis investigates if these discrepancies may be explained by the occurrence of local flow separation along the cylinder axis.

The generalized FNV theory is modified to account for viscous effects, by replacing the linear forcing term with a viscous force term computed using a simplified numerical model assuming the cross-flow principle to be valid. To reduce the computational cost related to the numerical solution of the two-dimensional Navier-Stokes and continuity equations, the governing equations are restated in terms of the stream function and vorticity transport equation and solved using the mixed Eulerian-Lagrangian Vortex-In-Cell method in combination with the Operator Splitting Technique.

Computations of the horizontal wave forces acting on a circular cylinder is carried out for wave conditions where the third harmonic of the FNV theory is known to deviate from experimental results. The computed load harmonics of the horizontal wave load are compared to estimates obtained by the generalized FNV theory and experimental measurements. Results of the three first harmonics are presented, while the main focus is on the amplitude of the third load harmonic. The computed third harmonic is shown to be in good agreement with both the FNV theory and empirical data for short waves. For longer waves the numerically predicted harmonics are in general smaller than the theoretical predictions. However, the numerical results overpredict the third harmonic for the steepest wave conditions tested compared to the experimental data. Thus flow separation alone seems not to explain the discrepancies in the FNV model.

Sammendrag

Sammenlikning av eksperimentelle målinger og analytiske modeller av ikke-lineære bølgelaster på sirkulære sylindere, som er festet til havbunnen og penetrerer den frie overflaten, har vist at den tredje harmoniske lastkomponeten overpredikeres av FNV teorien. Denne masteroppgaven undersøker om separasjon lokalt langs sylinderaksen er opphavet til dette avviket.

Den generaliserte FNV teorien modifiseres slik at den tar høyde for viskøse effekter. Dette utføres ved å erstatte det lineære lastleddet i FNV teorien med et forenklet viskøst lastledd. Ved å neglisjere stømninger langs sentralaksen til sylinderen, kan de viskøe kreftene beregnes ved å anvende den todimensjonale versjonen av Navier-Stokes likninger og kontinuitetslikningen. For å redusere beregningstiden benyttes en Eulersk-Lagrange metode kalt Vortex-In-Cell sammen med den matematiske teknikken Operator Splitting Technique.

Beregninger av horisontale bølgelaster blir utført for sjøtilstander hvor det har blitt observert at den generaliserte FNV teorien overpredikerer den tredje harmoniske lastkomponenten. De beregnede lastene sammenliknes med analytiske estimater og eksperimentelle målinger. Beregniger av de tre første lastkomponentene presenteres i denne oppgaven, men det fokuseres på amplituden av den tredje harmoniske lastkomponenten. Resultatene viser at den sistnevnte lastkomponenten samsvarer meget bra med både analytiske og eksperimentelle data når de innkommende bølgene er korte. For lengre bølger gir den modifiserte FNV teorien lavere estimater på samtlige lastkomponenter sammenliknet med de analytiske resultatene. Sammenliknet med eksperimentelle målinger overpredikerer den modifiserte FNV teorien den tredje harmoniske lastkomponenten når de innkommende bølgene ble tilstrekkelig steile. Resultatene indikerer dermed at avvikene i den analytiske FNV modellen ikke kun kan forklares ved separasjon.

Contents

Nomenclature

Abbreviations

CFD	Computational Fluid Dynamics
CPU	Central Processing Unit
FNV	Faltinsen, Newman and Vinje
OST	Operator Splitting Teqnuice
RAM	Random Accses Memory
RMS	Root Mean Square
VIC	Vortex-In-Cell

Main symbols

β	Stokes parameter
$\Delta\theta$	Cell size in θ-direction
$\Delta\tilde{t}$	Dimensionless time step
Δr_1	Thickness of the cells at the cylinder surface
Δt	Time step
Δz_i	Thickness of the i^{th} strip of the cylinder
Γ	Circulation

Λ	Scaling ratio
ν	Kinematic viscosity
ω	Angular frequency
ϕ	Velocity potential
ϕ_D	Linear diffraction potential
ϕ_I	Incident wave potential
ϕ_S	Linear scattering potential
Ψ	Nonlinear scattering potential
ψ	Stream function
ρ	Density of water
$\tilde{t}$	Dimensionless time
$\vec{u}$	Velocity vector
ξ	Vorticity
ζ_{a1}	Wave amplitude to first order
ζ_a	Wave amplitude
ζ_{Crest}	Distance from the sea floor to the wave crest
ζ_I	Surface elevation
ζ_{Trough}	Distance from the sea floor to the wave trough
a	Cylinder radius
C_D	Drag coefficient
$C_{F_{RMS}}$	Dimensionless root mean square value of the in-line force
C_{F_x}	Dimensionless in-line force
C_M	Inertia coefficient
D	Cylinder diameter

Fn	Froude number
F^1	Wave force predicted by the asymptotic Morisons equation
F^2	Non-linear wave force due to the linear diffraction potential ϕ_D
F^Ψ, F^3	Wave force due to the nonlinear scattering potential Ψ
F_D	Drag force
F_I	Inertia force
F_i	In-line force on the i^{th} strip
$F_{p,x}$	In-line pressure force
$F_{s,x}$	In-line shear force
F_{VIC}	Total in-line force computed with the Vortex-In-Cell program
F_x	Total in-line force
$F_x^{(i\omega)}$	i^{th} harmonic of the in-line force
g	Acceleration of gravity
H	Wave height
h	Water depth
H_1	Wave height according to first order wave theory
k	Wave number
KC	Keulegan-Carpenter number
L	Wave length
M	Number of grid points
N_θ	Number of nodes in the azimuthal direction
N_r	Number of nodes in the radial direction
n_t	Number of time steps each flow cycle
N_v	Number of vortex particles

P	Pressure
r, θ	Polar coordinates
$R\text{e}$	Reynolds number
$r^{'}, \theta$	Modified polar coordinate system
r_o	Domain size
T	Wave period
t	Time
T_w	Period of mono-harmonic oscillatory flow
U	Outer flow velocity
u, v, w	Velocity components in Cartesian coordinates
$U\text{r}$	Ursell number
U_o	Velocity amplitude of oscillatory flow
x, y, z	Cartesian coordinates

Chapter 1

Introduction

1.1 Motivation

Wind energy has so far been one of the most used sources of renewable energy, mainly by means of onshore installations. However, the seemingly endless free area at sea and better wind conditions have driven the wind industry offshore the last decade.

One of the main disadvantages of offshore wind is the high cost related to the construction and operation of such installations. Compared with onshore wind farms, which are already are less cost-efficient than conventional sources energy (Heptonstall (2007)), offshore installations have an even higher cost per megawatt produced. The main difference between onshore and offshore installations is the environmental condition in which they operate, as offshore installation are subjected to complex hydrodynamic loads.

At present and in the foreseeable future, see Figure 1.1, most offshore wind turbines are mounted on bottom fixed structures in shallow or intermediate water depth. Among them, monopiles and gravity based substructures are the most commonly used offshore foundations. The first natural period of such structures is typically around 4 seconds. In Ultimate Limit Stats conditions, peak wave periods are typically in the range of 10-15 seconds. This means that higher order loads become important as they may excite response at the eigen period of the wind turbine. Wave load models which accurately describe such loads will therefore be an essential tool in the further development of the offshore wind industry.

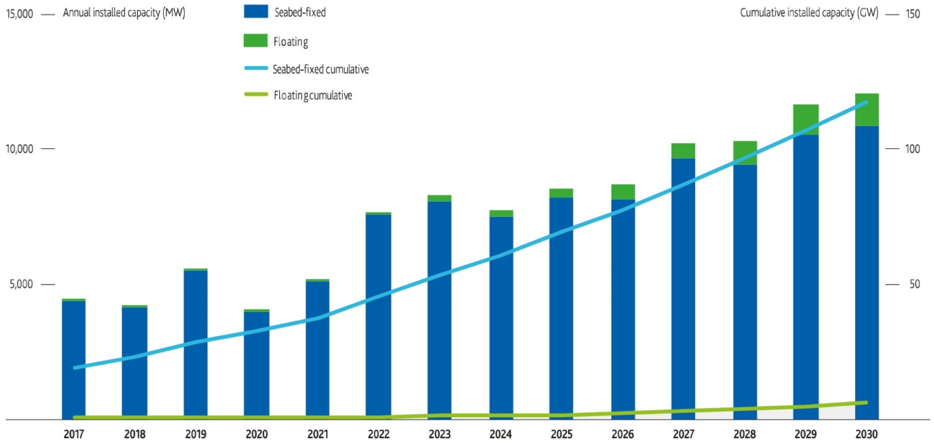

Figure 1.1: Projecions for offshore wind development globally out to 2030 (GWEC (2017)).

1.2 Ringing

Experiments have shown that large diameter monopile support structures for offshore wind turbines are susceptible to transient structural deflections at frequencies substantially higher than the incident wave frequencies in severe seas (Suja-Thauvin et al. (2017); Bachynski et al. (2017)). This phenomenon is often referred to as ringing, and it is characterized as a transient response vibration following a high, steep wave as illustrated in Figure 1.2 (Faltinsen et al. (1995)). This behavior can not be explained by traditional wave diffraction theories, as presented by C. MacCamy and A. Fuchs (1954), nor the Morison equation (Morison et al. (1950)). Many efforts have thus been made to explain the rationale behind since the phenomenon was first observed in the late 1980s and early 1990s (Natvig and Teigen (1993)).

Faltinsen et al. (1995) (FNV) presented analytic expressions of the forces acting on a non-moving, circular cylinder in deep water incident waves. A perturbation expansion in both wave number and wave slope was used leading to terms of up to third order. Kristiansen and Faltinsen (2017) generalized the FNV method to finite water depth. Another approach was presented by Malenica and Molin (1995). Applying the standard perturbation approach, they developed a complete third-order diffraction model for a fixed cylinder in finite water depth. Both of the methods mentioned above are based on the classical assumptions of inviscid, incompressible and irrotational fluid flow. Thus neglecting the effect of flow separation.

Numerous authors have during the last two decades presented experimental results of ringing. There are in particular two phenomena which have gained a lot of attention. One is the so-called secondary load cycle which occurs in steep waves and was first observed by Grue et al. (1993). The phenomenon is characterized by a distinct load peak right after the main load peak with a duration of about one-fifth to one-sixth of the wave period. The second phenomenon is a local run-up at the rear face of the cylinder, which occurs as a large wave passes the cylinder, as illustrated in Figure 1.3. The occurrence of this rear run-up was first described by Chaplin et al. (1997). Attempts by Kristiansen and Faltinsen (2017) to visualize the local rear run-up using confetti, made it clear that an upwelling from below causes the phenomenon. It is thus believed that the rear run-up originates from a high-pressure zone behind the cylinder due to flow separation.

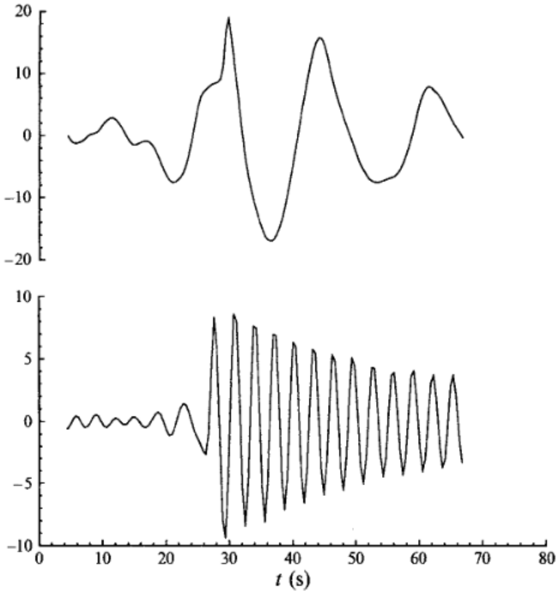

Figure 1.2: Example of the occurrence of ringing on a tension-leg platform as a steep wave passes the platform. The upper curve shows the time history of the surface elevation, while the lower shows the measured tension at the eigen frequency of the structure (Faltinsen et al. (1995)).

Figure 1.3: Example of water run-up behind the cylinder as a wave crest passes (Kristiansen and Faltinsen (2017)).

Discrepancies between experimental and analytical forces obtained on monopiles in long and steep waves have also been noted by several authors. Experimental measurements of the in-line force on a vertical cylinder in deep water was carried out by Huseby and Grue (2000). Results showed that the FNV model gave a reasonable prediction of the first and second harmonic. However, the results indicated that the phasing and amplitude of the third harmonic were incorrect. Kristiansen and Faltinsen (2017) showed that the predicted forces and moments from the generalized FNV model was in good agreement with experiments, both regarding phase and amplitude, for small to medium steep waves. Noticeable discrepancies in the third load harmonic were observed as the wave steepness exceeded a distinct limit. This was attributed to the onset of flow separation along the cylinder axis.

1.3 Scope

This thesis examines the effect of flow separation on higher harmonic wave loads on large diameter monopile in steep regular wave conditions. The main objective is to investigate if a simplified numerical model based on the two-dimensional Navier-Stokes equations, using a strip theory approach and assuming the cross-flow principle, can explain the discrepancies in the third load harmonic of the horizontal wave load obtained by the generalized FNV theory. To keep the computational cost low, viscous forces should be obtained using the Vortex-In-Cell method.

1.4 Report Structure

The first part of this thesis will present the theoretical background relevant to the thesis. First, different aspects of flow past two-dimensional circular cylinders are considered in Chapter 2. The reaming part of the chapter presents different regular wave theories and wave force models, focusing on Stokes perturbation theory and the generalized FNV theory. A brief outline is provided for both theories. Chapter 3 covers the theoretical foundation and the implementation of the Vortex-In-Cell method. This chapter will also present numerical results for a two-dimensional cylinder in impulsively started and planar oscillatory flows. The results are compared to experimental data and existing numerical results. The combined VIC-FNV method is presented in Chapter 4. Some comments to the test conditions are also given. The results are presented in Chapter 5. The horizontal wave force obtained by the combined VIC-FNV method are compared to experimental measurements and the generalized FNV theory. Concluding remarks are presented in Chapter 6.

Chapter 2

Theory

2.1 Flow around two-dimensional cylinders

Flow past two-dimensional cylinders with circular cross-section is a widely studied subject in research due to its practical importance in engineering application on typical marine structures exposed to waves and currents. In this section, some aspects of such flows are presented.

2.1.1 Flow separation

All solid objects traveling through a viscous fluid acquire a layer close to the surface associated with viscous flow effects, usually referred to as the boundary layer. The thickness of this layer is often defined as the normal distance from the wall to a point where the tangential velocity is 99% of the local free stream velocity (White (2006)). Shear stress caused by viscosity has a retarding effect on the fluid, within the boundary layer. This may be overcome if there is a negative, favorable, pressure gradient along the body contour, while a positive, adverse, pressure gradient increase the local retardation of the flow.

Whether the local pressure gradient is positive or negative is determined by the curvature of the body. In the case of a circular cylinder we have a favorable pressure gradient on the side facing the incoming flow. The negative pressure gradient will counteract the retarding effect of viscosity and the local velocity profile is preserved. The pressure gradient gradually change along the cylinder surface and at one point

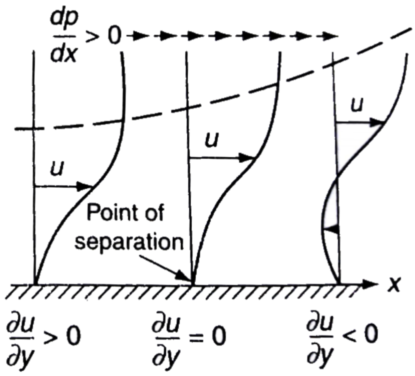

Figure 2.1: Effect of adverse pressure gradient (White (2006)).

the pressure gradient changes sign. Thus we get an adverse pressure gradient, slowing down the wall flow and the boundary layer thickens as illustrated in Figure 2.1. Further retardation of the fluid brings the shear stress at some point to zero. This is known as the separation point. From this point onwards the fluid velocity close to the wall changes sign, moving upstream, and a region of recirculating flow develop. The flow does no longer follow the body contour, thus we say that the flow has separated. In general, the flow separates more easily in laminar than in turbulent boundary layers. The reason for this is that the smaller eddies cause a net momentum flux from the free stream to the boundary layer, thus increasing the wall velocity.

2.1.2 Forces on a cylinder in uniform current

The total in-line force acting on a cylinder in a uniform current originate from two terms. A pressure force, due to local pressure variations along the surface of the cylinder, and a friction force, due to the viscous shear stresses within the boundary layer. The total force in the flow direction is simply found as the sum of these two contributions, $F_x = F_{p,x} + F_{s,x}$.

The total force F_x is usually presented in terms of a dimensionless force coefficient, C_{F_x}, defined as

$$C_{F_x} = \frac{F_x}{\frac{1}{2}\rho U^2 D} \tag{2.1}$$

in which D is the cylinder diameter, ρ is the density of the ambient fluid and U is the flow velocity past the cylinder.

2.1.3 Forces on cylinders in oscillatory flows

The in-line forces on cylinders in oscillatory flow are usually decomposed into two terms, an inertia part proportional to the acceleration, and a drag part proportional to velocity squared in the following manner

$$\begin{aligned} F_x &= F_I + F_D \\ F_x &= \rho \frac{\pi D^2}{4} C_M \frac{\partial U}{\partial t} + \frac{\rho}{2} C_D D |U| U \end{aligned} \tag{2.2}$$

where F_I and F_D is the inertia and drag force respectively. The non-dimensional inertia and drag coefficient C_M and C_D depends on both the Keulegan-Carpenter Number $K\mathrm{C}$ and the Reynolds number $R\mathrm{e}$ as illustrated in Figure 2.2. These non-dimensional numbers are defined as

$$K\mathrm{C} = \frac{U_o T_w}{D} \tag{2.3}$$

$$R\mathrm{e} = \frac{U_o D}{\nu} \tag{2.4}$$

where U_o and T_w are the flow velocity amplitude and period respectively, ν is the kinematic viscosity. Equation 2.2 is formally known as the Morison equation and was first proposed by Morison et al. (1950).

The ratio between the maximum of the two terms on the right hand side of equation 2.2 can be expressed as

$$\frac{F_{I_{Max}}}{F_{D_{Max}}} = \frac{\rho \frac{\pi^2}{2} C_M D^2 U_o}{\rho \frac{1}{2} C_D D U_o^2 T_w} = \frac{\pi^2}{K\mathrm{C}} \frac{C_M}{C_D} \tag{2.5}$$

At small values of $K\mathrm{C}$, C_M may be taken as $C_M = 2$, see Figure 2.2b, while C_D is approximately equal to 1. Thus equation 2.5 gives

$$\frac{F_{I_{Max}}}{F_{D_{Max}}} \propto \frac{20}{K\mathrm{C}} \tag{2.6}$$

This means that for small $K\mathrm{C}$ numbers, the inertia term of the in-line forces dominates and the drag term may be neglected. However, at larger values of $K\mathrm{C}$, viscous effects such as flow separation become more pronounced, and the drag term become increasingly important.

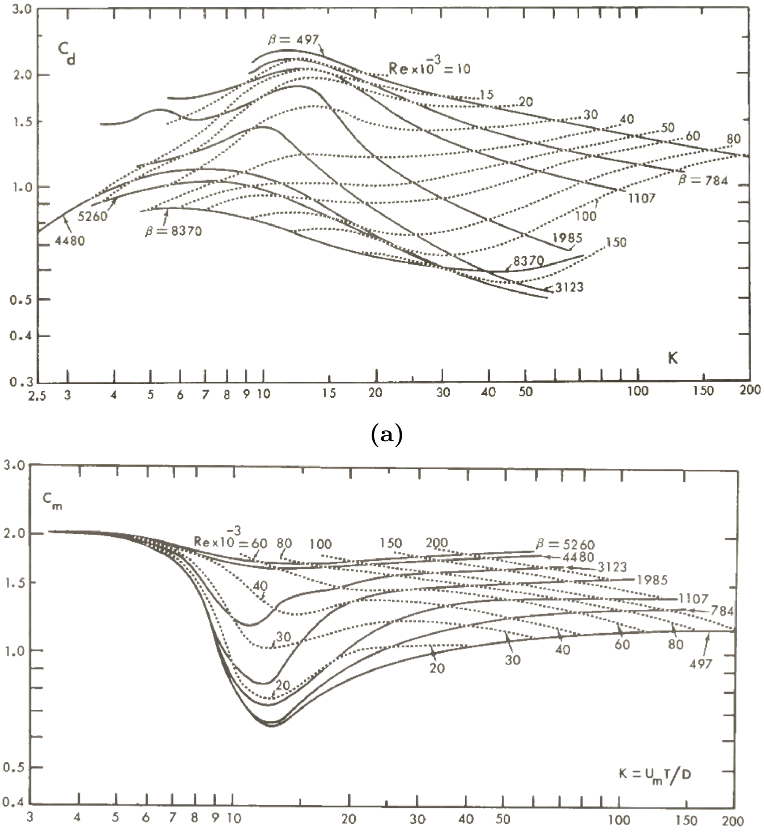

(a)

(b)

Figure 2.2: Drag (a) and inertia (b) coefficients dependence on Re and KC for a smooth circular cylinder (Sarpkaya (1976)).

2.1.4 Force coefficients

When decomposing the in-line forces according to the Morison equation, the hydrodynamic problem reduces to obtain suitable values of C_M and C_D. As equation 2.2 does not account for the wake behavior, history of the flow, nor the frequency at which the flow oscillates. Such effects must therefore be entirely accounted for by the two force coefficients.

For smooth cylinders in planetary oscillatory flow, it is possible to obtain analytical expressions for the two force coefficients as a function of the parameters

KC and the the Stokes parameter β, defined in equation 2.7.

$$\beta = \frac{Re}{K\mathrm{C}} = \frac{D^2}{\nu T_w} \tag{2.7}$$

One such solution was presented by Wang (1968) of order $\mathcal{O}((\pi\beta)^{-3/2})$. However, these expressions are only valid for small values of KC. Thus C_M and C_D must, in general, be obtained from numerical simulations of the Navier-Stokes equations or experiments. The two coefficients are usually calculated from the time history of the in-line force, F_x, by applying a standard Fourier averaging process. For an oscillatory flow represented by $U = U_o \sin(\omega t)$, this is performed according to equation 2.8 and 2.9 (Sarpkaya (1976)).

$$C_D = \frac{1}{\frac{1}{2}\rho U_o^2 D} \frac{3\omega}{8} \int_0^{T_w} F_x \sin \omega t dt \tag{2.8}$$

$$C_M = \frac{1}{\frac{1}{2}\rho U_o^2 D} \frac{K\mathrm{C}\omega}{\pi^3} \int_0^{T_w} F_x \cos \omega t dt \tag{2.9}$$

Here, ω is the angular frequency.

For $\beta < 1000$ the drag coefficient initially decrease with KC until a certain minimum. The inertia coefficient remains almost constant, approximately equal to 2, in the same region. The theory by Wang is in good agreement with experimental data obtained by Bearman et al. (1985) as the KC number is sufficiently low. However, as KC reach a value of about 2, the experimental data suddenly deviate from the theoretical results. For higher values of β, the experiments carried out by Sarpkaya (1986) indicated that the theoretically predicted C_D diverge from the experimental results at smaller values of KC. The discrepancies becoming larger as β increases. This was credited to the onset of three-dimensional instabilities, known as Honji instabilities (Honji (1981)), which leads to the formation of periodic vortex structures along the cylinder axis. In the higher KC range, $2 \lesssim K\mathrm{C} \lesssim 12$, C_D was found to be directly proportional to the KC number, while C_M decreased with increasing KC.

Another important characteristic of in-line force is the root mean square (RMS) value. The dimensionless RMS of the in-line force, denoted $C_{F_{RMS}}$, is computed similarly to the drag and inertia coefficients by evaluating the integral given by

Sarpkaya (1976) as

$$C_{F_{RMS}} = \frac{1}{T_w} \int_0^{T_w} \frac{F_x^2}{(\frac{1}{2}\rho D U_o^2)^2} dt \tag{2.10}$$

2.2 Regular wave theory

An important aspect when evaluating wave loads on marine structures is how one chose to describe the waves kinematics. This section provides the basic knowledge of regular water waves needed to evaluate such loads.

2.2.1 The boundary value problem

Sea water may be assumed to be a perfect fluid, with the fluid motion being irrotational. Thus, the flow can be described by the Laplace equation for a velocity potential ϕ, in equation 2.11, which must hold throughout the fluid (Faltinsen (1990)).

$$\nabla^2 \phi = 0 \tag{2.11}$$

Here ∇ denotes the del operator. To solve equation 2.11, one must provide boundary conditions for ϕ everywhere along the boundaries of the flow field of interest, as illustrated in Figure 2.3. At the free surface both the surface elevation ζ_I and the potential function ϕ are unknown, therefore requiring two boundary conditions. The two conditions enforced on the free surface are formally known as the dynamic and kinematic free surface conditions and are a consequence of no change in pressure and no flow across the fluid interface, respectively. The latter of the two may be expressed as

$$\frac{\partial \zeta_I}{\partial t} = \frac{\partial \phi}{\partial z} - \nabla\phi \cdot \nabla\zeta_I, \qquad z = \zeta_I \tag{2.12}$$

while the dynamic free surface condition is

$$\frac{\partial \phi}{\partial t} + \nabla\phi \cdot \nabla\phi + g\zeta_I = 0, \qquad z = \zeta_I \tag{2.13}$$

Taking the time derivative of equation 2.13 and introducing equation 2.12, equation

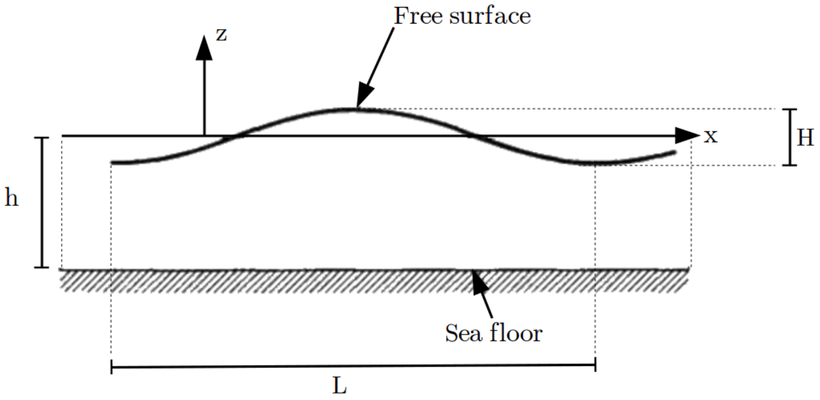

Figure 2.3: Illustration of the boundary value problem, the Cartesian coordinate system, water depth h, wave height H and wave length L.

2.14, known as the combined free surface boundary condition, can be obtained.

$$\frac{\partial^2 \phi}{\partial t^2} + g\frac{\partial \phi}{\partial z} + 2\nabla\phi \cdot \nabla\frac{\partial \phi}{\partial t} + \frac{1}{2}\nabla\phi \cdot \nabla\Big(\nabla\phi \cdot \nabla\phi\Big) = 0, \qquad z = \zeta_I \tag{2.14}$$

Finally, for waves propagating over a horizontal sea floor, the kinematic bottom boundary condition states that the sea floor is impermeable and thus the vertical fluid velocity has to be zero along the sea bed, according to equation 2.15.

$$\frac{\partial \phi}{\partial z} = 0, \qquad z = -h \tag{2.15}$$

2.2.2 Linear wave theory

With the combined free surface condition (eq. 2.14), one does not know where the free surface is before the problem is solved. However, by linearizing the free surface condition, we are able to simplify the problem and still get an adequate description of the surface waves in most cases. The linearized free surface condition, equation 2.16, is obtained by Taylor expansion of equation 2.14 around the mean free surface, only including the linear terms.

$$\frac{\partial^2 \phi}{\partial t^2} + g\frac{\partial \phi}{\partial z} = 0, \qquad z = 0 \tag{2.16}$$

Solving the linearized boundary value problem, we obtain a velocity potential proportional to the wave amplitude ζ_a valid up to the mean free surface. The use of linear wave theory (Airy waves) is in general justified when the wave amplitude is small. Consistent with linear theory the wave kinematics may be extrapolated above the mean free surface by a zeroth order approximation, e.i. all properties are assumed to be constant above $z = 0$. However, in extreme sea states, the discrepancies of linear theory become more pronounced, especially in the free surface zone. Thus in order to accurately predict the wave loads in such sea states more sophisticated wave models are needed.

2.2.3 Stokes wave theory

In Stokes wave theory, the exact solution of the boundary value problem is approximated using a so called perturbation series approach. The series expansions are in terms of a small perturbation parameter ϵ, which according to the original Stokes theory equals the wave steepness $k\zeta_{a1}$, where k is the wave number and ζ_{a1} is the wave amplitude to first order. Thus, the velocity potential ϕ and surface elevation ζ_I can be expressed on the form

$$\phi = \epsilon\phi_1 + \epsilon^2\phi_2 + \epsilon^3\phi_3 + ... \tag{2.17}$$

$$\zeta_I = \epsilon\zeta_1 + \epsilon^2\zeta_2 + \epsilon^3\zeta_3 + ... \tag{2.18}$$

The combined free surface boundary condition apply at the yet unknown free-surface elevation. To resolve this problem, a Taylor series expansion of the free surface condition in the vertical direction is performed about the mean free surface $z = 0$. The Taylor development of a function f, evaluated at $z = \zeta_I$, taken around $z = 0$ is given in equation 2.19 below.

$$f(x,\zeta,t) = f\Big|_{z=0} + \zeta_I \frac{\partial f}{\partial z}\Big|_{z=0} + \frac{\zeta_I^2}{2!}\frac{\partial^2 f}{\partial z^2}\Big|_{z=0} + \frac{\zeta_I^3}{3!}\frac{\partial^3 f}{\partial z^3}\Big|_{z=0} + ... \tag{2.19}$$

Carrying out the Taylor expansion on the combined free surface condition, equation 2.14, yields

$$\begin{aligned} \frac{\partial^2\phi}{\partial t^2}\Big|_{z=0} + g\frac{\partial\phi}{\partial z}\Big|_{z=0} + \zeta_I\Big(\frac{\partial^3\phi}{\partial z\partial t^2}\Big|_{z=0} + g\frac{\partial^2\phi}{\partial z^2}\Big|_{z=0}\Big) + \\ 2\nabla\phi\nabla\frac{\partial\phi}{\partial t}\Big|_{z=0} = 0 \qquad z = 0 \end{aligned} \tag{2.20}$$

showing terms up to double products of ζ_I and ϕ, representing the Stokes expansion up to second order. By further introducing the series expansion given in equation

2.17 and 2.18 we get

$$\begin{aligned}&\epsilon\Big\{\frac{\partial^2\phi_1}{\partial t^2}\Big|_{z=0}+g\frac{\partial\phi_1}{\partial z}\Big|_{z=0}\Big\}+\epsilon^2\Big\{\frac{\partial^2\phi_2}{\partial t^2}\Big|_{z=0}+g\frac{\partial\phi_2}{\partial z}\Big|_{z=0}+\\&\zeta_1\Big(\frac{\partial^3\phi_1}{\partial z\partial t^2}\Big|_{z=0}+g\frac{\partial^2\phi_1}{\partial z^2}\Big|_{z=0}\Big)+2\nabla\phi_1\nabla\frac{\partial\phi_1}{\partial t}\Big|_{z=0}\Big\}+\mathcal{O}(\epsilon^3)=0\qquad z=0\end{aligned}\tag{2.21}$$

Introducing the series expansion of ϕ into the Laplace equation (eq. 2.11) and the bottom boundary condition (eq. 2.15) we obtain the following expressions

$$\epsilon\nabla^2\phi_1+\epsilon^2\nabla^2\phi_2+...=0\tag{2.22}$$

$$\epsilon\frac{\partial\phi_1}{\partial z}\Big|_{z=-h}+\epsilon^2\frac{\partial\phi_2}{\partial z}\Big|_{z=-h}+...=0\tag{2.23}$$

The nonlinear boundary value problem has now been restated onto an infinite set of linear equations. One for each order of ϵ. Gathering all terms that depend on ϵ the linear boundary value problem is obtained, while the terms proportional to ϵ^2 yields the boundary value problem for the second order correction term. In general, the n^{th} order solution will depend on the solution of order n-1, creating a hierarchy of equations which must be solved from lower to higher order. As a rule of thumb, the accuracy of the velocity potential increases as more terms are added in the perturbation expansion of ϕ and ζ_I.

2.2.4 Fifth order Stokes wave

The procedure described in Section 2.2.3 may, in principle, be used to derive Stokes waves of any order. But as more terms are added in the of series of ϕ and ζ_I the extent of calculations increases dramatically. Still, a fifth order theory was derived by Skjelbreia and Hendrickson (1960). The assumption on which the derivation is based is that both the velocity potential and surface profile can be described as trigonometric series. This leads to the following expression for the velocity potential

$$\phi=\frac{c_\omega}{k}\sum_{n=1}^{5}D_n\cosh(nk(h+z))\sin(n(kx-\omega t))\tag{2.24}$$

where c_ω is the wave celerity given by

$$c_\omega=\frac{\sqrt{C_0^2(1+\lambda^2C_1+\lambda^4C_2)}}{k}\tag{2.25}$$

The surface elevation has the following form

$$\zeta_I = \frac{1}{k}\sum_{n=1}^{5} E_n \cos(n(kx-\omega t)) \tag{2.26}$$

The coefficients D_n and E_n are introduced for convenience and are defined in Table 2.1.

Table 2.1: Definition of the coefficients D_n and E_n

n	D_n	E_n
1	$\lambda A_{11} + \lambda^3 A_{13} + \lambda^5 A_{15}$	λ
2	$\lambda^2 A_{22} + \lambda^4 A_{24}$	$\lambda^2 B_{22} + \lambda^4 B_{24}$
3	$\lambda^3 A_{33} + \lambda^5 A_{35}$	$\lambda^3 B_{33} + \lambda^5 B_{35}$
4	$\lambda^4 A_{44}$	$\lambda^4 B_{44}$
5	$\lambda^5 A_{55}$	$\lambda^5 B_{55}$

The coefficients A_{ij} B_{ij} and C_i are functions of the ratio of the water depth to wave length, h/L, only and can be found in the original paper by Skjelbreia and Hendrickson (1960). It should be noted that the original expression for C_2, the factor +2592 must be replaced with −2592, as pointed out by Fenton (1985). Since the wave height H, the water depth h and the wave period T is assumed to be known, the only unknowns are the wave length L and the coefficient λ. These are found form the simultaneous solution of equation 2.27 and 2.28.

$$\frac{2\pi h}{gT^2} = \frac{h}{L}\tanh\left(\frac{2\pi h}{L}\right)\left(1+\lambda^2 C_1 + \lambda^4 C_2\right) \tag{2.27}$$

$$\frac{\pi H}{h} = \frac{L}{h}\left(\lambda + \lambda^3 B_{33} + \lambda^5\left(B_{35}+B_{55}\right)\right) \tag{2.28}$$

Here g is the acceleration of gravity. When L and λ are known the wave celerity is obtained from equation 2.25 and the wave number is found from equation 2.29.

$$k = \frac{2\pi}{L} \tag{2.29}$$

Differentiation of 2.24, yields the following expressions for the horizontal and vertical velocity components in equation 2.30 and 2.31.

$$u = \frac{\partial \phi}{\partial x} = c_w \sum_{n=1}^{5} n D_n \cosh(nk(h+z)) \cos(n(kx - \omega t)) \tag{2.30}$$

$$w = \frac{\partial \phi}{\partial z} = c_w \sum_{n=1}^{5} n D_n \sinh(nk(h+z)) \sin(n(kx - \omega t)) \tag{2.31}$$

Further derivation of the above equations yields the following formulas for the horizontal particle acceleration, horizontal velocity gradient and vertical velocity gradient in equation 2.32, 2.33 and 2.34 respectively.

$$\frac{\partial u}{\partial t} = c_w \omega \sum_{n=1}^{5} n^2 D_n \cosh(nk(h+z)) \sin(n(kx - \omega t)) \tag{2.32}$$

$$\frac{\partial u}{\partial x} = -c_w k \sum_{n=1}^{5} n^2 D_n \cosh(nk(h+z)) \sin(n(kx - \omega t)) \tag{2.33}$$

$$\frac{\partial w}{\partial z} = c_w k \sum_{n=1}^{5} n^2 D_n \cosh(nk(h+z)) \sin(n(kx - \omega t)) \tag{2.34}$$

2.2.5 Comments to higher order Stokes waves

Dean (1991) discusses the importance of the Ursell parameter, defined in equation 2.35, in connection with finite amplitude Stokes waves.

$$U\mathrm{r} = \frac{HL^2}{h^3} \tag{2.35}$$

An example of its importance was illustrated by studying the curvature at the wave trough predicted by second order Stokes wave theory. At large values of $U\mathrm{r}$ it was shown that a secondary crest occurred in the theoretical predicted trough, due to the largeness of the second order term. Under these conditions the assumption that the second order term is much smaller then the corresponding first order term is no longer valid. The advent of a secondary wave crest is not limited to second order Stokes theory but may appear in any higher order Stokes solution (Hedges (1995)). Thus, higher order Stokes theory should be used only when $U\mathrm{r}$ is sufficiently small.

Fenton (1990) performed a comparative study between fifth order Stokes theory and the more accurate Fourier solution. As a measure of accuracy, he used the integrated value of the horizontal particle velocity underneath the wave crest. From his analysis he proposed equation 2.36 as an upper limit for the Stokes theory.

$$\frac{L}{h} = 21.5e^{-1.87H/h} \tag{2.36}$$

Using the findings of Fenton (1990), Hedges (1995) showed that $U\mathrm{r} = 40$ is a better approximation of the upper limit for the application of Stokes waves.

Provided that the wave length is less than two times the water depth the Ursell number is of minor importance. In deep waters, the validity of Stokes wave theory is limited by the wave steepness H/L, due to the occurrence of wave breaking.

Figure 2.4 indicates the approximate regions in which various analytical wave theories may be regarded as valid. Note that the boundary between linear and Stokes higher order theories for deep water has been assumed to apply for intermediate water depth. This need not be true. The sea states used in the current analysis of wave loads on large monopile support structures consists of steep, non-breaking waves in deep and intermediate water. The use of fifth order Stokes wave may be justified according to Figure 2.4, which will be further discussed.

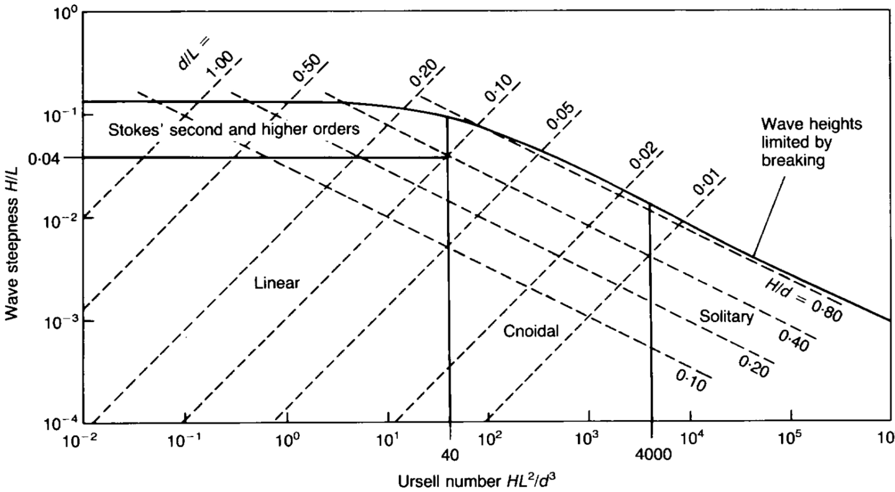

Figure 2.4: Validity of different wave motion models with respect to the wave steepness and the Ursell number in deep waters (Hedges (1995)).

2.3 Wave forces

All marine units, whether floating or fixed to the sea floor, are subjected to wave forces, and therefore these forces are of central interest to naval engineers. There are in principle three approaches to solve this problem. The first approach is based on experimental investigation. The second is based on the three fundamental assumptions of potential flow theory. The last is based on the numerical solution of the fundamental governing equations of a viscous fluid. In the following sections three different wave load models, one for each approach, are introduced.

2.3.1 The Morison equation

The semi-empirical Morison equation, introduced in Section 2.1.3, combined with first order wave theory is widely used in the prediction of hydrodynamic loads on slender structures due to its simplicity and low computational cost.

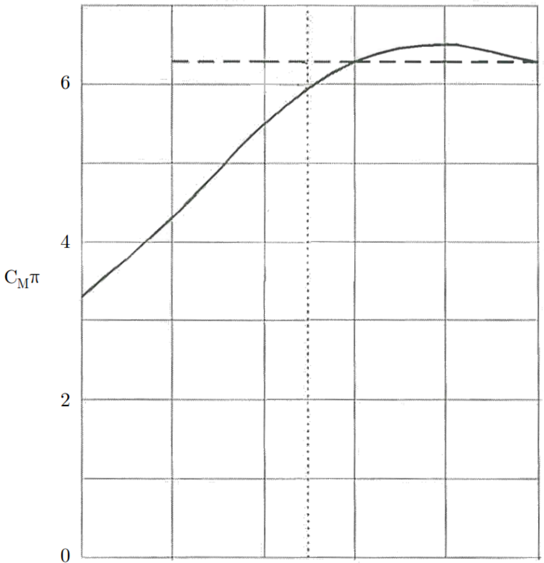

Figure 2.5: Comparison of the analytic obtained C_M and $C_M = 2$. (———), C_M as predicted by linear diffraction theory (C. MacCamy and A. Fuchs (1954)); (- - - - -), $C_M = 2$ (Pettersen (2004)).

To determine the total horizontal force acting on the cylinder, equation 2.2 must be integrated over the immersed part of the cylinder. The waves are assumed to be long compared to the cylinder diameter. The structure will not deform the wave profile, and the wave kinematics is thus undisturbed by the pile. Moreover, the two coefficients C_D and C_M are usually taken to be constant, which is in general not true. Applying linear wave theory and evaluating the wave kinematics from an undisturbed wave at the center axis of the pile, the integration can be carried out up to the mean free surface to give an approximation of the total force.

Neglecting the drag term in equation 2.2, it can be shown analytically that the Morison equation with $C_M = 2.0$ is correct as the wave length-cylinder diameter ratio tends to infinity, $L/D \to \infty$ (Faltinsen (1990)). The difference between the analytic solution of the linear diffraction problem, as presented by C. MacCamy and A. Fuchs (1954), and the inertia term in the Morison equation with $C_M = 2$ is less then 4% for $L/D > 5$ (Pettersen (2004)), as illustrated in Figure 2.5. Thus, in practice one use $L/D = 5$ as the lower limit for the application of the Morison equation. The wave forces on a monopile can then be expressed as equation 2.37, neglecting viscous forces.

$$F_x = 2\rho\pi a^2 \int_{-h}^{0} \frac{\partial u}{\partial t}, \qquad \frac{L}{D} > 5 \tag{2.37}$$

2.3.2 Generalized FNV theory

To better describe the ringing phenomenon, Faltinsen, Newmann and Vinje developed an extended diffraction theory able to capture loads up to third order. The FNV method uses a perturbation approach based on the assumption that the wave amplitude ζ_a and the cylinder radius a is small relative to the wave length L, similar to that of traditional diffraction theories. However, instead of assuming the wave amplitude to be small relative to the column radius, they allowed the two to be of the same order of magnitude. Thus making the theory applicable in severe seas. Formally, we may formulate the main assumption of the FNV model as follows; $k\zeta_a = \mathcal{O}(\epsilon)$, $ka = \mathcal{O}(\epsilon)$, $\zeta_a = \mathcal{O}(a)$ and $a/h = \mathcal{O}(\epsilon)$, where $\epsilon \ll 1$. The original FNV theory presented by Faltinsen et al. (1995) considered deep water regular incident waves only. Kristiansen and Faltinsen (2017) generalized the FNV theory to finite water depth by using wave kinematics for finite water depth.

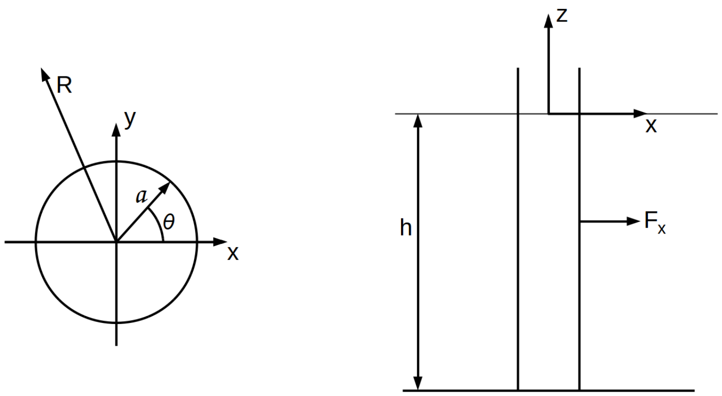

Figure 2.6: Description of the Cartesian coordinate system, load conversions, cylinder radius a, angle θ and water depth h. $R = (x^2 + y^2)^{1/2}$ is the distance from the cylinder axis to a point in the fluid.

Derivation

A Cartesian coordinate system according to Figure 2.6 is defined. The total velocity potential is written as $\phi = \phi_I + \phi_S + \Psi$, where ϕ_I, ϕ_S and Ψ are the incident wave potential, first order scattering potential and higher order scattering potential, respectively. Further, a linear diffraction potential ϕ_D is defined as $\phi_D = \phi_I + \phi_S$.

When solving the linear diffraction problem two complementary domains are considered including the outer domain, where $R = \mathcal{O}(L)$, and the inner domain where $R = \mathcal{O}(a)$. In the inner domain a are of order 1, whereas h are of order $1/\epsilon$. As $\epsilon \to 0$, the transverse length scale a remains fixed while the length of the cylinder tends to infinity. The fluid velocity field appears almost constant along the cylinder axis with $\partial/\partial z = \mathcal{O}(\epsilon)$. Consequently, the vertical derivative is much smaller than the horizontal derivatives.

$$\frac{\partial \phi}{\partial z} \ll \frac{\partial \phi}{\partial x}, \frac{\partial \phi}{\partial y} \tag{2.38}$$

Similar results apply to the second derivatives. Thus the Laplace equation reduces to the two-dimensional form, and ϕ can be replaced by a two-dimensional potential, $\phi = \phi(x, y)$.

$$\frac{\partial^2 \phi}{\partial x^2} + \frac{\partial^2 \phi}{\partial y^2} = 0 \tag{2.39}$$

By Taylor expansion of the diffraction potential ϕ_D around the cylinder axis

$x = 0$ and $y = 0$ one obtain the following solution in the near field of the cylinder in equation 2.40.

$$\begin{aligned}\phi_{Inner} = \phi_I\Big|_{x=0,y=0} + (x + \phi_{11})\frac{\partial \phi_I}{\partial x}\Big|_{x=0,y=0} + \\ (\frac{1}{2}x^2 + \phi_{21})\frac{\partial^2 \phi_I}{\partial x^2}\Big|_{x=0,y=0} + f(z,t) + \mathcal{O}(\epsilon^4)\end{aligned} \tag{2.40}$$

The terms ϕ_{11} and ϕ_{21} need only satisfy the two-dimensional Laplace equation and are determined by satisfying the impermeability condition on the cylinder surface.

$$\frac{\partial}{\partial n}(x + \phi_{11}) = 0 \qquad \text{and} \qquad \frac{\partial}{\partial n}(\frac{1}{2}x^2 + \phi_{21}) = 0, \qquad R = a \tag{2.41}$$

Here, $\vec{n}$ is the two-dimensional normal vector of the body, pointing into the fluid. A solution of equation 2.39 satisfying the body boundary conditions (eq. 2.41) can be obtained through the method of separation of variables. Since a far field condition cannot be applied to the inner solution, the potential ϕ_{Inner} contains an arbitrary function f. The function is found by matching of the inner and outer solution in an overlapping region. Thus the missing boundary condition is replaced by the matching requirement.

$$\phi_{Inner} = \phi_{Outer}, \qquad a \ll R \ll L \tag{2.42}$$

The outer solution ϕ_{Outer} is governed by the three-dimensional Laplace equation and by a suitable far field condition, but need not satisfy the body boundary condition. The appropriate solution of ϕ_{Outer} is a source distribution, along the z-axis (Newman (1977)). Applying the matching requirement (eq. 2.42) one obtain the function f. It can be shown, see Faltinsen (1999), that the three-dimensional hydrodynamic interaction potential f does not cause any horizontal force to $\mathcal{O}(\epsilon^5)$ and is therefore negligible. Thus ϕ_D is expressed as equation 2.43.

$$\phi_D = \phi_I\Big|_{x=0,y=0} + (x + \phi_{11})\frac{\partial \phi_I}{\partial x}\Big|_{x=0,y=0} + (\frac{1}{2}x^2 + \phi_{21})\frac{\partial^2 \phi_I}{\partial x^2}\Big|_{x=0,y=0} \tag{2.43}$$

The nonlinear scattering potential Ψ is a consequence of the linear scattering potential ϕ_S not satisfying the free surface boundary conditions to correct order. The solution of Ψ must satisfy the free surface condition, the three-dimensional Laplace equation, and the body boundary condition. The combined free surface boundary condition for the nonlinear scattering potential is according to equation 2.44.

$$\frac{\partial^2\Psi}{\partial t^2} + g\frac{\partial\Psi}{\partial z} = -2\nabla\phi\cdot\nabla\frac{\partial\phi}{\partial t} - \frac{1}{2}\nabla\phi\cdot\nabla\Big(\nabla\phi\cdot\nabla\phi\Big), \qquad z = \zeta_I \tag{2.44}$$

Since Ψ varies rapidly in the vertical direction in the surface region, the vertical gradient of the potential is dominant. Thus the time derivative on the left-hand side of equation 2.44 is negligible. However, this boundary condition cannot be transferred to the mean water level, $z = 0$, and must instead be imposed on the free surface. Since ka is assumed small and the domain where equation 2.44 must be considered is confined to the inner region, the free surface condition for Ψ need only be satisfied on a horizontal plane following ζ_I at $x = y = 0$. Solving the boundary value problem we obtain the following expression for the horizontal force due to Ψ (Faltinsen et al. (1995)),

$$F^{\Psi} = \rho\pi a^2\frac{4}{g}u^2\frac{\partial u}{\partial t} \tag{2.45}$$

where the particle velocity and acceleration are evaluated at $x = 0$ and $z = 0$. The distributed force due to the linear diffraction potential ϕ_D is found by integrating the pressure p along the cylinder wall in equation 2.46.

$$dF' = -\int_0^{2\pi} pn_x a d\theta \tag{2.46}$$

Here n_x is the x-component of the surface normal vector. The Bernoulli equation is used to evaluate the pressure. Carrying out the integration yields,

$$dF' = \rho\pi a^2\Big(\frac{\partial u}{\partial t} + u\frac{\partial u}{\partial x} + w\frac{\partial u}{\partial z}\Big) + a_{11}\Big(\frac{\partial u}{\partial t} + w\frac{\partial u}{\partial z}\Big) \tag{2.47}$$

where a_{11} is the two-dimensional added mass in surge. The total load acting on the cylinder in x-direction is obtained by integrating the distributed load term dF' along the cylinder up to the free surface, and adding the load due to the higher order scattering potential Ψ.

$$F_x = \int_{-h}^{\zeta} dF'(z,t)dz + F^{\Psi} \tag{2.48}$$

Discrepancies in the generalized FNV model

Kristiansen and Faltinsen (2017) carried out systematic regular wave experiments on a vertical, free-surface piercing, bottom mounted, non-moving circular cylinder. One model with typical dimensions of large monopile support structures was used for all wave conditions at a model scale of 1:48. The full scale diameter of the pile was 6.9m. Tests were performed at two water depths, being $h/a = 7.83$ and $h/a = 5.51$, and the wave conditions ranged from deep to intermediate water depths. Horizontal forces and moments were measured and higher harmonic load terms up to fifth order were studied, while the main focus was on the loads oscillating with 3ω. In particular, the influence of the linear wave steepness H_1/L and the dimensionless wave number ka was considered.

The experimental results were compared to forces estimated by the generalized FNV theory, using Stokes fifth order wave theory to obtain the wave kinematics. An overall good agreement was observed, both regarding amplitude and phase for the first, second and third load harmonic, for small to medium steep waves. More precise, the first harmonic was found to be in general good agreement for all wave conditions. Some deviations between the experimental and theoretical results were

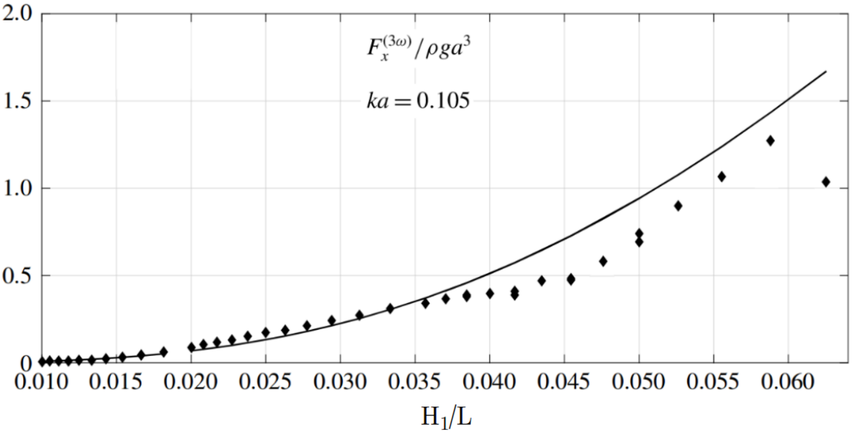

Figure 2.7: Example of amplitude of the third harmonic of the horizontal force as a function of wave steepness. (———), FNV model; ♦, experimental results obtained by Kristiansen and Faltinsen (2017)). The figure is taken from the same paper.

observed for the second harmonic, regardless of the wave steepness, as the incident waves became short, $ka > 0.12 - 0.15$. The theory overpredicts the force component, and the discrepancy increases gradually as the dimensionless wave number increases. This is expected since the FNV model does not include second order wave diffraction. Further, the third harmonic obtained with the FNV model was found to be in excellent agreement with the experimental results for the lowest wave steepnesses for all wave lengths. However, the theory overpredicts for the higher wave steepnesses. This is exemplified in Figure 2.7. Here, the amplitude of the third harmonic of the horizontal force is presented as a function of the wave steepness for $ka = 0.105$ and $h/a = 7.83$. There is a reasonably good agreement up to about $H_1/L = 1/30$. As the wave steepness further increases the theoretical and experimental results deviates and noticeable discrepancies are observed. The magnitude of these discrepancies change with the wave length, but a general increase was observed with increasing wave steepness.

2.3.3 Computational fluid dynamics

The wave load models presented so far provide reasonable estimates for the in-line forces as long as their respective assumptions are fulfilled. The low computational cost related to these models makes these tools well suited for handling large test matrices for design purposes. However, neither of the models can provide a complete description of the force variation in extreme sea states.

The rapid growth of computer hardware in recent years have enabled scientists and engineers to use the fundamental unsteady three dimensional Navier-Stokes equations to predict nonlinear wave loads on marine structures. While using Computational Fluid Dynamics (CFD) to simulate wave-structure interaction have been going on for some time, most existing studies have remained in the research stage. As an advanced numerical tool, CFD has its merits in applications where nonlinearities are of concern, as shown by Paulsen et al. (2014). Their CFD simulations predicted the additional local force peak close to, and during, the time of minimum loading, as well as the wave run-up on the downstream side of the cylinder. However, due to the high computational costs such computations impose, present-day CFD technology is still not applicable as a widespread design tool in the offshore industry.

Chapter 3

The Vortex-In-Cell Method

At present, the most widely used CFD models are generally based on a direct resolution of the Navier-Stokes equations. The usual numerical scheme being the finite volume method. However, other methods such as the finite element and the finite difference have gained much interest since they enable higher order approximations of the Naiver-Stokes equations. Although reliable, these Eulerian methods are computationally demanding and were limited to moderate Reynolds numbers and to laminar flow for some time. Other strategies were therefore developed in the early days of CFD. Among these are the Lagrangian methods, which are related to high Reynolds number flows and therefore characterized by regions of concentrated vorticity embedded in an otherwise irrotational fluid. However, in terms of computational cost, these methods are rendered impractical for high-resolution simulations. A thorough description of the different numerical schemes within this class of solvers may be found in Lewis (1991).

The Vortex-In-Cell method presented in this chapter takes advantage of the best features of both methods mentioned and is thus classified as a mixed Eulerian-Lagrangian method. The Lagrangian treatment of the vortex elements is kept while the resulting vorticity field is transported according to the full Navier-Stokes equations solved in a fixed Eulerian mesh. The main advantages of such methods are first of all the relatively low operational cost. Moreover, the dynamics are computed on the particles, removing the Courant criterion traditionally limiting the time step in Eulerian methods. Thus the hybrid methods can tackle much greater time steps.

The method presented in this chapter is based on the Vortex-In-Cell (VIC) method first developed by Christiansen (1973) and applies the Operator Splitting Technique (OST) proposed by Chorin (1973). A radially expanding polar mesh coinciding with the cylinder surface is used, enabling the surface boundary condition to be simply and precisely satisfied. The no-slip condition is enforced by using a modified version of the well known Thom's formula, as proposed by Smith and Stansby (1988). Several higher order formulations can be found in the literature. One being the fourth order accurate formula derived by Briley (1971) using a skewed seven point stencil and quadratic Lagrangian interpolation polynomials. The circulation carried by each vortex particle is projected onto the polar mesh using a second order Cloud-In-Cell (CIC) scheme (Birdsall and Fuss (1969)). The method conserves both the total circulation and linear impulse, but not the angular impulse. Higher accuracy may be achieved by applying higher order interpolation schemes, such as the fourth order $M4$ scheme (Kudela and Kozlowski (2009)), or by changing the discrete vortices into blobs with finite core and an inner Gaussian distribution of vorticity as proposed by Leonard (1985).

The direct summation of the N_v vortices produces an operational count of N_v^2 (Smith and Stansby (1988)). A large number of vortices are required to achieve a good representation of the flow. The N_v^2 operation count will therefore significantly reduce the efficiency of the VIC method presented here. More efficient methods have been developed, such as the "box-box" scheme, which has an operational count as low as N_v (Koumoutsakos and Leonard (1995)), but is not implemented in the present version of the program. To reduce the computational cost, a simplified version of the absorption procedure presented by Smith and Stansby (1989) is implemented. Here the vortices that cross the body contour due to the diffusion transport are removed from the flow. New particles, fewer in numbers, are then introduced back into the flow carrying the same amount of circulation as the vortices removed from the flow (Scolan and Faltinsen (1994)).

The following sections closely follow the excellent outline provided in the Lecture notes by Yves-Marie Scolan, see Scolan (1991).

3.1 The numerical model

The flow of an incompressible fluid with constant kinematic viscosity and density past a circular cylinder is governed by the Navier-Stokes equations and the continuity equation. In their primitive form they are formulated in terms of velocity $\vec{u}$ and pressure P.

$$\nabla \cdot \vec{u} = 0 \tag{3.1}$$

$$\frac{\partial \vec{u}}{\partial t} + (\vec{u} \cdot \nabla)\vec{u} = -\frac{1}{\rho}\nabla P + \nu \nabla^2 \vec{u} \tag{3.2}$$

If we only consider two dimensional flows, the Navier-Stokes equations may be written in the form of the Poisson equation for the stream function ψ

$$\nabla^2 \psi = -\xi \tag{3.3}$$

and the transport equation for the vorticity component normal to the flow plane

$$\frac{\partial \xi}{\partial t} + \vec{u} \cdot \nabla \xi = \nu \nabla^2 \xi \tag{3.4}$$

where the vorticity ξ is given by

$$\vec{\xi} = \xi \vec{k} = \nabla \times \vec{u} \tag{3.5}$$

At the body both the impermeability and no-slip conditions must be respected. The latter of the two may be expressed as

$$\frac{\partial \psi}{\partial x} = 0, \qquad \frac{\partial \psi}{\partial y} = 0 \qquad \text{At the body} \tag{3.6}$$

This implies that the body surface is a stream line

$$\psi_{Body} = C \tag{3.7}$$

where C is an arbitrary constant generally set to zero. This formulation of the cylinder prohibit any flux of fluid through the body surface and the impermeability condition is therefore naturally introduced in the solution of the Poisson equation (eq. 3.3).

At sufficiently large Reynolds numbers, the effect of viscosity becomes negligible far from the cylinder. The vorticity also tends to zero far from the cylinder, leaving the flow nearly inviscid and irrotational (White (2006)). Therefore, far from the body, the boundary conditions are

$$\frac{\partial \psi}{\partial x} = 0, \qquad \frac{\partial \psi}{\partial y} = U, \qquad \xi = 0 \qquad \text{At infinity} \tag{3.8}$$

3.2 The method

The distribution of the vorticity is approximated by a set of N_v discrete point vortices of strength Γ_i, located at points (x_i, y_i) such that

$$\xi(x, y) = \sum_{i=1}^{N_v} \Gamma_i \delta(x - x_i)\delta(y - y_i) \tag{3.9}$$

where $\delta(.)$ denotes the Dirac delta function. The distribution is advanced in time by the method summarized below.

- The Poisson equation for the stream function is solved on the Eulerian grid. The solution is used to create a set of new vortex particles along the cylinder, which satisfy the no-slip condition.
- The flow velocity of each vortex particle is calculated by the Vortex-In-Cell method and their position is updated by a first order scheme.
- New velocities are calculated again to give a second order correction for the vortex position.
- Viscous diffusion is simulated by superimposing a random walk to the position of the vortex particles. Vortices crossing the body surface are coalesced at the nearest surface node and diffused into the flow.

A flow chart illustrating this process is presented in Figure 3.1.

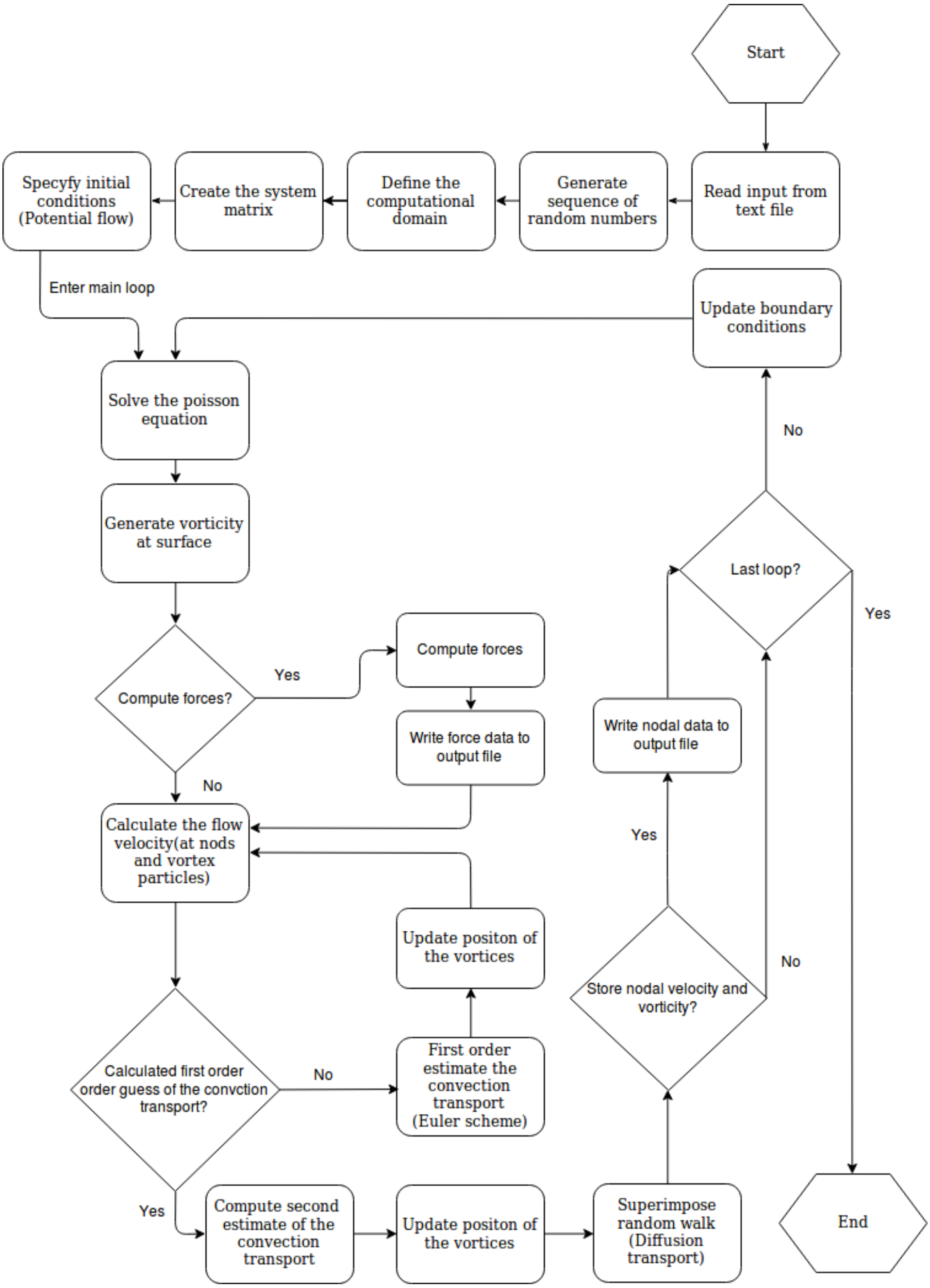

Figure 3.1: Flow chart illustrating the present implementation of the Vortex-In-Cell method.

3.2.1 Algorithm

The computational domain is defined over an annular region where the inner boundary coincide with the cylinder surface of radius $r = 1$, and the outer boundary located at a distance r_o. Uniform spacing is used in the circumferential direction, while a stretched mesh according to equation 3.10 is used in the radial direction.

$$r = B_m\left(e^{A_m r^{'}} - 1\right) + 1 \tag{3.10}$$

The coefficients A_m and B_m in equation 3.10 are found by the value of the outer radius r_o and the radial mesh spacing at the cylinder surface. The thickness of the first layer is chosen to be $\sqrt{2\nu\Delta t}$ as proposed by Smith and Stansby (1988). We will later see that this yields an adequate resolution of the boundary layer. The outer radius r_o must be sufficiently large such that the boundary conditions given by equation 3.8 hold.

In the modified polar coordinate system $(r^{'}, \theta)$, the Poisson equation may be written as

$$\frac{\partial^2\psi}{\partial\theta^2} + a(r^{'})\frac{\partial^2\psi}{\partial r^{'2}} + b(r^{'})\frac{\partial\psi}{\partial r^{'}} = -r^2\xi \tag{3.11}$$

where

$$a(r^{'}) = \left(r\frac{dr^{'}}{dr}\right)^2 \tag{3.12a}$$

$$b(r^{'}) = r\frac{dr^{'}}{dr} + r^2\frac{d^2r^{'}}{dr^2} \tag{3.12b}$$

Equation 3.11 is solved using a Fast Fourier transform technique combined with a finite difference method. Both ψ and $-r^2\xi$ are expanded as Fourier series in the azimuthal θ-direction and substituted into the finite difference analogue of equation 3.11. This yields a set of tridiagonal linear systems, one for each harmonic amplitude of ψ. A thorough description of the solution of the Poisson equation is found in Appendix A.

The CIC method, also known as the Area-Weighting scheme, proposed by Christiansen (1973) is used to project the circulation carried by each vortex onto the nodes of the polar mesh. If Γ_{Vortex} is the strength of a single vortex, the circulation assigned to the four corner nodes of the cell of which the vortex is confined is computed as follows

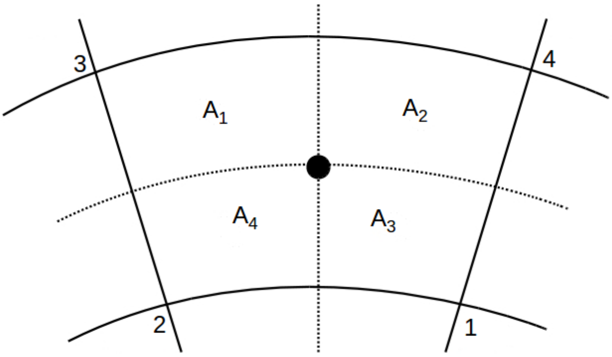

Figure 3.2: Illustration of the Cloud-In-Cell scheme

$$\Gamma_{node_i} = \frac{A_i \Gamma_{Vortex}}{A_{Cell}} \qquad \text{For i} = 1,2,3,4 \tag{3.13}$$

where the areas A_k is defined in Figure 3.2 and A_{Cell} is the total area of the cell in which the vortex is confined. For large number of particles the nodal circulation at node (j,k) is obtained by summing up the contribution from all the individual vortices.

Having done that, the nodal circulation $\Gamma(j,k)$ is transformed in terms of vorticity by the following formula

$$\xi(j,k) = \frac{\Gamma(j,k)}{r_{j,k}\Delta\theta} \frac{dr^{'}}{dr}\Big|_{r'=j} \tag{3.14}$$

To model the action of viscosity, new vortices are created along the cylinder surface at each time increment such that the no-slip condition is satisfied. The additional circulation Γ_{New} introduced at the surface nodes $(0,k)$ is given by (Smith and Stansby (1988))

$$\Gamma_{New} = \Delta\theta\xi(0,k)\frac{dr}{dr'}\Big|_{r'=0} - \Gamma_{Old} \tag{3.15}$$

where Γ_{Old} is the circulation distributed onto the surface mesh from the existing vortices. Since the cylinder surface is assumed to be a streamline, ψ is only a function of r along the body and the finite difference analogue of equation 3.11 reduces to

$$\xi(0,k) = -a(0)\Big(\psi(1,k)-2\psi(0,k)+\psi(-1,k)\Big)-\frac{1}{2}b(0)\Big(\psi(1,k)-\psi(-1,k)\Big) \quad (3.16)$$

In order to satisfy the body boundary condition the stream function must be constant at all points inside the cylinder. Both $\psi_{0,k}$ and $\psi_{-1,k}$ is therefore set to zero and equation 3.16 then becomes

$$\xi(0,k) = -\Big(a(0)+\frac{1}{2}b(0)\Big)\psi(1,k) \quad (3.17)$$

The additional circulation Γ_{New} generated at node $(0,k)$ is shared equally among n_{sv} newly created vortices at each node. These sub-vortices are then spread uniformly over the corresponding surface segment surrounding the point of vorticity production.

To solve the vorticity transport equation (3.4) the Operator Splitting Technique proposed by Chorin (1973) is employ. Here equation 3.4 is split into a linear diffusion equation

$$\frac{\partial\xi}{\partial t} = \nu\nabla^2\xi \quad (3.18)$$

and the nonlinear Euler equation

$$\frac{\partial\xi}{\partial t} = -\vec{u}\cdot\nabla\xi \quad (3.19)$$

Equation 3.19 is solved by convecting the vortices. The vortices are moved with their local velocity without changing their circulation. These velocities are found through bilinear interpolation using the nodal values of the stream function of the cell containing the vortex. More details are found in Appendix B. The convection motion is calculated by a second order Runge-Kutta scheme in the following manner. First, the new position of the vortices at the instant $t+\Delta t$ is computed using the first order Euler scheme

$$\vec{x}_2^1 = \vec{x}_1 + \vec{u}\Delta t = \vec{x}_1 + d_1 \quad (3.20)$$

where $\vec{u}$ is the flow velocity at a vortex, $\vec{x}_1$ is its position before the displacement and $\vec{x}_2^1$ is the position after the displacement according to the first order scheme. The vortices are moved to their new positions and new computations give a prediction of the velocity at the position $\vec{x}_2^1$. Then a second guess of the displacement is made as follows

$$d_2 = \vec{u}(\vec{x}_2^1, t + \Delta t)\Delta t \tag{3.21}$$

The final position is calculated by averaging the two displacements.

$$\vec{x}_2 = \vec{x}_1 + \frac{1}{2}(d_1 + d_2) \tag{3.22}$$

The linear diffusion equation (3.18) is solved by adding a random walk to the motion of the discrete vortex particles. The random numbers are distributed according to a Gaussian distribution with zero mean value and a standard deviation of $\sqrt{2\nu\Delta t}$. If g_1 and g_2 are two numbers selected form the normal distribution mentioned above and (x_1, y_1) is the position of a point vortex before the displacement, then the position of the vortex after the diffusion process, (x_2, y_2), is given by equation 3.23.

$$\begin{aligned} x_2 &= x_1 + g_1 \\ y_2 &= y_1 + g_2 \end{aligned} \tag{3.23}$$

In practice, a large sequence of random numbers (400000) is generated once and for all at the beginning of the simulation. This is achieved by using a Box-Muller scheme (Press et al. (1992)).

During the convection process, some vortices may enter the body. These vortices are reflected to their mirror-images position (Smith and Stansby (1988)). Further, vortices may also cross the cylinder surface due to the random walk, this is especially true in the case of oscillating current at low values of KC. These vortices, which enter the body, are coalesced at the nearest surface node. New vortices are then re-injected into the fluid flow at a certain radial distance chosen from the same Gaussian distribution as for the diffusion process. This technique proposed by Scolan and Faltinsen (1994) drastically reduce the number of vortices present in the flow and the CPU time is consequently reduced.

It should be noted that there exist no strong theoretical proof for the convergence of the combined VIC-OST method when a solid boundary is present. In cases where there exist no boundaries, it has been shown that the convergence of the Operator Splitting Technique depends mainly on the Reynolds number, time step and number of vortex particles (Scolan and Faltinsen (1994)). Furthermore, since the diffusion process is modeled by imposing a random walk to the motion of the vortices, all local variables such as pressure, vorticity, velocity and so on, have a small random component proportional to $\sqrt{\Delta t/Re}$.

3.3 Calculation of forces

For viscous and incompressible flows, the forces originate from the pressure which acts normal to the body surface and a purely viscous stress which acts tangentially.

$$F_x = -\int_B (p\vec{n}_x + \rho\nu\xi\vec{\tau}_x)dl = F_{p,x} + F_{s,x} \tag{3.24}$$

Here, $\vec{n}_x$ and $\vec{\tau}_x$ is the x components of the normal and tangent vector of cylinder surface respectively. Since the pressure is not determined in the present method, an alternative way of calculating the surface pressure must be used to obtain the pressure force. There exist several ways to derive such an expression. The following is the outline of the most commonly used method, which is the method implemented in the present VIC program.

Due to the no-slip condition both the velocity and acceleration are equal to zero at the cylinder surface. Equation 3.2 therefore simplifies to equation 3.25 along the body contour.

$$\frac{1}{\rho}\nabla P = \nu\nabla^2\vec{u} \tag{3.25}$$

By substituting equation 3.1 and 3.5 into the above equation and forming a scalar product with the azimuthal unit vector $\vec{\theta}$, we get

$$\frac{\partial P}{\partial\theta} = \rho\nu\frac{\partial\xi}{\partial n} \tag{3.26}$$

Assuming that the pressure is piecewise constant along the body, the discretization of equation 3.26 gives

$$P_{k+\frac{1}{2}} - P_{k-\frac{1}{2}} = \rho\nu\Delta\theta\frac{\partial\xi}{\partial n} \tag{3.27}$$

where the point $k+1/2$ is the midpoint of the segment $[\theta_k, \theta_{k+1}]$. The pressure force is thus found by summation of the pressure distribution obtained from equation

3.27

$$\frac{1}{\rho}F_{p,x} = -\nu r(\Delta\theta)^2 \sum_{k=1}^{N_\theta} \left[\cos\theta_k \sum_{i=1}^{k} \frac{\partial\xi}{\partial n}\Big|_i \right] \tag{3.28}$$

where the normal gradient of the vorticity at the cylinder surface, $\partial\xi/\partial n$, may be obtained by integrating the Navier-Stokes equation along a small closed loop surrounding a point of vorticity production, namely a node at the cylinder surface (Scolan (1991)). Performing this analysis yields the following expression

$$\frac{\partial\xi}{\partial n}\Big|_k = -\nu\frac{\Gamma_{New,k}}{\Delta\theta\Delta t} \tag{3.29}$$

where $\Gamma_{New,k}$ is the newly created circulation at the k^{th} surface node. The validity of equation 3.29 is somewhat questionable and may lead to inaccurate force calculations, as shown by Lin et al. (1996). Their results showed that the method presented above significantly overpredicted the in-line force on a circular cylinder in planar oscillatory flow when compared to Wang's theory. They, therefore, recommended using other methods based on the radial integration of pressure through the Navier-Stokes equations or the generalized Blasius theorem. However, their investigation of the present method was limited to small values of β (=76) and $K\mathrm{C} \leq 2$, whereas the current study only considers large values of β and $K\mathrm{C} \geq 1-2$. Further, the method has been implemented by several authors yielding adequate estimations of the in-line forces (Smith and Stansby (1988), Scolan and Faltinsen (1994), Smith and Stansby (1991), Skomedal et al. (1989)).

In order to obtain the friction force $F_{s,x}$, we have to provide the vorticity on the cylinder. Since the area-weighting scheme smoothens the vorticity distribution along the cylinder surface, the surface vorticity cannot be taken as the nodal value of ξ along the body. Thus, the vorticity is found by using a Taylor development of ξ along the normal direction on the body surface. We are then led to the development

$$\xi_{0,k} = \xi_{1,k} - (n_1 - n_0)\frac{\partial\xi}{\partial n}\Big|_k \tag{3.30}$$

where the indices 0 and 1 denote the position on the body contour and at a small normal distance from the body, respectively. Introducing equation 3.30 into the expression for the skin friction we obtain the following formula for $F_{s,x}$ in equation 3.31.

$$\frac{1}{\rho}F_{s,x} = \nu\Delta\theta \sum_{k=1}^{N_\theta} \left[\xi_{1,k} - (n_1 - n_0)\frac{\partial\xi}{\partial n}\Big|_k \right] \tag{3.31}$$

3.4 Numerical implementation

A computer program in the program language Fortran 08 was developed incorporating the method outlined in the previous sections. The solution of the tridiagonal matrix system was solved using the DGTTRS routine from LAPACK (Anderson et al. (1991)), and the Fourier transform for were done using a double precision version of the Fortran package FFTPack (Swarztrauber (1982)).

3.5 Impulsively started flow

The accuracy of the VIC-program was first tested by carrying out computations of an impulsively started flow past a circular cylinder. A summary of the grid parameters, time step and $R\mathrm{e}$ tested are presented in Table 3.1.

A characteristic feature of an impulsively started flow past a circular cylinder is the appearance of two, recirculating bubbles, often referred to as the main eddy (Bouard and Coutanceau (1980)). As the Reynolds number increases the velocities in these circulating regions get larger, and then, for $R\mathrm{e} > 60$ a secondary phenomena occurs during the development of the flow. At first, the streamlines close to the cylinder and about half-way between the rear stagnation point and separation points show some distortion, as seen in Figure 3.3.

For higher values of $R\mathrm{e}$ ($R\mathrm{e} > 500$) these small disturbances grow and form small secondary eddies, which has a rotation opposite to that of the main eddy. As $R\mathrm{e}$ further increases these small eddies increase in size, as seen in Figure 3.4 and 3.5, until the outer boundary touches the boundary of the main circulating bubble, thus splitting the main eddy in two.

Table 3.1: Grid parameters and time step used in the simulation of impulsively started flow past a circular cylinder.

$R\mathrm{e}$	N_r	N_θ	$\Delta\tilde{t}$	r_o
300	300	512	0.01	5D
550	300	512	0.01	5D
3000	400	1024	0.005	5D
9500	500	2048	0.0025	5D

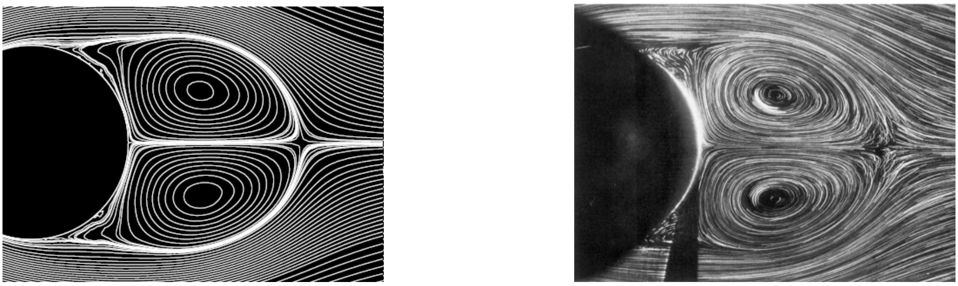

(a) **(b)**

Figure 3.3: Comparison of the streamlines from the VIC program (a) with the experimental flow visualization of Bouard and Coutanceau (1980) (b) at $\tilde{t} = 2.5$, $Re = 300$.

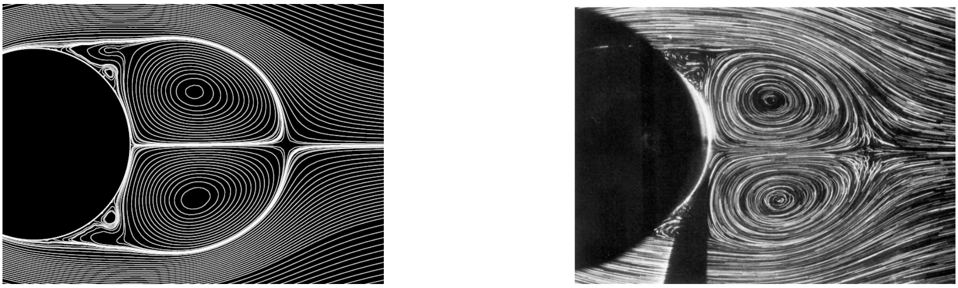

(a) **(b)**

Figure 3.4: Comparison of the streamlines from the VIC program (a) with the experimental flow visualization of Bouard and Coutanceau (1980) (b) at $\tilde{t} = 2.5$, $Re = 550$.

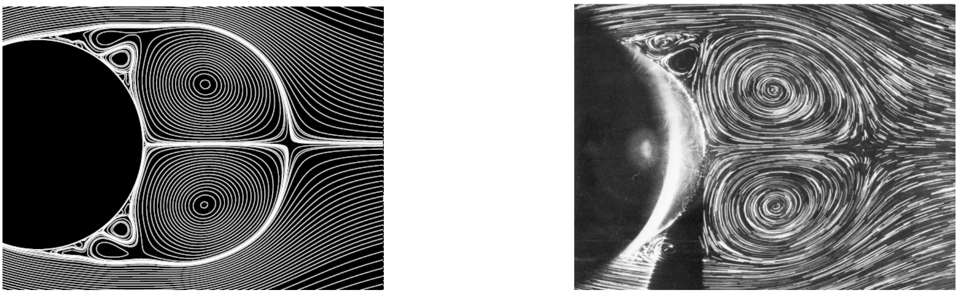

(a) **(b)**

Figure 3.5: Comparison of the streamlines from the VIC program (a) with the experimental flow visualization of Bouard and Coutanceau (1980) (b) at $\tilde{t} = 2.5$, $Re = 3000$.

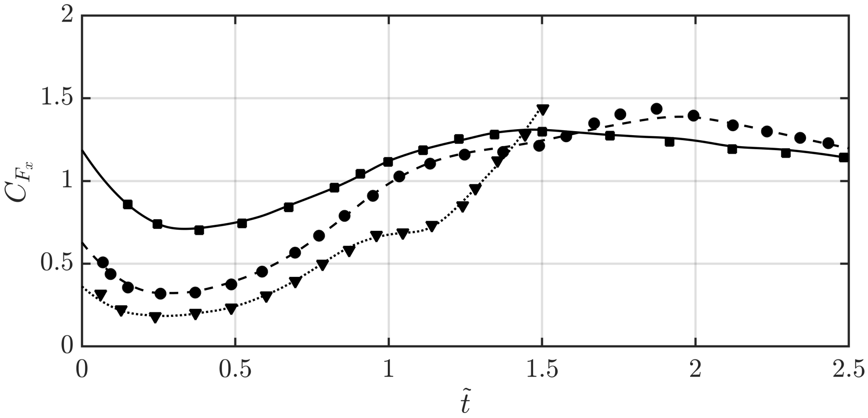

Figure 3.6: Time development of the dimensionless in-line force C_{F_x}. Lines represent results obtained with the present VIC method, while the points correspond to the results obtained by Koumoutsakos and Leonard (1995). (———), ■, $Re = 550$; (- - - - -), ●, $Re = 3000$; (··········), ▼, $Re = 9500$.

Figure 3.3 to 3.5 show comparisons between the numerical streamline distribution obtained with the present method with experiments (Bouard and Coutanceau (1980)) at $Re = 300$, 550 and 3000 and $\tilde{t} = 2.5$, where the dimensionless time, $\tilde{t}$, is defined as $\tilde{t} = Ut/D$. The figures show good qualitative agreement between the numerical method and experimental visualization. The present VIC program seems to predict the developments of the primary eddy, as well as the occurrence of the small secondary eddies rather well. Both regarding size and position. However, the numerical streamline distribution is not completely symmetric, whereas the experimental data are symmetric. This is most noticeable at $Re = 550$, where the secondary eddy on the upper side of the cylinder is smaller than that of the lower side. These small deviations are believed to be due to the random walk imposed on the vortex particles. As the Reynolds number increase, the flow becomes less viscous, and the effect of the diffusion process becomes less pronounced. Thus the flow field predicted by the present method becomes more symmetric as Re increases, as shown in Figure 3.5a. For the two highest Reynolds numbers tested in this section, a very dense mesh is required to correctly reproduce the complex flow features in the vicinity of the cylinder, see Table 3.1. At the end of these simulations a large number of computational elements, $N_v \approx 500000$, was present. Visualization of the flow at $Re = 5000$ and $Re = 95000$ can be found in Appendix E.

The results presented above give an indication of the accuracy of the present method. However, as pointed out by Koumoutsakos and Leonard (1995), streamline diagnostics are forgiving and may fail to detect deviations from the correct solution, as they are a smooth function of the flow. The computed in-line force are two derivatives less smooth then the streamlines and may therefore give a more precise measure of the accuracy of the present method. In Figure 3.6 a comparison of the calculated in-line force coefficient with the results of the high-resolution simulations carried out by Koumoutsakos and Leonard (1995) is presented. The general agreement is good. However, some discrepancies are observed. This may be related to how the body forces are computed. The present method uses the simple strategy outlined in Section 3.3, whereas Koumoutsakos and Leonard (1995) obtained the force by integrating the change of the linear impulse within the computational domain.

Table 3.2: Force coefficients calculated cycle by cycle.

KC	2.0		6.0		10.0	
Cycle	C_M	C_D	C_M	C_D	C_M	C_D
1	1.9637	0.6811	1.7263	1.1050	1.5006	1.4944
2	1.9603	0.7090	1.7293	1.2324	1.5112	1.7580
3	1.9523	0.6657	1.5783	1.6888	1.7376	1.4744
4	1.9427	0.7398	1.4926	0.7834	1.7116	1.7618
5	1.9360	0.7356	1.7793	1.1774	1.1543	1.5681
6	1.9215	0.7709	1.6833	1.4362	1.3384	2.7866
7	1.9541	0.7359	1.6402	1.3432	2.4300	0.2763
8	1.9474	0.6917	1.6020	1.2969	1.2928	1.6461
9	1.9459	0.7650	1.3591	2.1084	1.7558	1.9928
10	1.9385	0.7483	1.3753	1.3002	1.6837	1.5577
11	1.9493	0.8062	1.5633	1.8513	1.3499	2.2231
12	1.9514	0.6946	1.4916	1.8078	1.6081	1.9492
13	1.9561	0.8063	1.6843	1.9571	1.0851	1.5758
14	1.9429	0.7689	2.5004	1.2546	1.3534	1.8536
15	1.9426	0.7376	2.0175	1.0214	1.5878	2.0544
16	1.9141	0.7811	1.7157	1.2020	1.0934	1.6997
17	1.9200	0.7231	1.7794	1.5108	0.8754	1.6350
18	1.9395	0.6689	1.7942	0.9649	2.0004	1.5905
19	1.9523	0.7641	1.7335	1.3773	1.5748	1.7525
20	1.9262	0.7787	1.4070	1.8859	1.6570	2.1484

3.6 Oscillatory flow

In order to further establish the accuracy of the method in predicting the in-line forces, in particular the drag and inertia coefficients, a number of numerical experiments were carried out for a cylinder in a mono-harmonic oscillatory flow. Values of the force coefficients were obtained from the Morison equation applying the standard Fourier averaging process presented in Section 2.1.4. Then values of C_M and C_D are determined by averaging the two coefficients over a number of flow cycles. The two first flow cycles were neglected when computing the mean of C_M and C_D. The computation of the root mean square was performed in a similar fashion. At small KC numbers the cyclic variation of the force coefficient is small. As the KC number increases, stronger vortex structures are shedded, and larger variations may occur. This is illustrated in Table 3.2, where results of the cycle to cycle variation of the Morison force coefficients for $K\mathrm{C} = 2$, 6 and 10, obtained by the present VIC program is presented. The values of C_M and C_D presented in this section will therefore somewhat depend on the number of flow cycles simulated. For $K\mathrm{C} \leq 4$ 6 - 8 flow cycles were usually simulated, while up to 20 cycles were used for the largest KC numbers.

A direct comparison between the computed in-line force history and the Morison equation is shown in Figure 3.7 for six different KC numbers covering the KC range of interest. For small values of KC the agreement between the two models are very close, while the results deviate at higher KC numbers. This is expected since the Morison representation of the in-line force is good in the range of KC where inertia forces dominate, but it is not able to capture the complete picture of the force variation when the flow separation occurs (Sumer and Fredsøe (2006)). However, the VIC-program seems also to struggle when the KC number become sufficiently large. Looking at the time series obtained from the numerical simulation we observe large, seemingly random, fluctuations in the force history for $K\mathrm{C} \geq 6 - 8$. The fluctuations becoming larger as KC increase. Additionally, a pronounced phase-difference is observed for the largest KC values. It is unclear to the author why this occur, but it seems plausible that the accuracy of equation 3.29 decreases as the vortex structures close to the cylinder increase in strength and size.

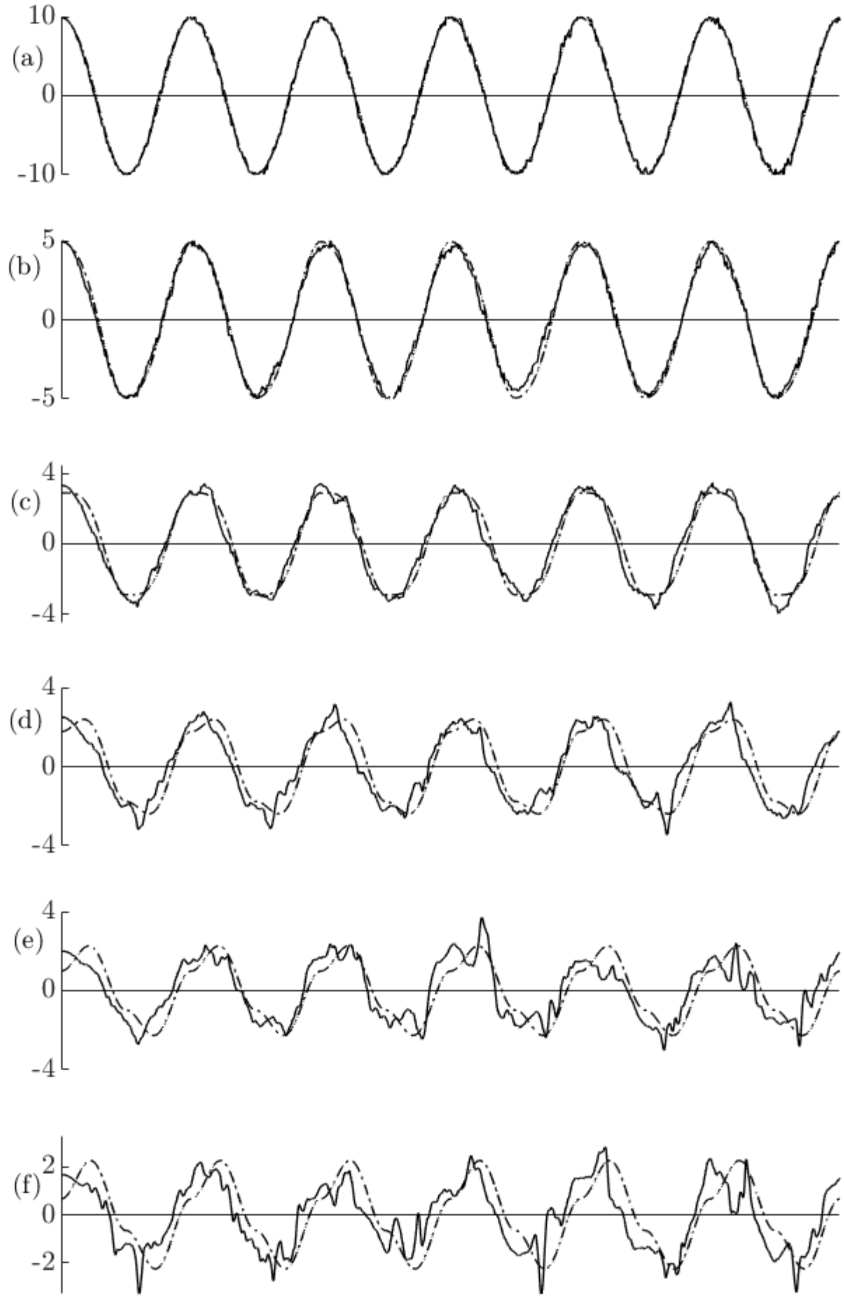

Figure 3.7: Examples of time variation of the in-line force. (———), force calculated by the VIC program; (-·-·-·-), the Morison equation with experimentally obtained C_M and C_D (Sarpkaya (1976)). (a) KC = 2. (b) KC = 4. (c) KC = 6. (d) KC = 8. (e) KC = 10. (f) KC = 12

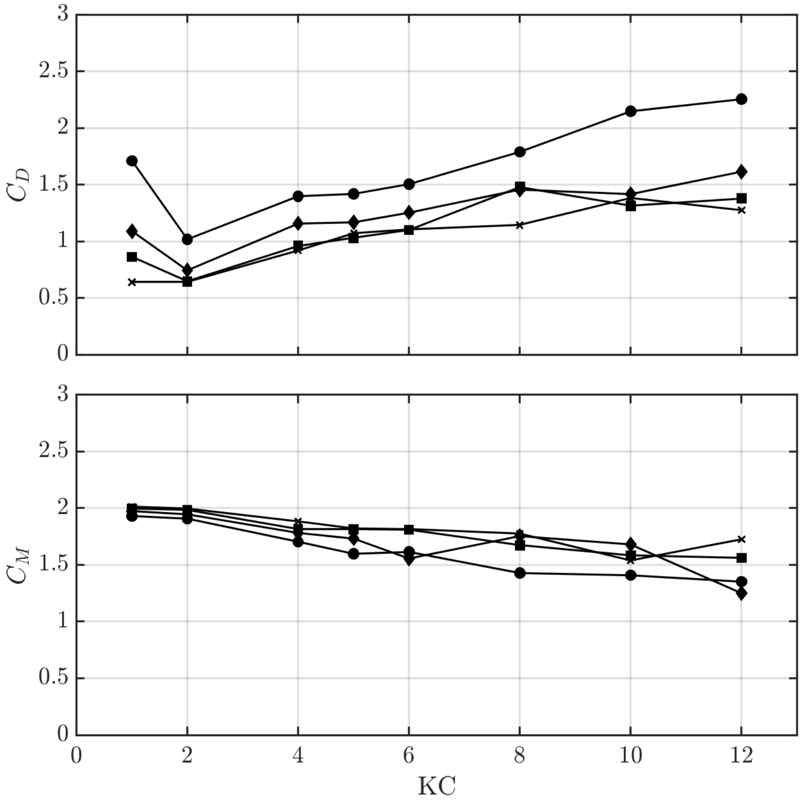

Figure 3.8: Effect of time step on C_M and C_D. (—●—), $n_t = 50$; (—◆—), $n_t = 100$; (—■—), $n_t = 200$; (—×—), $n_t = 500$. $N_r = 200$, $N_\theta = 256$ and $r_o = 50D$ were used in all simulations.

3.6.1 Sensitivity analysis

Several computations were made to determine the influence of the time step, grid spacing and domain size. KC values ranging from 1 to 12 were tested at a Reynolds number of 10000.

Effect of time step

The sensitivity analysis of the time step Δt was performed using four different time steps. The time steps tested are chosen in order to have a certain number of steps per period. That is to say $U_o\Delta t/D = K\text{C}/n_t$, where n_t is the number of steps per period. The development of C_M and C_D computed with $n_t = 50$, 100, 200 and 500 are shown in Figure 3.8.

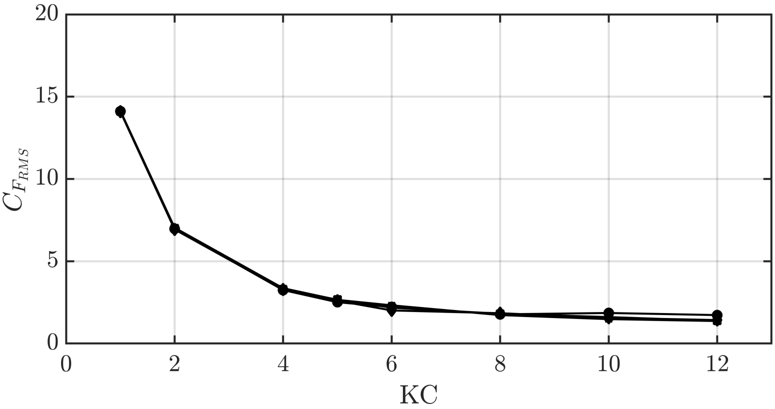

Figure 3.9: Effect of time step on the root mean square of the in-line force. (—●—), $n_t = 50$; (—◆—), $n_t = 100$; (—■—), $n_t = 200$; (—×—), $n_t = 500$. $N_r = 200$, $N_\theta = 256$ and $r_o = 50D$ were used in all simulations.

It is clear from the figure that the time step has a great influence on the computed force coefficients. As the time step decreases, we observe a drop of C_D, while C_M increases for $K\mathrm{C} < 6$. However, the difference in the predicted in-line force, as shown by the RMS values in Figure 3.9, are small in the same KC range. It therefore seems likely that the time step mainly affects the phasing of the computed in-line force and not the force amplitude.

At higher KC values no apparent trends are observed. It is believed that the large fluctuations observed in the times series, Figure 3.7, are the reason for the inconsistent prediction of the two force coefficients at $K\mathrm{C} > 6$.

Effect of grid refinement

The mesh resolution has a large influence on the computed result of all numerical simulations. Especially within the boundary layer, where a fine mesh is necessary to capture the rapid change of the vorticity and velocity field. To increase the grid density close to the body, without increasing the computational time significantly, an exponential grid distribution is employed in the radial direction. Thus concentrating the number of grid cells close to the cylinder.

To get a rough estimate of how well the boundary layer is resolved, equation 3.32 is applied. It is an estimate of the boundary layer thickness δ_B for a circular cylinder in oscillatory flow (Faltinsen (1990)).

$$\delta_B = 4.6\sqrt{\frac{2\nu}{\omega}} \tag{3.32}$$

Note that this formula is valid for non-separated flows only. However, as mentioned in Section 2.1.1, the boundary layer thickens when flow separation occurs. Thus equation 3.32 provides us with a lower limit of δ_B. Remembering that the width of the innermost cell is proportional to the diffusion transport, $\sqrt{2\nu\Delta t}$. The ratio between Δr_1, the first spacing close to the cylinder, and the boundary layer thickness may be written as equation 3.33,

$$\frac{\Delta r_1}{\delta_B} = \frac{\sqrt{2\nu\Delta t}}{4.6\sqrt{\frac{2\nu}{\omega}}} = \frac{\sqrt{\frac{2K\mathrm{C}U_oD^2}{\mathrm{Re}U_on_t}}}{4.6\sqrt{\frac{2K\mathrm{C}U_oD^2}{2\pi U_o\mathrm{Re}}}} = \frac{1}{4.6}\sqrt{\frac{2\pi}{n_t}} \tag{3.33}$$

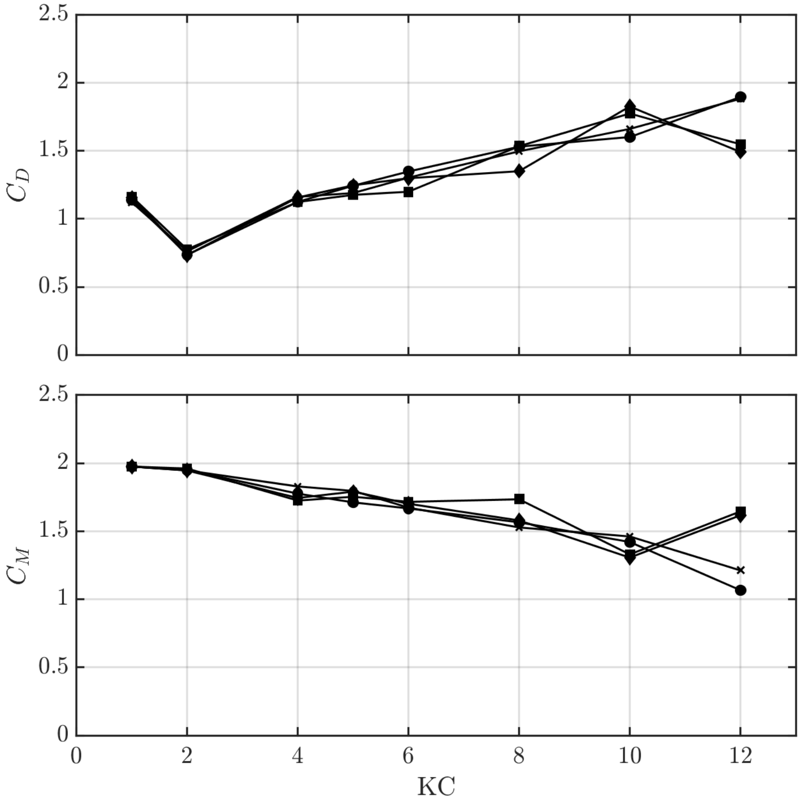

Figure 3.10: Effect of N_r on C_M and C_D. (—●—), $N_r = 100$; (—◆—), $N_r = 200$; (—■—), $N_r = 300$; (—×—); $N_r = 400$. $N_\theta = 256$, $r_o = 50D$ and $n_t = 100$ were used in all simulations.

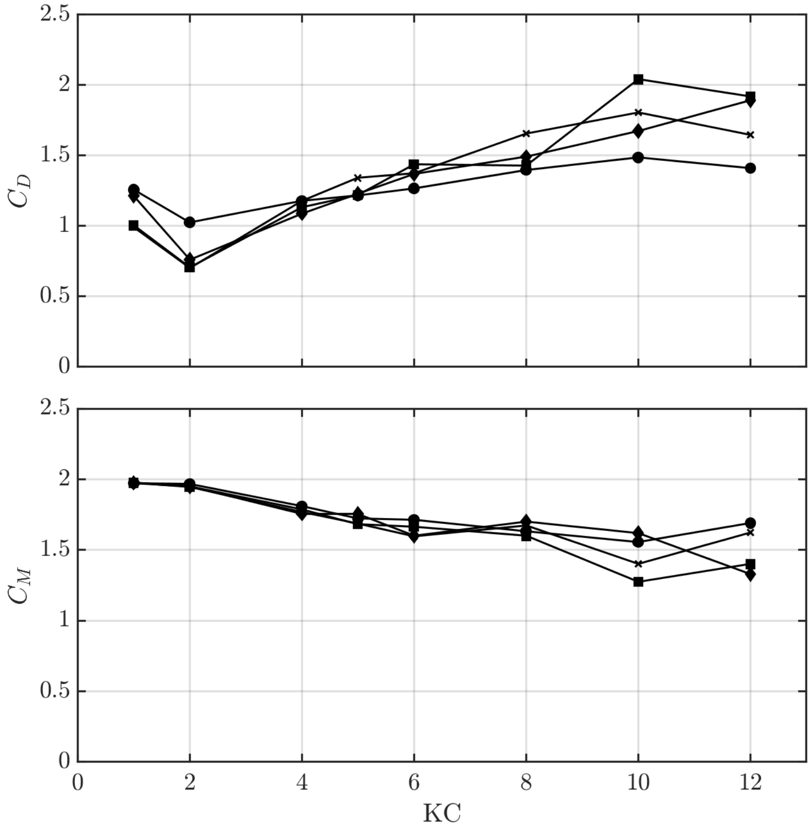

Figure 3.11: Effect of N_θ on C_M and C_D. (—●—), $N_\theta = 64$; (—◆—), $N_\theta = 128$; (—■—), $N_\theta = 256$; (—×—), $N_\theta = 512$. $N_r = 200$, $r_o = 50D$ and $n_t = 100$ were used in all simulations.

where n_t is of order 100. The first spacing near the cylinder along a radial line is then approximately 5% of the boundary layer thickness, which indicates that the boundary layer is adequately resolved. Note that the relative thickness of the first layer estimated in the above equation is unaffected by the number of grid cells in the radial direction.

To obtain accurate results, the quality of the mesh itself must also be evaluated. One important factor determining the mesh quality is the aspect ratio of the cells, defined as the ratio between the longest edge length to the shortest edge length. At the surface cells, this ratio may be expressed as in equation 3.34.

$$\frac{\Delta\theta}{\Delta r_1} = \frac{\frac{2\pi}{N_\theta}}{\sqrt{2\nu\Delta t}} = \frac{\frac{2\pi}{N_\theta}}{\sqrt{\frac{2K\mathrm{C}D^2}{Re n_t}}} \tag{3.34}$$

Using $N_\theta = 100$, $KC = 10$ and $Re = 10000$, equation 3.34 gives an aspect ratio of approximately 7. Ideally, the aspect ratio should be equal to 1. To acquire such a low aspect ratio N_θ must be of order 1000, which would result in a computational effort deemed too high in the present study.

Figure 3.10 shows the development of C_D and C_M with four different grid densities in the radial direction. It is apparent that the radial grid density is of minor importance for $KC < 6$. This is expected since N_r mainly affect the grid density far from the cylinder where grid refinement has less effect on the solution. The results are once again inconclusive for the largest KC values.

The effect of the circumferential grid spacing is presented in Figure 3.11. Increasing the azimuthal grid density seems to have some effect on the predicted C_D, while the computed C_M is less affected by N_θ.

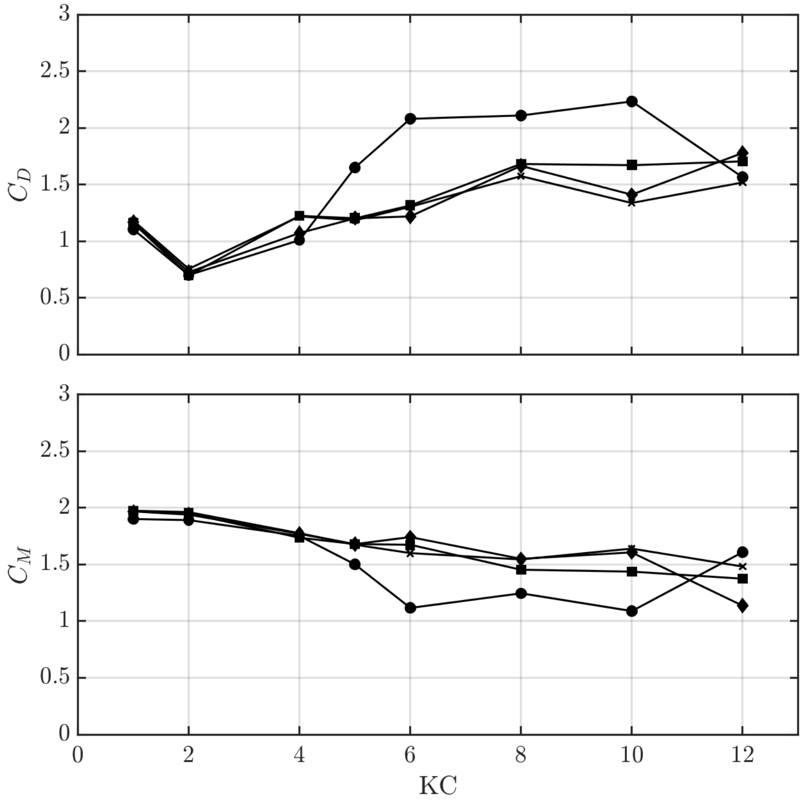

Figure 3.12: Effect of r_o on C_M and C_D. (—●—), $r_o = 2.5D$; (—◆—), $r_o = 5D$; (—■—), $r_o = 12.5D$; (—×—), $r_o = 50D$. $N_r = 200$, $N_\theta = 256$ and $n_t = 100$ were used in all simulations.

Effect of domain size

The computational domain is defined in an annular region, with only the location of the outer boundary r_o as an input parameter. To determine the effect of the domain size, four different domain sizes were examined; r_o = 2.5D, r_o = 5D, r_o = 12.5D and r_o = 50D.

Looking at Figure 3.12 one can observe a significant change in both C_M and C_D with increasing domain size. The effect is especially noticeable for the smallest domain, yielding significantly higher and lower values of C_D and C_M respectively. The results from the two largest computational domains are indistinguishable for KC < 6 and only minor differences are observed for KC ≤ 8.

Choice of simulation parameters

From the results presented till now, it is clear that the ability of the presented VIC program to predict the in-line force depends on the KC number. The numerical computation of the in-line force seems to be consistent up to KC ≈ 6. At higher KC values large, seemingly random, variations of the computed force coefficients are observed. It may indicate that a finer mesh and shorter time step is needed to obtain an accurate representation of the force history for KC > 6 than what used in the present investigation. A thorough study of the grid resolution and time step at high KC numbers is needed to resolve this problem. However, as the CPU time increases rapidly with both mesh density and time step, see Section 3.7, this has not been performed in the present work. The choice of simulation parameters will therefore be based on the results presented for KC < 6.

Figure 3.8 and 3.12 indicates that $n_t = 200$ and $r_o = 12.5D$ is sufficiently large. Further increasing these values did not affect the computed force coefficients. The grid study showed that the radial grid density did not significantly affect the

Table 3.3: Summary of grid parameters and time step for oscillatory flow past a circular cylinder.

N_r	N_θ	r_o	n_t
100	256	12.5D	200

computed in-line force. Thus to keep the computation cost as low as possible $N_r = 100$ will be used in the remaining part of this study. For the circumferential grid density $N_\theta = 256$ is chosen, to reduce the computational burden. This choice may be questionable as clear differences are observed between $N_\theta = 256$ and $N_\theta = 512$ in Figure 3.11. However, the results obtained with the two grid densities only differs with about 6% for $K\mathrm{C} < 6$ and the choice is not believed to affect the results presented in Chapter 5 significantly. The simulation parameters used in the remainder of this work are summarized in Table 3.3.

3.6.2 Comparison with experimental results

Values of C_D and C_M computed by the present method are plotted together with drag and inertia coefficients measured by Sarpkaya (1976) at $R\mathrm{e} = 10000$, 20000 and 40000 in Figure 3.13 and 3.14. For small values of $K\mathrm{C}$ ($\leq$ 5-6) the agreement between the experimentally measured and computed C_D is very close, regardless of $R\mathrm{e}$. Over the same $K\mathrm{C}$ range both the numerically predicted and experimental measured inertia coefficient show the same general trend. However, the numerical prediction of C_M is approximately $5 - 10\%$ smaller than the experimental data. This indicates that the present method somewhat underpredicts the in-line forces relative to the experimental measurements. Similar trends were also observed by Skomedal et al. (1989) and Lin et al. (1996). The reason for this is not clear. It may be related to three-dimensional flow features, which are present in the experiments but cannot be reproduced in a two-dimensional simulation. Furthermore, results presented by Sumer and Fredsøe (2006) suggest that one may expect the boundary layer of a cylinder in oscillatory flow to be turbulent for Re as low as 5000 - 7000. This fact is not accounted for in the numerical simulations but may have affected the experimental measurements presented in Figure 3.13 and 3.14.

For $K\mathrm{C}$ above 6, differences between the experiment and numerical prediction of C_D appears. This is most apparent for the lowest Reynolds number, $R\mathrm{e} = 10000$. Here the numerical prediction does not reproduce the rapid rise of the drag coefficient. Instead, the computed drag coefficient, in general, decreases as $K\mathrm{C}$ increases. Large local variation of the numerical predicted C_D is also noticed in this range of $K\mathrm{C}$. For larger Reynolds numbers the computed C_D increases almost monotonically with $K\mathrm{C}$. The agreement is good for $R\mathrm{e} = 20000$, whereas the present program overpredicts the drag coefficient at $Re = 40000$.

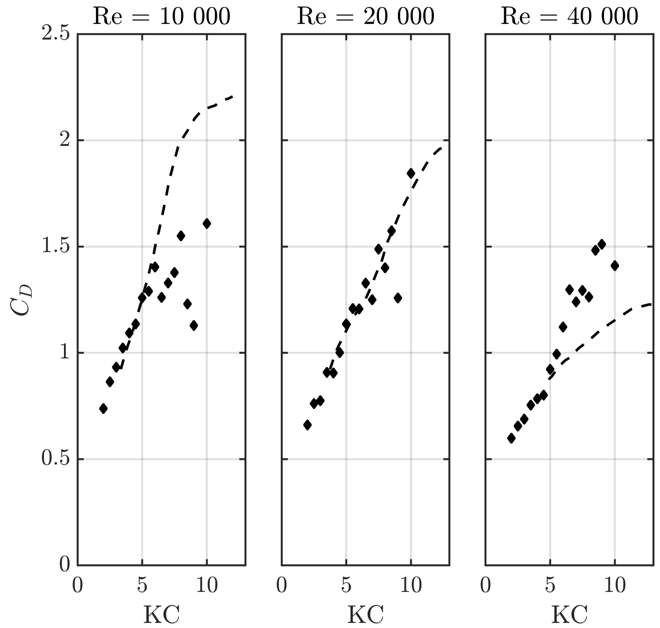

Figure 3.13: Computed and measured drag coefficients. (- - - - -), experimental measurements (Sarpkaya (1976)); ♦, VIC program.

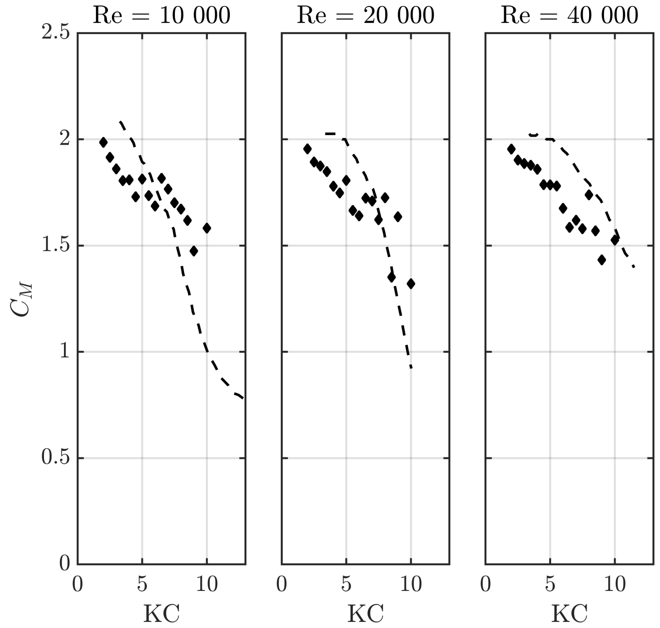

Figure 3.14: Computed and measured inertia coefficients. (- - - - -), experimental measurements (Sarpkaya (1976)); ♦, VIC program.

The numerical prediction of C_M is in general closer to the experimental measurements than those of C_D. However, significant scattering is observed in the numerical data for $K\mathrm{C} > 5$. Furthermore, the numerical predicted inertia coefficient almost ceases to decrease for $6 < KC < 8$ at $R\mathrm{e} = 10000$ and 20000, whereas the experimental data decrease significantly. The same trend is not seen at the highest value of *Re*. Here both numerical and experimental follow similar trends for the whole $K\mathrm{C}$ range.

In general, the numerically predicted drag and inertia coefficients seem to be less sensitive to changes in the Reynolds number than that of the experimental measurements obtained by Sarpkaya (1976).

3.6.3 Flow regimes

At small values of $K\mathrm{C}$ the fluid motion is small compared to the width of the cylinder, and the vortex particles stay in the vicinity of the cylinder. This is illustrated in Figure 3.15, where the position of the point vortices is shown for a circular cylinder in a planer oscillatory flow with $K\mathrm{C} = 1.5$. The arrows in the figure indicate the direction and velocity magnitude of the surrounding fluid. We observe that the vortex particles are concentrated into blobs on each side of the cylinder, moving with the ambient flow.

As the value of $K\mathrm{C}$ increases the flow separates from the cylinder, creating a pair of symmetric, attach vortices at the downstream side of the cylinder (Williamson (1985)). When the ambient flow change direction, these vortices are pushed on either side of the cylinder, forming two vortex pairs with the newly created vortices. These vortex pairs eventually leave the cylinder at the end of the half cycle. As

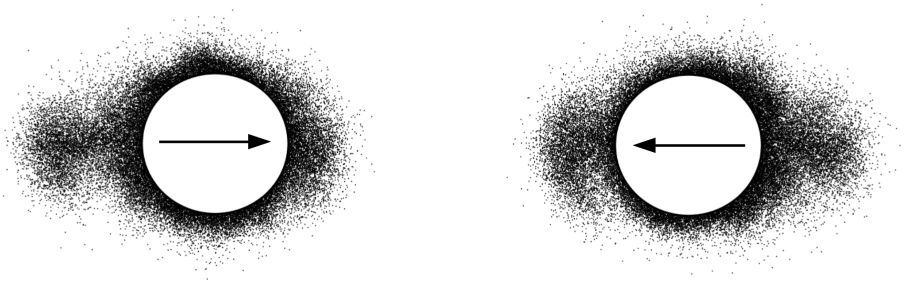

Figure 3.15: Point vortex positions for $K\mathrm{C} = 1.5$ and $\beta = 500$. Arrows indicate the direction and magnitude of the ambient flow.

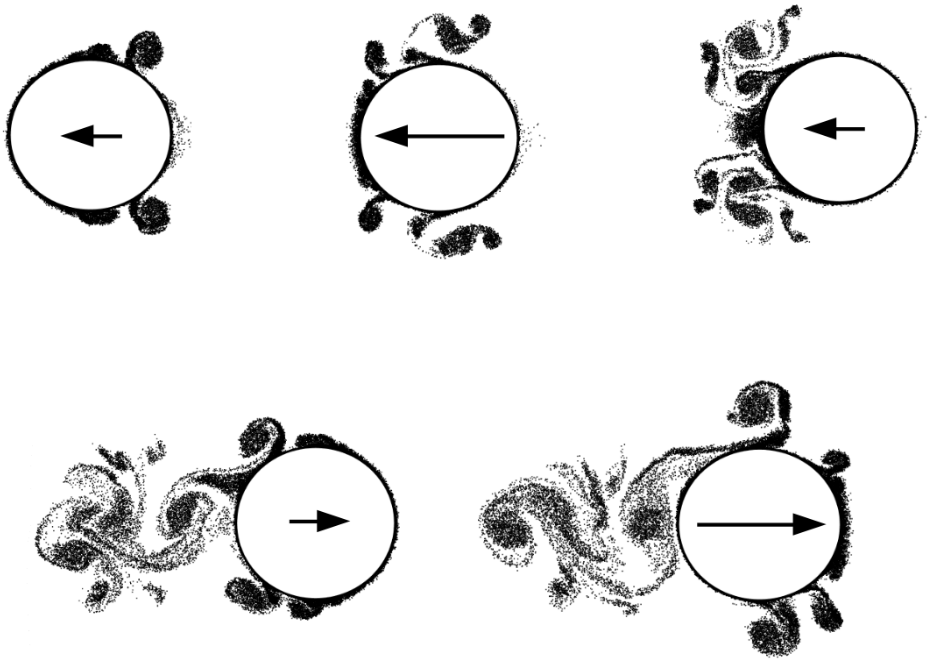

Figure 3.16: Point vortex positions for $KC = 4$ and $\beta = 2500$. Arrows indicate the direction and magnitude of the ambient flow.

KC reach approximately 4, dependent on the Reynolds number, the attach vortices are no longer symmetric and do not form simultaneously. The vortex particle positions for this case is shown in Figure 3.16.

When KC further increase the flow becomes less organized, and as KC becomes larger then about 7 the vortex shedding pattern changes. This is illustrated in Figure 3.17. Within this flow regime, $7 < KC < 15$, the vortices are shedded on either the upper or lower side of the cylinder. Shifting from one side to side (Williamson (1985)). The newly shedded vortices create a vortex pair, which is convected away from the cylinder by its self-induced velocity field. Experiments by Williamson (1985) showed the development of a transverse vortex street in this KC range. This is not seen in Figure 3.17. The reason may be that the simulation was terminated too early for such a vortex street to form. The simulation was stopped after only 8 complete flow cycles as the storing of the vortex particle positions took a considerable amount of time and memory as the number of vortices increased. There were approximately 600000 vortex particles at the end of the simulation.

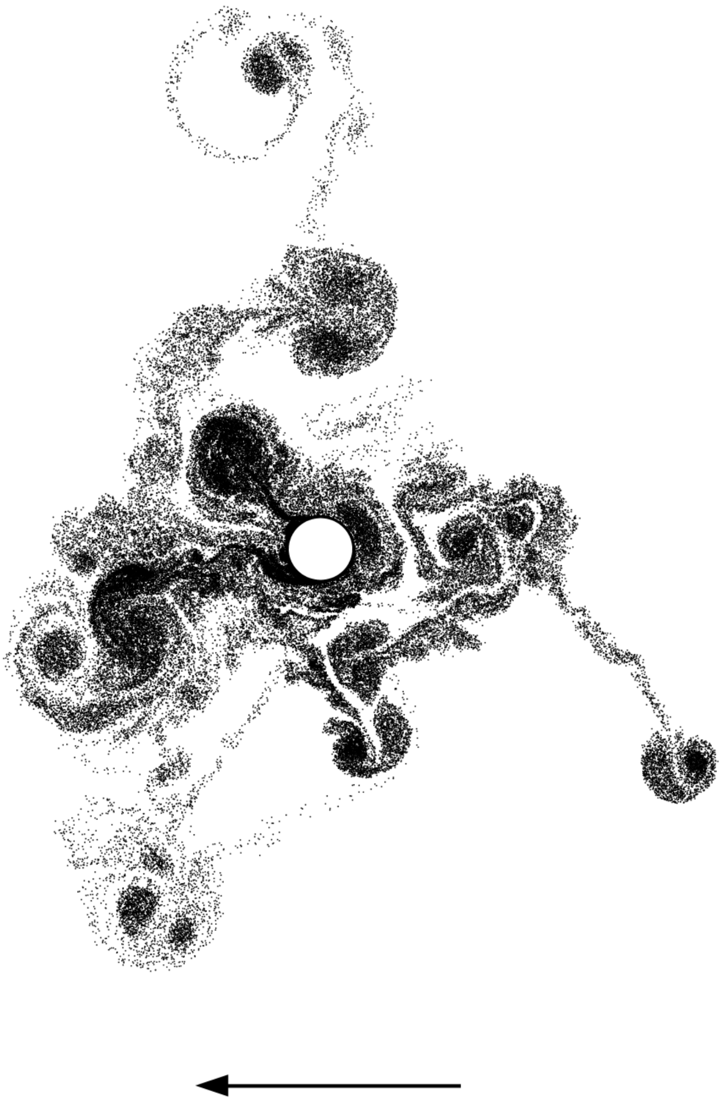

For caption see next page.

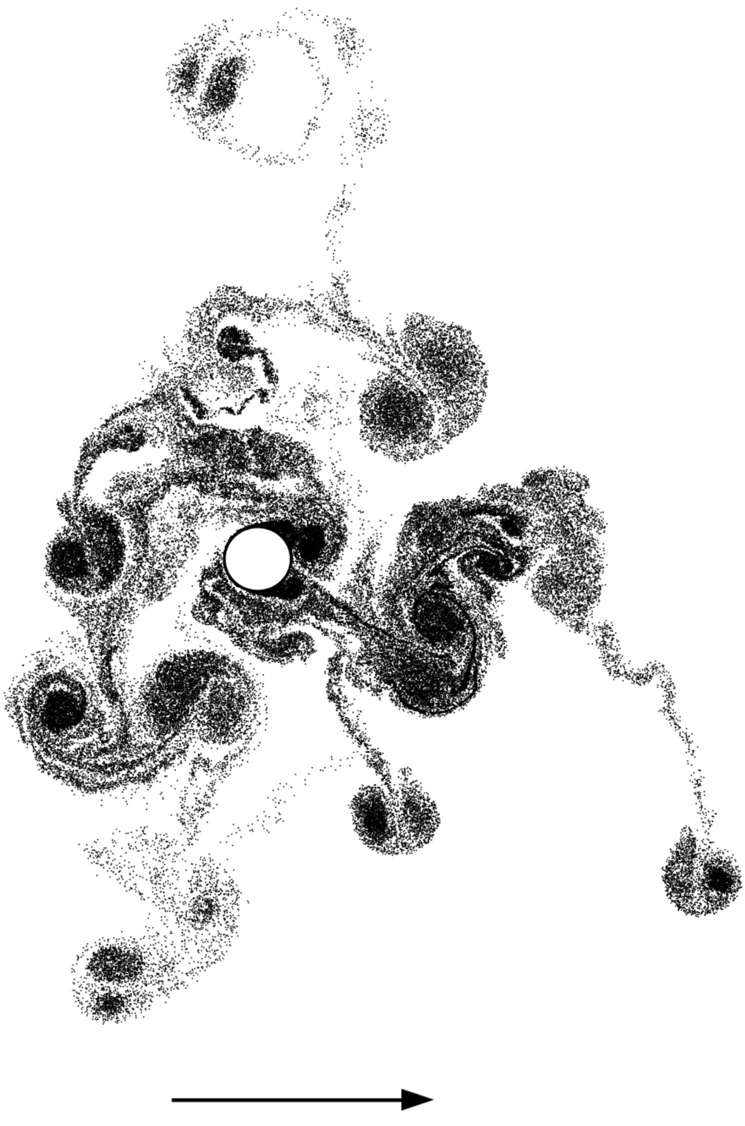

Figure 3.17: Point vortex positions for $KC = 10$ and $\beta = 1000$. Arrows indicate the direction and magnitude of the ambient flow.

3.7 Performance test

The motivation for implementing the Vortex-In-Cell algorithm instead of using commercially available solvers such as STAR-CCM+ and ANSYS Fluent is the relatively low computational cost related to the method. To get a notion of the efficiency of the VIC method, timed numerical experiments were carried out, see Table 3.4. All timed experiments were run over 6 complete flow cycles on a 2-core Intel i7 machine with 8 GB of RAM. The implementation was compiled with the gfortran compiler version 5.4.0 and optimization flag '-O2'. $r_o = 12.5D$ were used in all simulations. Although of interest, no attempts to compare the execution time of the present method with traditional Eulerian solvers were made.

It should be noted that the main focus during the present work has been to implement the VIC method as presented by Scolan (1991). More efficient versions of the VIC method have been developed, as mentioned in the introduction of this chapter. Such strategies have not been explored due to time limitations and the author's limited programming experience.

Figure 3.18 shows the execution time in minutes as a function of the total number of grid points, M. The operational count of the present method increase with $M \log M$. Because of this, we expect the execution time to increase significantly as the mesh is refined. This is observed when studying Figure 3.18.

Table 3.4: Summary of grid parameters and time step used to test the execution time of the present VIC program.

Run	N_r	N_θ	n_t
1	100	128	100
2	300	256	100
3	400	512	100
4	100	256	100
5	100	256	200
6	100	256	300
7	100	256	400
8	100	256	500

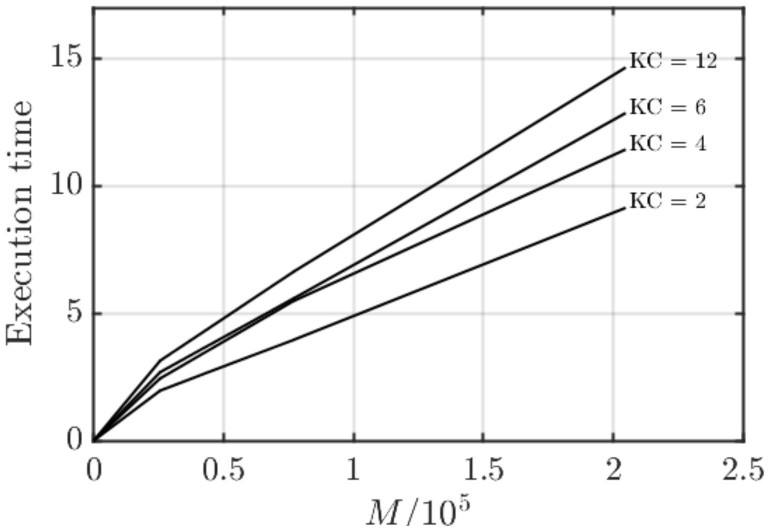

Figure 3.18: Execution time in minutes versus number of grid nodes $M = N_r \cdot N_\theta$ for four different KC values. Run 1 to 3.

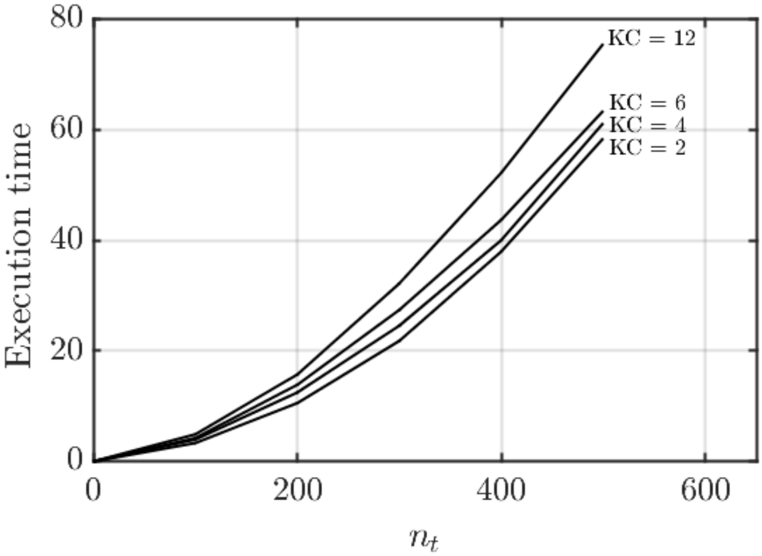

Figure 3.19: Execution time in minutes versus number of time steps per flow cycle, n_t, for four different KC values. Run 4 to 8.

As KC increases the vortex particles move further away from the cylinder. Fewer particles cross the cylinder surface and the simplified abortion scheme become less effective. This in turn results in a larger number of computational elements to be present in the computational domain. Thus suggesting an large increase of the execution time as KC increase. This is also seen in Figure 3.18. Comparing the execution time for the simulations carried out at $KC = 2$ and 12 we observe an increase of more than 50%, independent of grid refinement.

The execution time in minutes as a function of the time step is presented in Figure 3.19. The effect of decreasing the time step is clearly visible. As the time step decrease, one may expect a linear increase of the execution time, since the number of computation increase linearly with n_t. However, the execution time seems to be proportional to n_t^2. As the VIC-program progress in time, more vortices are produced along the surface of the cylinder to enforce the no-slip boundary condition. This implies that the number of vortex particles present in the computational domain is proportional to n_t. As the computational count of the present method is proportional to N_v^2, the increased number of vortex particles yields a significant rise in the execution time.

It is worth noting that the execution time for run 5, representative for the remaining part of the present work, was between 11 and 16 minutes.

Chapter 4

Computation of Wave Forces

4.1 Combined VIC-FNV model

Cartesian coordinates (x, y, z) are defined with positive x-direction in the wave propagation direction. The z-axis coincide with the center axis of the cylinder, with positive direction upwards. Furthermore, $z = 0$ and $z = h$ corresponds to the sea floor and the mean free surface, respectively. See Figure 4.1. Then the expression for the total in-line force according to the generalized FNV theory (eq. 2.48) is restated in the following manner,

$$F_x = F^1 + F^2 + F^3 \tag{4.1}$$

where F^1, F^2 and F^3 are defined in equation 4.2 to 4.4.

$$F^1 = \int_0^\zeta \Big(2\rho\pi a^2 \frac{\partial u}{\partial t}\Big) dz \tag{4.2}$$

$$F^2 = \int_0^\zeta \Big(\rho\pi a^2 \Big(u\frac{\partial u}{\partial x} + w\frac{\partial u}{\partial z}\Big) + a_{11} w \frac{\partial u}{\partial z}\Big) dz \tag{4.3}$$

$$F^3 = \rho\pi a^2 \frac{4}{g} u^2 \frac{\partial u}{\partial t}\Big|_{z=h,x=0} \tag{4.4}$$

Here equation 4.2 represents the asymptotic solution of the Morison equation within potential flow theory. 4.3 represents the nonlinear force terms due to the linear diffraction potential ϕ_D and 4.4 represents the forces due to the nonlinear diffraction potential ψ.

To account for viscous forces acting on the cylinder, the linear forcing term F^1, is replaced by a force term F_{VIC}, computed by the two-dimensional VIC program presented in the previous chapter. Equation 4.1 then becomes equation 4.5,

$$F_x = F_{VIC} + F^2 + F^3 \tag{4.5}$$

which will be referred to as the combined VIC-FNV model.

To evaluate F_{VIC} the cylinder is discretized into m strips, over which we assume the forces to be constant, as illustrated in Figure 4.1. To reduce the computational cost, a stretched mesh is used according to equation 4.6.

$$\Delta z_i = \alpha^{i-1} \Delta z_1 \tag{4.6}$$

Here the Δz_i is the thickness of the i^{th} strip counted from the sea floor, α is the axial contraction factor and Δz_1 is the thickness of the strip touching the seabed, defined as in equation 4.7.

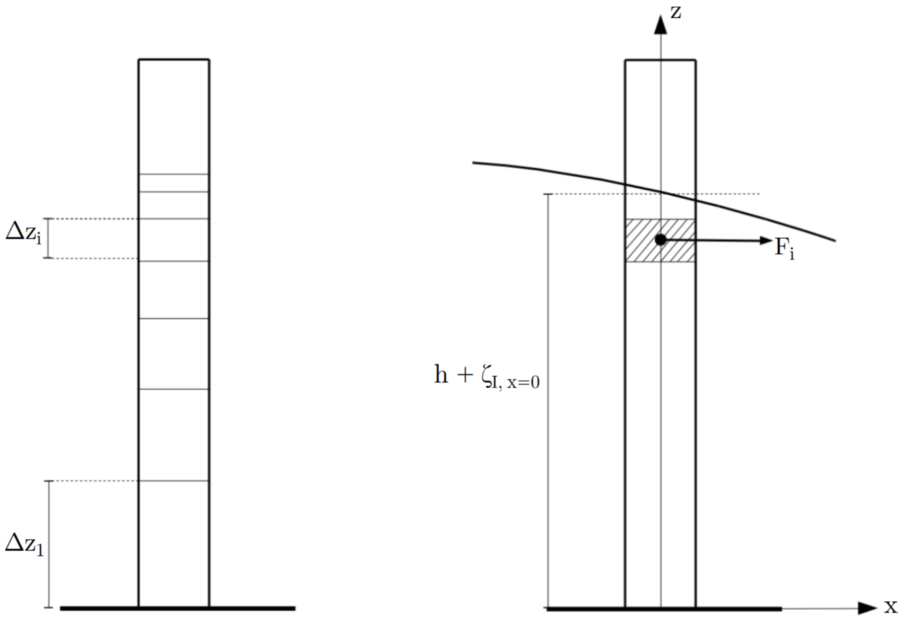

Figure 4.1: Right; illustration of the discretization of the cylinder into m strips. Left; description of the Cartesian coordinate system and load conversions.

$$\Delta z_1 = \frac{(\alpha - 1)\zeta_{Crest}}{\alpha^{m+1} - 1} \tag{4.7}$$

Here ζ_{Crest} is the distance from the sea floor to the wave crest.

The use of a stretched mesh is explained by the fact that the wave kinematics change more rapidly with z close to the surface than at the sea floor. Hence a finer mesh is needed in the surface zone. We further define two separate computational domains, D_1 and D_2. D_1 covers the part of the cylinder where $0 \leq z \leq \zeta_{Trough}$, in other words, the part of the cylinder which remains submerged during the complete flow cycle. The reaming part of the cylinder is covered by D_2 , that is to say, $\zeta_{Trough} \leq z \leq \zeta_{Crest}$. In the submerged domain, D_1, the ambient flow past a strip is treated as a oscillatory flow. In the surface domain, D_2, the flow is treated as an abruptly started uniform current. This is illustrated in Figure 4.2.

In the submerged domain, D_1, calculations are carried out over several flow cycles, to remove transient effects occurring during the first few cycles. Typically, 6-8 were simulated. In the surface domain, D_2, force calculations were only carried out as long as the center of the strip was submerged, otherwise the forces were assumed to be zero.

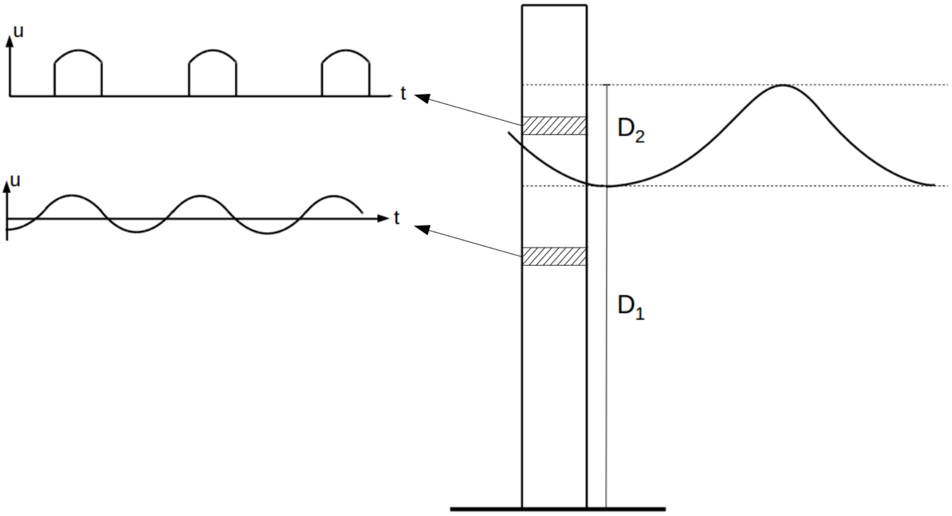

Figure 4.2: Illustration of the ambient flow past strips in the submerge domain D_1 and the surface domain D_2.

The boundary condition for each strip, u, was found using Stokes fifth order wave theory, as presented in Section 2.2.4. The horizontal particle velocity was evaluated at the geometric center of each strip and extrapolated to the outer boundary r_o.

When the time history of the in-line force for each strip is computed, the total force F_{VIC} is simply found by summing the stripwise contributions in the following manner.

$$F_{VIC} = \sum_{i=1}^{m} F_i \Delta z_i \tag{4.8}$$

The distributed load term, F^2, is found by direct numerical integration of equation 4.3, while F^3 is found directly from equation 4.4. The wave kinematics and free surface elevation is obtained using fifth order Stokes theory. Since Stokes wave theory is only valid up to the mean free surface, all quantities contributing to the load term F^2 and the boundary condition for F_{VIC} must be Taylor expanded for $h < z \leqslant |\zeta|$. If f represent either u, w, $\partial u/\partial t$, $\partial u/\partial x$, $\partial u/\partial z$, the Taylor expansion consistent with fifth order Stokes theory is as follows

$$\begin{aligned} f(z) =&(f_1+f_2+f_3+f_4+f_5)\Big|_{z=0} + z\frac{\partial(f_1+f_2+f_3+f_4)}{\partial z}\Big|_{z=0} + ... \\ &\frac{z^2}{2!}\frac{\partial^2(f_1+f_2+f_3)}{\partial z^2}\Big|_{z=0} + \frac{z^3}{3!}\frac{\partial^3(f_1+f_2)}{\partial z^3}\Big|_{z=0} + \frac{z^4}{4!}\frac{\partial^4 f_1}{\partial z^4}\Big|_{z=0} \qquad z>0 \end{aligned} \tag{4.9}$$

where f_i refers to the i^{th} order Stokes wave theory. A time series of the total horizontal load F_x is in turn constructed with equation 4.5, and the three first harmonics are extracted by band-pass filtering.

4.2 Test conditions

The wave conditions used in the present work were chosen such that they match the environmental condition tested by Kristiansen and Faltinsen (2017). Thus, only regular waves were tested at two water depths, $h/a = 7.83$ and $h/a = 5.51$. The main focus was on the wave conditions where discrepancies in the theoretical third harmonic were observed.

Table 4.1: Test condition parameters. T, KC, Ur and Re are given for a linear wave steepness $H_1/L = 1/25$, at two water depths.

	$h/a = 5.51$				$h/a = 7.83$			
ka	T	KC	Ur	$Re/10^3$	T	KC	$U\mathrm{r}$	$Re/10^3$
0.30	3.73	1.62	2.22	33.3	3.67	1.50	0.77	31.6
0.28	3.93	1.78	2.73	35.1	3.81	1.62	0.95	32.9
0.26	4.12	1.99	3.42	37.2	3.97	1.77	1.19	34.4
0.24	4.35	2.24	4.35	39.9	4.15	1.95	1.51	36.3
0.22	4.61	2.58	5.67	43.3	4.37	2.18	1.96	38.5
0.20	4.93	3.05	7.60	47.7	4.64	2.48	2.61	41.4
0.18	5.33	3.71	10.52	53.9	4.96	2.89	3.59	45.0
0.16	5.81	4.74	15.25	63.0	5.37	3.47	5.13	50.0
0.14	6.42	6.45	23.55	77.8	5.90	4.37	7.72	52.0
0.12	7.16	9.71	40.21	104.8	6.61	5.88	12.46	68.8
0.10	8.00	15.94	80.63	154.0	7.56	8.85	22.41	90.4

The wave steepness H_1/L range from 1/40 to 1/20, where H_1 is the linear wave height obtained from linear wave theory, whereas the ka range was 0.1 to 0.3. The test condition parameters are summarized in Table 4.1.

Note that most of the presently considered wave conditions are within the suggested upper limit provided by Hedges (1995). Significant distortions of the theoretical wave form was observed for the longest wave condition at $h/a = 5.51$. The results from this wave condition were therefore neglected.

Values of the Keulegan-Carpenter numbers are illustrated for relevant wave conditions in Figure 4.3. Solid lines represent $K\mathrm{C}$ where the maximum horizontal velocity at the incident wave crest according to Stokes fifth order theory is used. The dashed lines present $K\mathrm{C}$ obtained using the maximum velocity in the submerged domain, D_1, that is, the horizontal velocity at $z = \zeta_{Trough}$ underneath the wave crest.

The results presented in Section 3.6 indicates that the accuracy of the present VIC program is questionable as local $K\mathrm{C}$ numbers become larger than about $5-6$. Figure 4.3 illustrates that this will only occur for the longest and steepest wave conditions tested in the present work. Further, the local $K\mathrm{C}$ number will generally be less than what indicated in Figure 4.3 since the horizontal particle velocity decreases as one moves downwards through the water column.

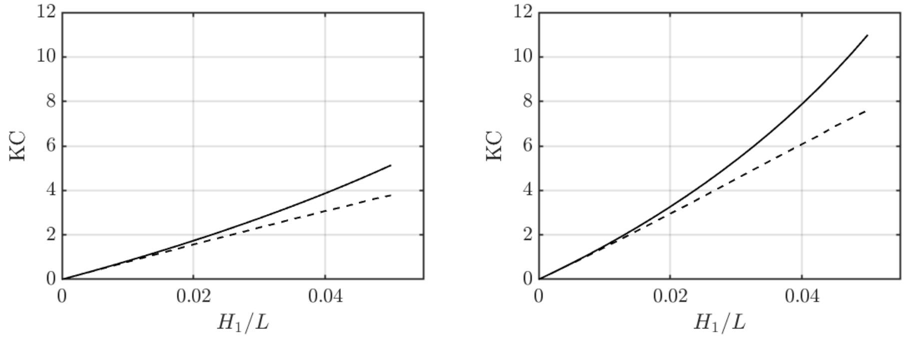

Figure 4.3: Example illustrating different KC numbers for linear wave steepness ranging from 0 to 1/20 at water depth $h/a = 7.83$, for two dimensionless wave numbers, $ka = 0.15$ (left) and $ka = 0.105$ (right). (———), horizontal velocity at the incident wave crest according to Stokes fifth order theory is used; (- - - - -), the maximum velocity in the submerge domain, D_1, is used.

4.3 Scaling of viscosity

The experiments performed by Kristiansen and Faltinsen (2017) were executed on a model with a diameter of 0.144m, whereas the current implementation of the VIC method assumes the diameter to be 2m. To achieve similarity in forces between the model scale and simulation scale, equality of KC and Re is needed. Equal KC in the two scales is obtained through equality in Froude number, defined in equation 4.10.

$$Fn = \frac{U_o}{\sqrt{gD}} \tag{4.10}$$

Assuming constant Froude number and geometric similarity with scale ratio $\Lambda = D_s/D_m$ one can obtain the following relationship between velocities in model scale, denoted by the subscript m, and simulation scale, denoted by the subscript s.

$$\begin{gathered} \frac{U_{o,m}}{\sqrt{gD_m}} = \frac{U_{o,s}}{\sqrt{gD_s}} \\ \Downarrow \\ U_{o,m} = \sqrt{\Lambda} U_{o,s} \end{gathered} \tag{4.11}$$

Other physical parameters can be derived through dimensional analysis, some of which are presented in Table 4.2.

Similarity in Froude number will generally imply dissimilarity in Reynolds number. This problem may be overcome by introducing an artificial kinematic viscosity through Froude scaling of ν. The relationship for the correct Froude scaling of viscosity is derived from the basic relations of distance and time, given in Table 4.2, as follows

$$\nu_s[\frac{m^2}{s}] = \frac{\Lambda^2}{\sqrt{\Lambda}}\nu = \Lambda^{3/2}\nu \tag{4.12}$$

The viscosity of freshwater is approximately 10^{-6}, neglecting variation due to temperature, while the scale ratio Λ is found to be

$$\Lambda = \frac{D_s}{D_m} = \frac{2}{0.144} = 13.9 \tag{4.13}$$

Equation 4.12 then yields $\nu_s \approx 5.2 \cdot 10^{-5}$.

Table 4.2: Scaling factor for relevant parameters when applying Froude scaling (Steen (2014)).

Length $[m]$	Λ
Velocity $[m/s]$	$\sqrt{\Lambda}$
Time $[s]$	$\sqrt{\Lambda}$

Chapter 5

Results

5.1 Comparison of F^1 and F_{VIC}

An example of the time-history of the total in-line force acting on a monopile and its three first harmonics over three wave periods are presented in Figure 5.1. The dashed lines represent the in-line force as predicted by the asymptotic Morison equation, the term F^1 in the FNV model. The solid lines show the in-line force obtained using the VIC program stripwise along the cylinder, as described in Section 4.1.

From the comparison of the total horizontal force, the first plot in Figure 5.1, noticeable differences between the two force calculation methods are observed. First of all, one sees that the VIC method predict larger forces in the wave propagation direction than in the negative x-direction, whereas the asymptotic Morison equation yields equal force amplitudes in both directions. Secondly, a slight phase difference is observed. This phase shift is expected since the asymptotic Morison equation does not account for viscous forces, which are usually assumed to be 90 degrees out of phase with the inertia force.

From the comparison of the three first load harmonics, a reduction of all harmonics is observed. This reduction is associated with a decrease of the numerical predicted inertia force as KC becomes sufficiently large. The largest reduction is observed for the third load harmonic, whereas the differences in the first and second harmonic are less noticeable. The phase shift previously mentioned is seen in all three load harmonics. In general, there is a reduction in all load harmonics for the longest waves, the difference increasing as the waves steepen. The phase difference also increases as the waves become longer and steeper.

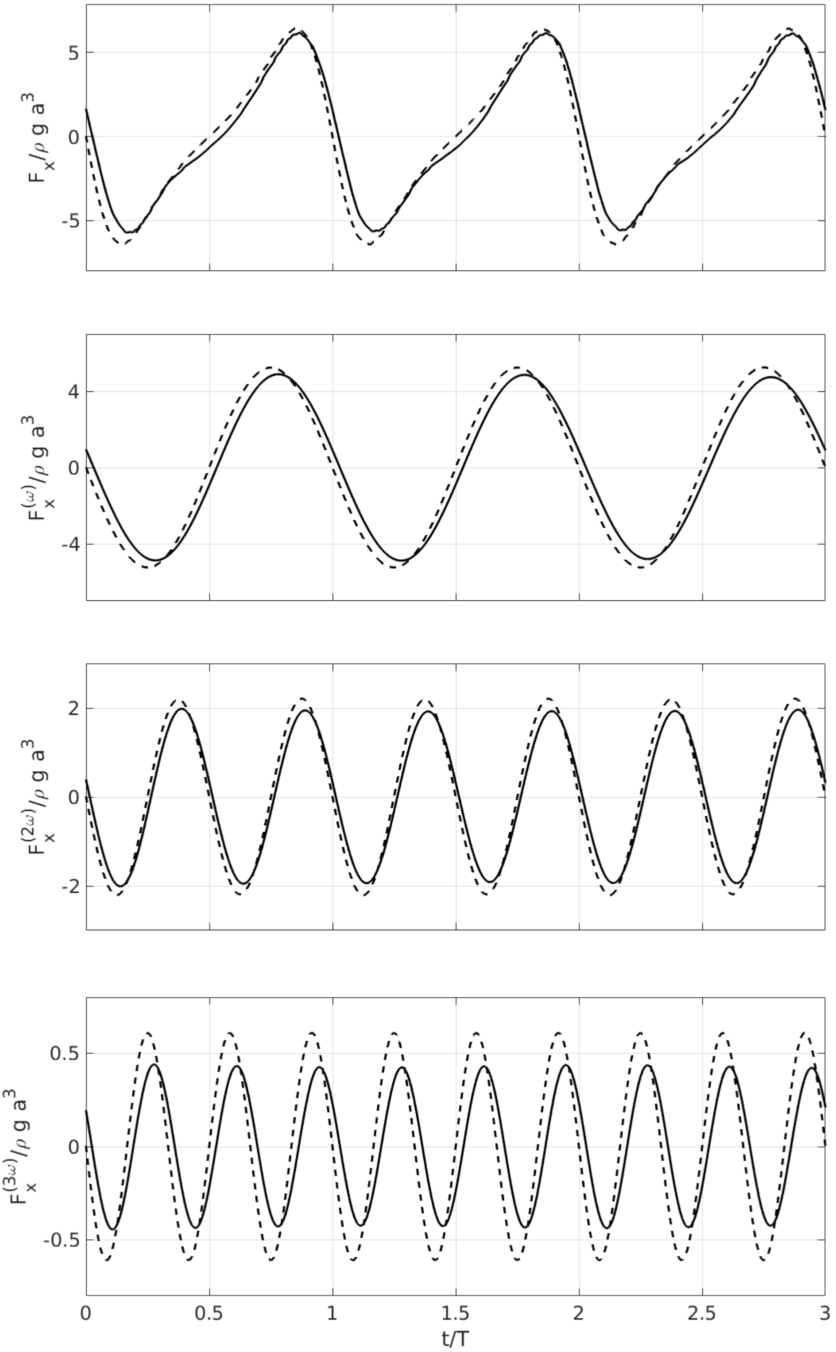

Figure 5.1: Example of the total force, F_x, and the three first load harmonics, F_x^{ω}, $F_x^{2\omega}$ and $F_x^{3\omega}$, of the normalized horizontal force. (- - - - -), asymptotic solution of the Morison equation; (———), force computed with the VIC-program. $ka = 0.105$, $H_1/L = 1/25$ and water depth $h/a = 7.83$.

5.2 Comparison of the FNV method and the combined VIC-FNV model

The amplitude of the first three load harmonics of the horizontal force F_x, for two selected wave steepnesses are shown in Figure 5.2. The dashed and solid lines represent the load harmonics predicted by the generalized FNV method and the combined VIC-FNV model, respectively. The water depth $h/a = 7.83$. Experimental measurements obtained by Kristiansen and Faltinsen (2017) are also provided and are represented by circles.

For the shortest wave conditions the local KC number along the cylinder axis is small. In this range of KC the in-line force is dominated by the inertia component and the viscous force has little effect on the total force predicted by the combined VIC-FNV method. This can be seen in Figure 5.2, as the results obtained by the two methods are in good agreement for $ka > 0.18$, independent of wave steepness. Small differences are observed in the first harmonic, as the results obtained by the combined VIC-FNV model are larger than the results obtained with the FNV model. The estimations of the second and third harmonic obtained by the two methods are indistinguishable in this ka range.

For longer waves, $ka < 0.18$, the agreement between the combined VIC-FNV method and the experimental measurements are good for the wave conditions where no significant discrepancies are observed in the generalized FNV model. As mentioned in the previous section, the third harmonic obtained by the combined method is in general smaller than what is predicted by the FNV model and the difference between the two methods increases with the wave steepness. Note also that the first and second harmonic are smaller for the steepest and longest wave conditions when compared to the analytic FNV model.

For the steepest wave conditions the generalized FNV model, in general, overpredicts the third harmonic. This is clearly seen in Figure 5.3, where a close-up of the amplitude of the third harmonic for $H_1/L = 1/25$ and ka ranging from 0.09 to 0.18 is shown. For the selected wave condition the theoretical prediction of $F_x^{(3\omega)}$ is about twice as large as the experimental measurements. Discrepancies between the combined VIC-FNV method and the experimental measurements are also seen.

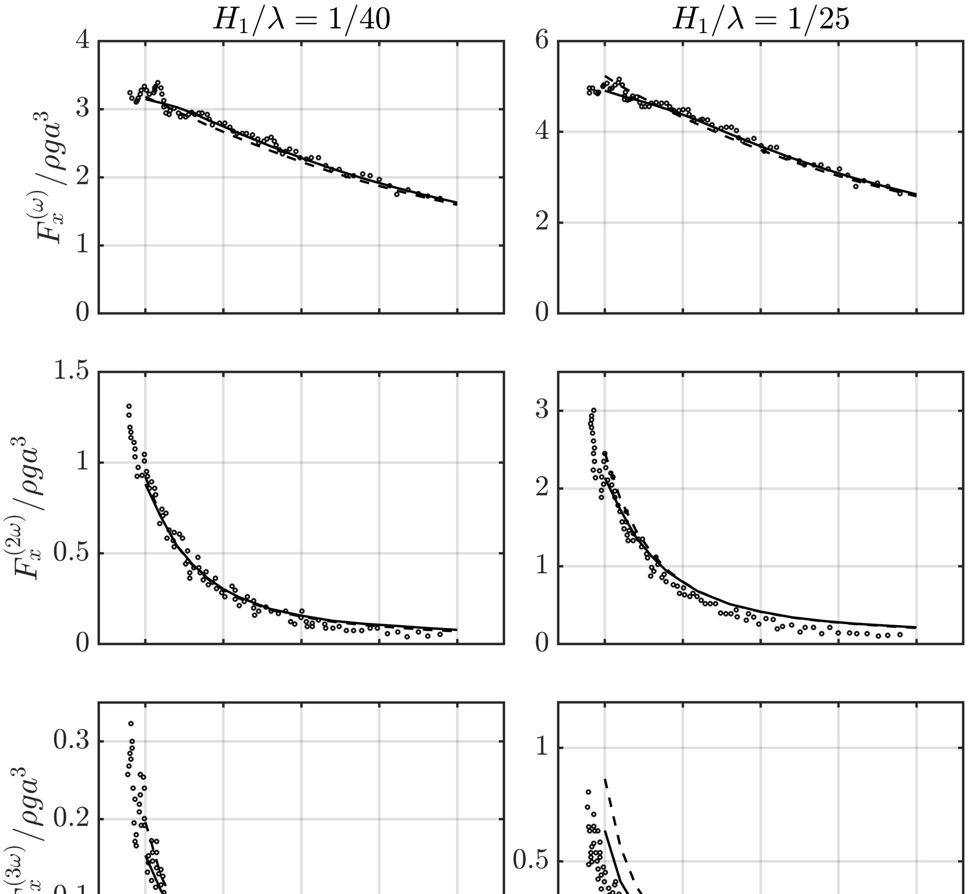

Figure 5.2: Horizontal force amplitude of the first three harmonics due to regular waves as a function of dimensionless wave number ka for wave steepnesses $1/40$ and $1/25$. Water depth $h/a = 7.83$. (- - - - -), FNV theory; (———), combined VIC-FNV method; ○, experimental measurements (Kristiansen and Faltinsen (2017)).

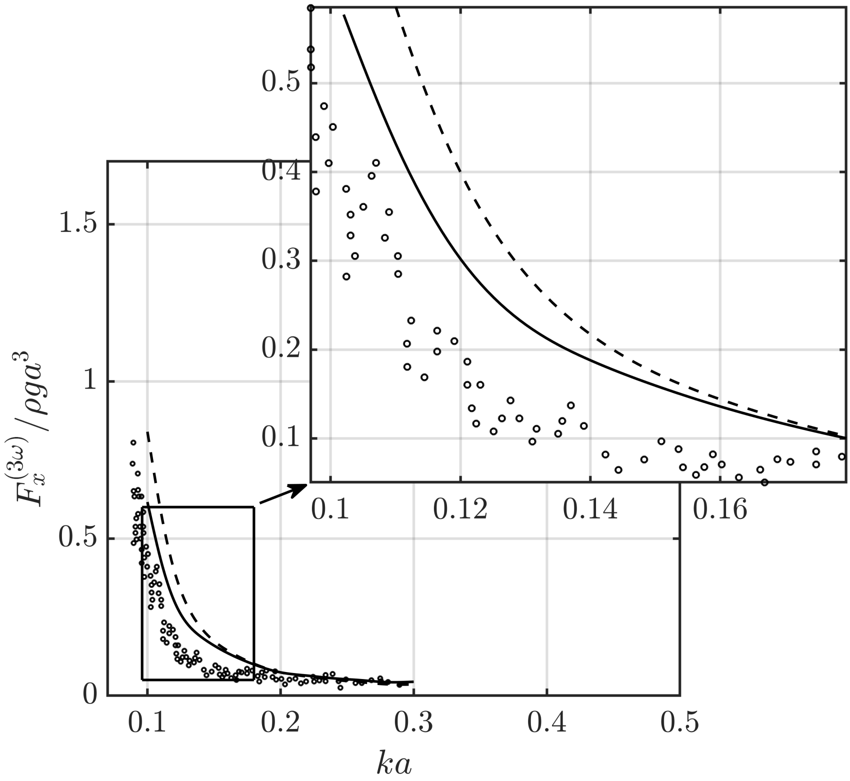

Figure 5.3: Close-up view of the 3^{rd} harmonic versus ka for wave steepness 1/25 and water depth $h/a = 7.83$. (- - - - -), FNV theory; (———), combined VIC-FNV method; ○, experimental measurements (Kristiansen and Faltinsen (2017)).

From the above figure it is observed that both the FNV and VIC-FNV methods diverge from the experimental results at $ka \approx 0.18$. For smaller wave numbers the discrepancies for both methods increase gradually with decreasing ka. The predicted third harmonic by the combined VIC-FNV method is in general closer to the experimental results than that of the FNV method. The difference between the two models being approximately 25% for $ka = 0.1 - 0.13$. This illustrates the general trend in the prediction of the third harmonic: both methods are in close agreement with experimental measurements up to a certain point. Beyond this point both methods overpredict the third harmonic. The combined VIC-FNV method yielding lower predictions of $F_x^{(3\omega)}$ compared to the FNV theory. This trend is further illustrated in Figure 5.4. Here, the amplitudes of the first three harmonics as a function of the linear wave steepness for three different values of ka,

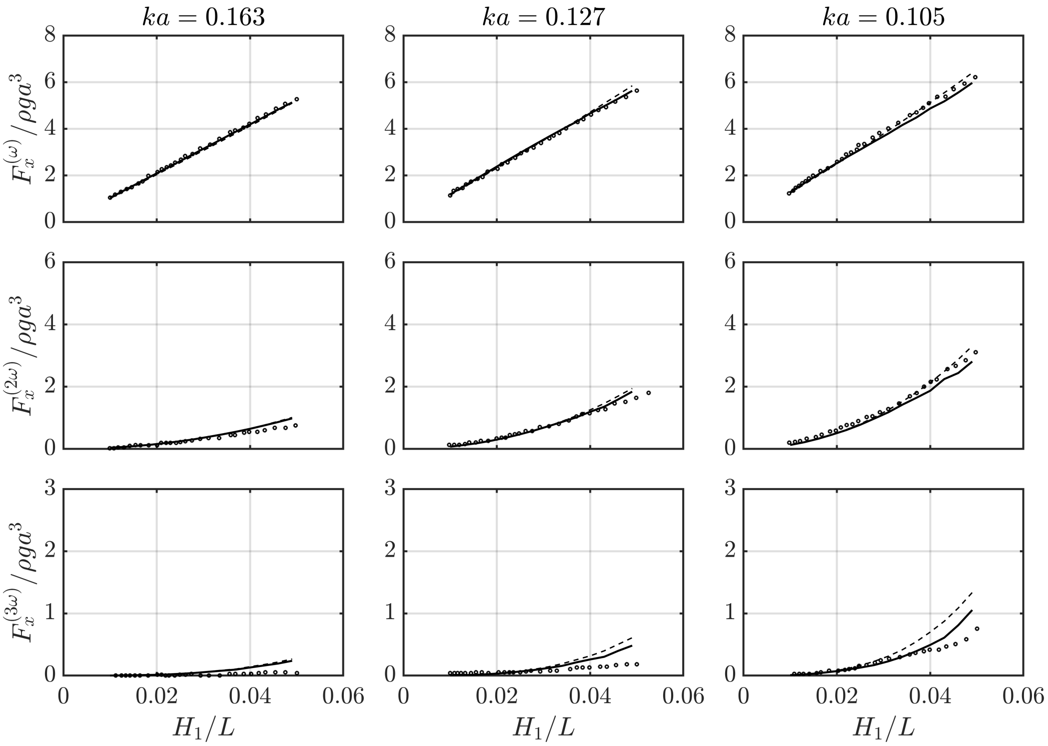

Figure 5.4: Amplitudes of the first three harmonics of the horizontal force due to regular waves at water depth $h/a = 7.83$ versus linear wave steepness at three non-dimensional wave numbers. (- - - - -), FNV theory; (———), combined VIC-FNV method; ○, experimental measurements (Kristiansen and Faltinsen (2017)).

corresponding to long waves, are presented. For $ka = 0.105$ we observe that the combined method yields a somewhat better prediction of the third harmonic. This is, however, not seen for $ka = 0.163$ and 0.127, where both methods diverge from the experimental measurements at $H_1/L \approx 0.03$. Beyond this point, the discrepancies increase gradually with increasing wave steepness for both methods. In Appendix F, results are provided for water depth $h/a = 5.51$. Similar trends are observed. However, the difference between the FNV theory and the combined VIC-FNV method are in general smaller.

The noticeable differences observed between the inviscid FNV theory and the viscous VIC-FNV method, indicate that viscous effects are important when evaluating higher order wave loads on cylinders in long steep waves. It is, however, clear that the combined VIC-FNV method is not able to accurately predict the third harmonic for $H_1/L \geq 1/30 - 1/25$.

The current method assumes the cross-flow principle to be valid, thus neglecting three-dimensional flow effects. Honji (1981) showed that the flow past a circular cylinder in mono-harmonic ambient flow exhibit distinct three-dimensional structure for $K\mathrm{C} \approx 1 - 2$. Visual studies of similar flow conditions carried out by Tatsuno and Bearman (1990) indicates that the flow stays three-dimensional as $K\mathrm{C}$ further increases. Furthermore, the introduction of nonuniform in-flow conditions poses yet another trigger for three-dimensional flow effects. Zdravkovich (1997) reviews the effect of shear flow past fully submerged circular cylinders and describes the occurrence of two secondary flows along the cylinder span. These secondary flows are driven by spanwise pressure gradients established along both the front and rear side of the cylinder. The local pressure is proportional to the local inflow velocity squared. On the side facing the in-flow, the secondary spanwise flow is driven downwards by the pressure gradient, whereas the flow runs upwards at the hind-part of the cylinder.

There are obvious differences between the wave-structure interaction problem and that of a submerged cylinder in mono-harmonic or shear flow, both regarding the in-flow conditions and the effect of the free surface. However, it seems plausible that the flow past a cylinder in waves may behave in a similar fashion. As the waves become steeper the local $K\mathrm{C}$ number along the cylinder axis increase and the velocity profile underneath the wave crest becomes more skewed, suggesting that three-dimensional flow features become more pronounced. Thus the cross-flow assumption may be questionable for the steepest wave conditions.

It shouted be noted that the present implementation of the generalized FNV theory yields, in general, large estimates of the three first load harmonics when compared to the results presented by Kristiansen and Faltinsen (2017). The differences are noticeable for the longest and steepest wave conditions ($H_1/L > 0.035 - 0.04$ and $ka < 0.14 - 0.12$). It is believed that the error originates from the implementation of the fifth order Stokes wave. If true, the load harmonics obtained by the combined VIC-FNV method should also be smaller for these wave conditions, as both methods are affected by the same error. This may imply that the combined VIC-FNV method yields satisfactory estimates of the third load harmonic for steeper wave conditions, then what indicated by Figure 5.2 to 5.4. However, it would also imply that the combined method significantly underpredict the first and second load harmonic for these wave conditions. Further, this does not explain the discrepancies observed for the shorter wave conditions.

5.3 Effect of Reynolds number

Until now, Reynolds numbers equivalent to those present in the experiments performed by Kristiansen and Faltinsen (2017) have been studied. Experiments by Kristiansen et al. (2017) indicated that there are notable Reynolds number effects when evaluating higher harmonic wave loads. To investigate the effect of Re on the combined VIC-FNV method several simulations were carried out. The Reynolds number was changed by increasing or decreasing the kinematic viscosity, see Table 5.1. Simulations were performed for three different values of ka, 0.163, 0.127 and 0.105, at a water depth $h/a = 7.83$. The linear wave steepness ranged from 1/100 to 1/20. Results for all wave conditions are provided in Appendix G.

The first three load harmonics obtained by the combined VIC-FNV method were not significantly affected by changing the Reynolds number. A small increase of the third load harmonic were observed for $ka = 0.105$, illustrated in Figure 5.5, whereas the experimental measurements (Kristiansen et al. (2017)) indicated an distinct reduction of the third harmonic as Re increased. As mentioned before, the KC number along the cylinder axis is in general small, which suggest that inertia forces dominate. The results presented in Section 3.6 indicate that the numerical

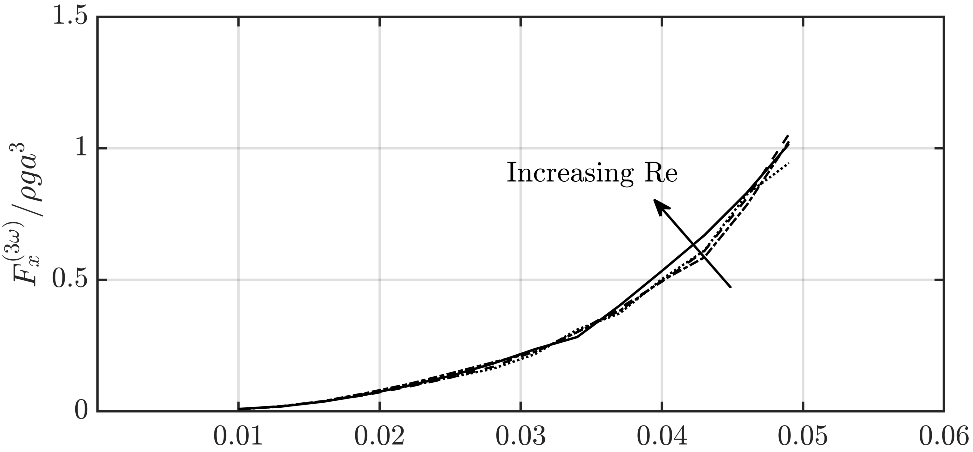

Figure 5.5: Effect of Reynolds number on the third harmonic of the horizontal force as a function of the linear wave steepness. $ka = 0.105$ at water depth $h/a = 7.83$. (———), $v_s = 2.59 \cdot 10^{-5}$; (- - - - -), $v_s = 5.18 \cdot 10^{-5}$; (··········), $v_s = 1.04 \cdot 10^{-4}$; (-·-·-·-·), $v_s = 2.07 \cdot 10^{-4}$.

predicted inertia force does not change significantly with Re at small values of KC. Implying that the force acting on the individual strips is only slightly affected by changes of Re. It is believed that the differences between the experimental and numerical obtained results are due to three-dimensional flow effects not captured by the combined VIC-FNV method.

Table 5.1: Scaling of the kinematic viscosity.

Run	ν_s
1	$2.59 \cdot 10^{-5}$
2	$5.18 \cdot 10^{-5}$
3	$1.04 \cdot 10^{-4}$
4	$2.07 \cdot 10^{-4}$

Chapter 6

Conclusions and Further Work

In this thesis, a new partly numerical method for computing higher harmonic wave loads on vertical, non-moving, surface-piercing circular cylinders based on the FNV theory has been tested. Viscous forces are accounted for by replacing the linear forcing term in the FNV method with a simplified numerical model assuming the cross-flow principle to be valid. The two-dimensional Navier-Stokes equations are solved using the hybrid Eulerian-Lagrangian Vortex-In-Cell method in combination with the Operator Splitting Technique.

The Vortex-In-Cell program was verified by running several numerical experiments of the flow past a circular cylinder in impulsively started and planar oscillatory flow. Comparison with visualization experiments (Bouard and Coutanceau (1980)) showed that the present program accurately predicts the development of both the large primary and the secondary eddies. However, as the Reynolds number increased a fine grid was needed to correctly reproduce the complex flow features in the vicinity of the cylinder. The time development of the in-line force was computed at several Reynolds numbers. These were found to be in good agreement with those obtained by Koumoutsakos and Leonard (1995). For oscillatory flows, results were presented in the form of the Morison force coefficients, C_D and C_M, and compared to measurements by Sarpkaya (1976). The numerically predicted drag coefficient was in good agreement with the empirical data for $K\mathrm{C} < 5 - 6$, whereas the inertia coefficient was underpredicted by $5\% - 10\%$ in this KC range. For larger values of KC neither of the force coefficients were well described by the present Vortex-In-Cell program. Discrepancies between the VIC-OST method and experimental data have been noted by several authors (Skomedal et al. (1989); Lin et al. (1996)). These discrepancies may be due to three-dimensional effects or other factors which may affect the experimental measurements, or it may be due to the method itself. A comparative study of the VIC-OST method and other numerical schemes is needed to resolve this question.

Computations of the in-line wave forces, using the partly numerical VIC-FNV method, were performed for wave conditions where the third harmonic of the FNV theory is known to deviate from experimental results. The load harmonics were compared to the generalized FNV theory and experimental measurements (Kristiansen and Faltinsen (2017)). Load terms oscillating with ω, 2ω and 3ω were studied. The main focus was on the amplitude of the third load harmonic.

The first three load harmonics obtained by the combined VIC-FNV method were indistinguishable from those obtained by the FNV method for short waves, independent of wave steepness. For lower values of ka, the combined VIC-FNV method gave, in general, lower estimates of all load harmonics. However, the VIC-FNV method significantly overpredicted the third harmonic for the steepest waves. Diverging from the experimental measurements at similar wave steepnesses as the generalized FNV theory. Thus flow separation alone seems not to explain the discrepancies in the FNV model. The rationale of the discrepancies has not been investigated. However, it is believed that the onset of three-dimensional flow effects may be the reason.

Some uncertainties are related to the accuracy of the current VIC program and the implementation of the wave kinematics. It is therefore recommended to perform wave computations using a similar approach applying a well proven Eulerian solver, such as OpenFOAM. Different discretization strategies of the cylinder have not been evaluated in the present study. As this may affect computed wave forces, other strategies such as a Lagrangian discretization approach should be tested. Future work should also seek to capture three-dimensional flow effects.

Bibliography

Anderson, E., Bai, Z., Bischof, C., Blackford, S., Demmel, J., Dongarra, J., Croz, J. D., Greenbaum, A., Hammarling, S., McKenney, A., Sorensen, D., 1991. Lapack users' guide Accessed: http://www.netlib.org/lapack/lug/.

Bachynski, E., Kristiansen, T., Thys, M., October 2017. Experimental and numerical investigations of monopile ringing in irregular finite-depth water waves. Applied Ocean Research 68.

Bearman, P. W., Downie, M. J., Graham, J. M. R., Obasaju, E. D., May 1985. Forces on cylinders in viscous oscillatory flow at low keulegan-carpenter numbers. Journal of Fluid Mechanics 154 (-1), 337–356.

Birdsall, C. K., Fuss, D., 1969. Clouds-in-clouds, clouds-in-cells physics for many-body plasma simulation. Journal of Computational Physics 3 (4), 494 – 511.

Bouard, R., Coutanceau, M., 1980. The early stage of development of the wake behind an impulsively started cylinder for $40 < \mathrm{re} < 10^4$. Journal of Fluid Mechanics 101 (3), 583–607.

Briley, W. R., 1971. A numerical study of laminar separation bubbles using the navier-stokes equations. Journal of Fluid Mechanics 47 (4), 713–736.

C. MacCamy, R., A. Fuchs, R., 12 1954. Wave forces on piles: A diffraction theory, 21.

Chaplin, J. R., RAINEY, R. C. T., YEMM, R. W., 1997. Ringing of a vertical cylinder in waves. Journal of Fluid Mechanics 350, 119–147.

Chorin, A. J., 1973. Numerical study of slightly viscous flow. Journal of Fluid Mechanics 57 (4), 785–796.

Christiansen, I., 1973. Numerical simulation of hydrodynamics by the method of point vortices. Journal of Computational Physics 13 (3), 363–379.

Dean, R. G., 1991. Water wave mechanics for engineers and scientists, 2nd Edition. Vol. 2 of Advanced series on ocean engineering. World Scientific, Singapore.

Faltinsen, O. M., 1990. Sea loads on ships and offshore structures. Cambridge ocean technology series. Cambridge University Press, Cambridge.

Faltinsen, O. M., February 1999. Ringing loads on a slender vertical cylinder of general cross- section. Journal of Engineering Mathematics 35 (1), 199–217.

Faltinsen, O. M., Newman, J. N., Vinje, T., April 1995. Nonlinear wave loads on a slender vertical cylinder. Journal of Fluid Mechanics 289 (-1), 179–198.

Fenton, J., 1985. A fifth order stokes theory for steady waves. Journal of waterways, port, coastal and ocean engineering 111 (2), 216–234.

Fenton, J., 1990. Nonlinear wave theories. the sea: ideas and observations on progress in the study of the sea. Ocean Engineering Science 9, 3–25.

Grue, J., Bjorshol, G., Strand, O., 1993. Nonlinear wave loads which may generate ‘ringing’ responses of offshore structures. In International Workshop on Water Waves and Floating Bodies (IWWWFB), Japan.

GWEC, 2017. Global wind report. Annual Market Update 2017, Global Wind Energy Council Accessed July 2018: http://gwec.net/global-figures/global-offshore/.

Hedges, T. S., 1995. Regions of validity of analytical wave theories. Ice Proceedings Water Maritime and Energy 112 (2), 111 – 114.

Heptonstall, P., 2007. A Review of Electricity Unit Cost Estimates.

Honji, H., 1981. Streaked flow around an oscillating circular cylinder. Journal of Fluid Mechanics 107, 509–520.

Huseby, M., Grue, J., 2000. An experimental investigation of higher-harmonic wave forces on a vertical cylinder. Journal of Fluid Mechanics 414, 75–103.

Koumoutsakos, P., Leonard, A., 1995. High-resolution simulations of the flow around an impulsively started cylinder using vortex methods. Journal of Fluid Mechanics 296, 1–38.

Kristiansen, T., Bachynski, E. E., Bickert, F., Hniche, A., Kocher, V., Liandrat, A., 2017. Aspects in model testing of a monopile in steep waves. ASME. International Conference on Offshore Mechanics and Arctic Engineering.

Kristiansen, T., Faltinsen, O. M., 2017. Higher harmonic wave loads on a vertical cylinder in finite water depth.

Kudela, H., Kozlowski, T., 2009. Vortex in cell method for exterior problems. Journal of Theoretical and Applied Mechanics 47 (4), 779–796.

Leonard, A., 1985. Computing three-dimensional incompressible flows with vortex elements. Annual Review of Fluid Mechanics 17 (1), 523–559.

Lewis, R. I., 1991. Vortex Element Methods for Fluid Dynamic Analysis of Engineering Systems. Cambridge Engine Technology Series. Cambridge University Press.

Lin, X., Bearman, P., Graham, J., 1996. A numerical study of oscillatory flow about a circular cylinder for low values of beta parameter. Journal of Fluids and Structures 10 (5), 501 – 526.

Malenica, Molin, B., November 1995. Third-harmonic wave diffraction by a vertical cylinder. Journal of Fluid Mechanics 302, 203–229.

Morison, J. R., Johnson, J. W., Schaaf, S. A., O'Brien, M. P., 1950. Force exerted by surface waves on piles. Journal of Petroleum Technology 2.

Natvig, B., Teigen, P., January 1993. Review of hydrodynamic challenges in tlp design. International Journal of Offshore and Polar Engineering 3 (4), 241–249.

Newman, J. N., 1977. Marine hydrodynamics. MIT Press, Cambridge, Mass.

Paulsen, B. T., Bredmose, H., Bingham, H., Jacobsen, N., 2014. Forcing of a bottom-mounted circular cylinder by steep regular water waves at finite depth. Journal of Fluid Mechanics 755, 1–34.

Pettersen, B., 2004. Marin Teknikk 3, Hydrodynamikk. NTNU, Institutt for marin teknikk.

Press, W. H., Teukolsky, S. A., Vetterling, W. T., Flannery, B. P., 1992. Numerical Recipes in FORTRAN: The Art of Scientific Computing, 2nd Edition. Vol. 1 of Fortran Numerical Recipes. Cambridge University Press.

Sarpkaya, T., 1976. Vortex shedding and resistance in harmonic flow about smooth and rough circular cylinders at high reynolds numbers. Tech. rep.

Sarpkaya, T., April 1986. Force on a circular cylinder in viscous oscillatory flow at low keulegancarpenter numbers. Journal of Fluid Mechanics 165 (Apr), 61–71.

Scolan, Y.-M., 1991. Numerical prediction of vortex shedding around arbitrary two-dimensional bodies. NTNU, Institutt for marin teknikk.

Scolan, Y.-M., Faltinsen, O., 1994. Numerical studies of separated flow from bodies with sharp corners by the vortex in cell method. Journal of Fluids and Structures 8 (2), 201–230.

Skjelbreia, L., Hendrickson, J., 1960. Fifth order gravity wave theory. Proceedings 7th conference of coastal engineering, 184–196.

Skomedal, N. G., Vada, T., Sortland, B., 1989. Viscous forces on one and two circular cylinders in planar oscillatory flow. Applied Ocean Research 11 (3), 114 – 134.

Smith, P., Stansby, P., 1989. An efficient surface algorithm for random-particle simulation of vorticity and heat transport. Journal of Computational Physics 81 (2), 349 – 371.

Smith, P., Stansby, P., 1991. Viscous oscillatory flows around cylindrical bodies at low keulegan-carpenter numbers using the vortex method. Journal of Fluids and Structures 5 (4), 339–361.

Smith, P. A., Stansby, P. K., 1988. Impulsively started flow around a circular cylinder by the vortex method. Journal of Fluid Mechanics 194, 45–77.

Steen, S., 2014. Experimental Methods in Marine Hydrodynamics. Akademika forlag, Nardoveien 12, 7005 Trondheim.

Suja-Thauvin, L., Krokstad, J. R., Bachynski, E. E., de Ridder, E.-J., December 2017. Experimental results of a multimode monopile offshore wind turbine support structure subjected to steep and breaking irregular waves. Ocean Engineering 146, 339–351.

Sumer, B. M., Fredsøe, J., 2006. Hydrodynamics around cylindrical structures, revised. Edition. Vol. v. 26 of Advanced Series on Ocean Engineering. World Scientific Publishing, London.

Swarztrauber, P. N., 1982. Vectorizing the ffts, in parallel computations. Academic Press, 51–83.

Tatsuno, M., Bearman, P. W., 1990. A visual study of the flow around an oscillating circular cylinder at low keulegan–carpenter numbers and low stokes numbers. Journal of Fluid Mechanics 211, 157–182.

Wang, C.-Y., 1968. On high-frequency oscillatory viscous flows. Journal of Fluid Mechanics 32 (1), 55–68.

White, F. M., 2006. Viscous fluid flow, 3rd Edition. McGraw-Hill series in mechanical engineering. McGraw-Hill Higher Education, Boston.

Williamson, C. H. K., 1985. Sinusoidal flow relative to circular cylinders. Journal of Fluid Mechanics 155, 141–174.

Zdravkovich, M. M., 1997. Flow around circular cylinders : Vol. 1 : [Fundamentals]. Oxford University Press, Great Clarendo Street, Oxford OX2 6DP.

Appendix

Appendix A : Solution of the Poisson equation

In polar coordinates the Poisson equation may be written as equation A.1.

$$\frac{\partial^2 \psi}{\partial r^2} + \frac{1}{r}\frac{\partial \psi}{\partial r} + \frac{1}{r^2}\frac{\partial^2 \psi}{\partial \theta^2} = -\xi \tag{A.1}$$

Introducing the modified polar coordinate system $(r^{'}, \theta)$, with uniform mesh size we get equation A.2

$$\frac{\partial^2 \psi}{\partial \theta^2} + a(r^{'})\frac{\partial^2 \psi}{\partial r^{'2}} + b(r^{'})\frac{\partial \psi}{\partial r^{'}} = -r^2\xi \tag{A.2}$$

where

$$a(r^{'}) = \left(r\frac{dr^{'}}{dr}\right)^2 \tag{A.3a}$$

$$b(r^{'}) = r\frac{dr^{'}}{dr} + r^2\frac{d^2r^{'}}{dr^2} \tag{A.3b}$$

$$r = B_m\left(exp^{A_m r^{'}} - 1\right) + 1 \tag{A.3c}$$

Since $\psi(r^{'}, \theta)$ and $\xi(r^{'}, \theta)$ are periodic in the azimuthal direction, with period 2π, we can approximate them by the truncated Fourier series given in equation A.4a and A.4b,

$$\psi(r^{'}, \theta) = \frac{1}{N_\theta}\sum_{k=0}^{N_\theta - 1} \tilde{\psi}_k(r^{'})e^{ik\theta} \tag{A.4a}$$

$$\xi(r^{'}, \theta) = \frac{1}{N_\theta}\sum_{k=0}^{N_\theta - 1} \tilde{\xi}_k(r^{'})e^{ik\theta} \tag{A.4b}$$

where i is the imaginary number defined as $i^2 = -1$ and $\tilde{\psi}_k$ and $\tilde{\xi}_k$ are the k^{th} complex Fourier coefficients of ψ and ξ given by equation A.5.

$$\tilde{\psi}_k(r^{'}) = \sum_{j=0}^{N_\theta - 1} \psi(r^{'}, \theta_j) e^{-ik\theta_j} \tag{A.5a}$$

$$\tilde{\xi}_k(r^{'}) = \sum_{j=0}^{N_\theta - 1} \xi(r^{'}, \theta_j) e^{-ik\theta_j} \tag{A.5b}$$

$\theta_j = 2j\pi/N_\theta$ and N_θ is the number of grid points in the azimuthal direction. The above transformation between the physical and the Fourier space can be efficiently performed using the Fast Fourier Transform (FFT), which has an operational count of $\mathcal{O}(N_\theta \log N_\theta)$. Substituting the expansion given in equation A.4a and A.4b into the Poisson equation and equating the Fourier coefficients, $\tilde{\psi}_k(r^{'})$ and $\tilde{\xi}_k(r^{'})$ satisfies the following second order differential equation

$$-k^2\tilde{\psi}_k(r^{'}) + a(r^{'})\frac{\partial^2\tilde{\psi}_k(r^{'})}{\partial r^{'2}} + b(r^{'})\frac{\partial\tilde{\psi}_k(r^{'})}{\partial r^{'}} = -r^2\tilde{\xi}_k(r^{'}) \tag{A.6}$$

This equation may be discretized applying the second-order three point difference operators given in equation A.7a and A.7b.

$$\frac{\partial\tilde{\psi}_k(r^{'})}{\partial r^{'}} \approx \frac{\tilde{\psi}_k(r^{'}_{j+1}) - \tilde{\psi}_k(r^{'}_{j-1})}{2\Delta r^{'}} \tag{A.7a}$$

$$\frac{\partial^2\tilde{\psi}_k(r^{'})}{\partial r^{'2}} \approx \frac{\tilde{\psi}_k(r^{'}_{j+1}) - 2\tilde{\psi}_k(r^{'}_{j}) + \tilde{\psi}_k(r^{'}_{j-1})}{(\Delta r^{'})^2} \tag{A.7b}$$

Introducing the above approximations into equation A.6 yields

$$(a_j - \frac{b_j}{2})\tilde{\psi}_k(r^{'}_{j-1}) - (k^2 + 2a_j)\tilde{\psi}_k(r^{'}_{j}) + (a_j + \frac{b_j}{2})\tilde{\psi}_k(r^{'}_{j+1}) = -r_j^2\tilde{\xi}_k(r^{'}) \tag{A.8}$$

To complete the linear system, boundary conditions at the inner and outer boundaries must be introduced. At the cylinder surface the Dirichlet boundary condition, equation A.9, is introduced.

$$\tilde{\psi}_k(r^{'}_0) = 0 \tag{A.9}$$

To treat the Neumann boundary condition at the outer boundary accurately, we apply a second order backward difference scheme.

$$\frac{\partial\tilde{\psi}_k(r^{'})}{\partial r}\Big|_{N_{r-1}} = -\tilde{u}_{\theta,N_{r-1}} \approx \frac{1}{2}\frac{dr^{'}}{dr}\Big|_{N_{r-1}}\Big(\tilde{\psi}_k(r^{'}_{N_{r-3}}) - 4\tilde{\psi}_k(r^{'}_{N_{r-2}}) + 3\tilde{\psi}_k(r^{'}_{N_{r-1}})\Big) \tag{A.10}$$

which implies

$$\tilde{\psi}_k(r^{'}_{N_{r-1}}) \approx \frac{2\tilde{u}_{\theta,N_{r-1}}}{3}\frac{dr}{dr^{'}}\Big|_{N_{r-1}} - \frac{1}{3}\tilde{\psi}_k(r^{'}_{N_{r-3}}) + \frac{4}{3}\tilde{\psi}_k(r^{'}_{N_{r-2}}) \tag{A.11}$$

Here, the complex Fourier coefficients $\tilde{u}_\theta$ are defined in the same manner as equation A.5 and N_{r-1} is the radial position of the outer boundary.

Equation A.8, A.9 and A.11 result in the resolution of N_θ tridiagonal linear systems of size $(N_r - 1) \times (N_r - 1)$, one for each harmonic mode k. However, since both ψ and ξ are real functions the complex Fourier coefficients are related by equation A.12a and A.12b,

$$\tilde{\psi}_{N_{\theta-k}} = \tilde{\psi}^{*}_{N_k} \tag{A.12a}$$

$$\tilde{\xi}_{N_{\theta-k}} = \tilde{\xi}^{*}_{N_k} \tag{A.12b}$$

for $k = 0, 1, 2..., N_\theta - 1$, where $*$ denotes the complex conjugate. Thus it is only needed to solve the linear systems for the $N_\theta/2 + 1$ first modes, obtaining the $N_\theta/2 - 1$ last modes by equation A.12a and A.12b. Once the Fourier coefficients are known, the nodal values of ψ and ξ are obtained by performing the inverse Fourier Transform given in equation A.4a and A.4b.

Appendix B: Calculation of the velocity

The velocity in polar coordinates is given by equation B.1.

$$\vec{u} = \frac{1}{r}\frac{\partial\psi}{\partial\theta}\vec{r} - \frac{\partial\psi}{\partial r}\vec{\theta} \tag{B.1}$$

Since $\psi(r^{'},\theta)$ is periodic in the azimuthal direction, with period 2π, we can approximate it by the truncated Fourier series given in equation B.2.

$$\psi(r^{'},\theta) = \frac{1}{N_\theta}\sum_{k=0}^{N_\theta-1}\tilde{\psi}_k(r^{'})e^{ik\theta} \tag{B.2}$$

Here where i is the imaginary number defined as $i^2 = -1$, $\tilde{\psi}_k$ is the k^{th} complex Fourier coefficients of ψ, $\theta_j = 2j\pi/N_\theta$ and N_θ is the number of grid points in the azimuthal direction. Derivation of both sides of equation B.2 with respect to θ yields the relations between the complex Fourier coefficients and the derivative ψ_θ in equation B.3.

$$\frac{\partial\psi(r^{'},\theta)}{\partial\theta} = \frac{1}{N_\theta}\sum_{k=0}^{N_\theta-1}\tilde{\psi}_k(r^{'})ike^{ik\theta} \tag{B.3}$$

After calculating the first term, ψ_θ, there remains to calculate the tangential velocity component. Consistent with the solution of the Poisson equation, a second order central difference scheme is applied to approximate the radial derivative of ψ as in equation B.4, without consideration of the boundary nodes.

$$\frac{\partial\psi(r^{'},\theta)}{\partial r}\Big|_{r_j^{'},\theta_k} = \frac{1}{2}\frac{dr^{'}}{dr}\Big|_{r_j^{'}}\Big(\psi(r_{j+1}^{'},\theta_k) - \psi(r_{j-1}^{'},\theta_k)\Big) \tag{B.4}$$

On the cylinder surface the tangential velocity cannot be obtained by a central difference scheme, since it would imply a non zero normal velocity along the body contour. Then a second order forward difference scheme is used as in equation B.5.

$$\begin{aligned}\frac{\partial\psi(r^{'},\theta)}{\partial r}\Big|_{r_0^{'},\theta_k} &= \frac{1}{2}\frac{dr^{'}}{dr}\Big|_{r_0^{'}}\Big(-3\psi(r_0^{'},\theta_k) + 4\psi(r_1^{'},\theta_k) - \psi(r_2^{'},\theta_k)\Big)\\ &= \frac{1}{2}\frac{dr^{'}}{dr}\Big|_{r_0^{'}}\Big(4\psi(r_1^{'},\theta_k) - \psi(r_2^{'},\theta_k)\Big)\end{aligned} \tag{B.5}$$

At the outermost ring the boundary condition may be used directly.

For convenience, the velocity at each node of the mesh is expressed in Cartesian coordinates according to equation B.6.

$$\begin{aligned} u_x &= \cos\theta u_r - \sin\theta u_\theta \\ u_y &= \sin\theta u_r + \cos\theta u_\theta \end{aligned} \tag{B.6}$$

Then the velocity at each vortex particle is obtained by bi-linear interpolation in equation B.7, as illustrated in Figure B1.

$$\vec{u}_l = A_{j,k} \cdot \vec{u}_{j,k} + A_{j+1,k} \cdot \vec{u}_{j+1,k} + A_{j,k+1} \cdot \vec{u}_{j,k+1} + A_{j+1,k+1} \cdot \vec{u}_{j+1,k+1} \tag{B.7}$$

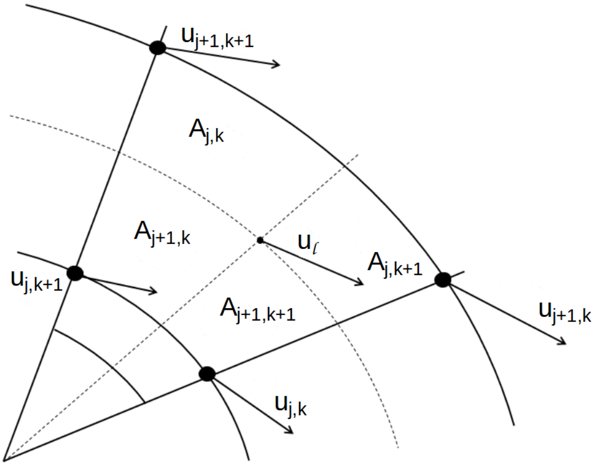

Figure B1: Bi-linear interpolation of the nodal velocities

Appendix C : Definition of the computational domain

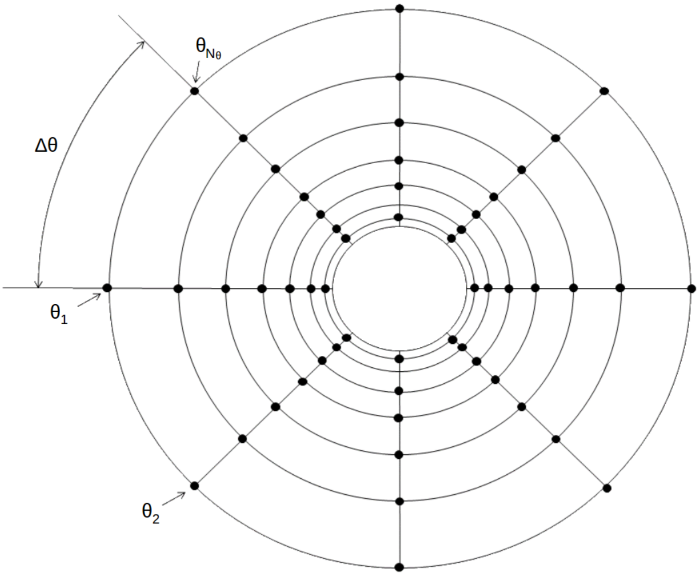

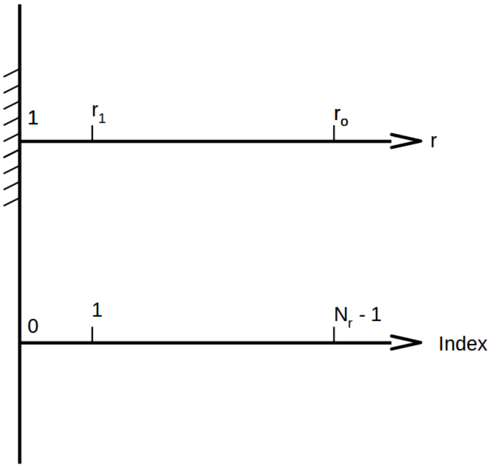

Appendix D : Flow visualization of impulsively started flow past a circular cylinder

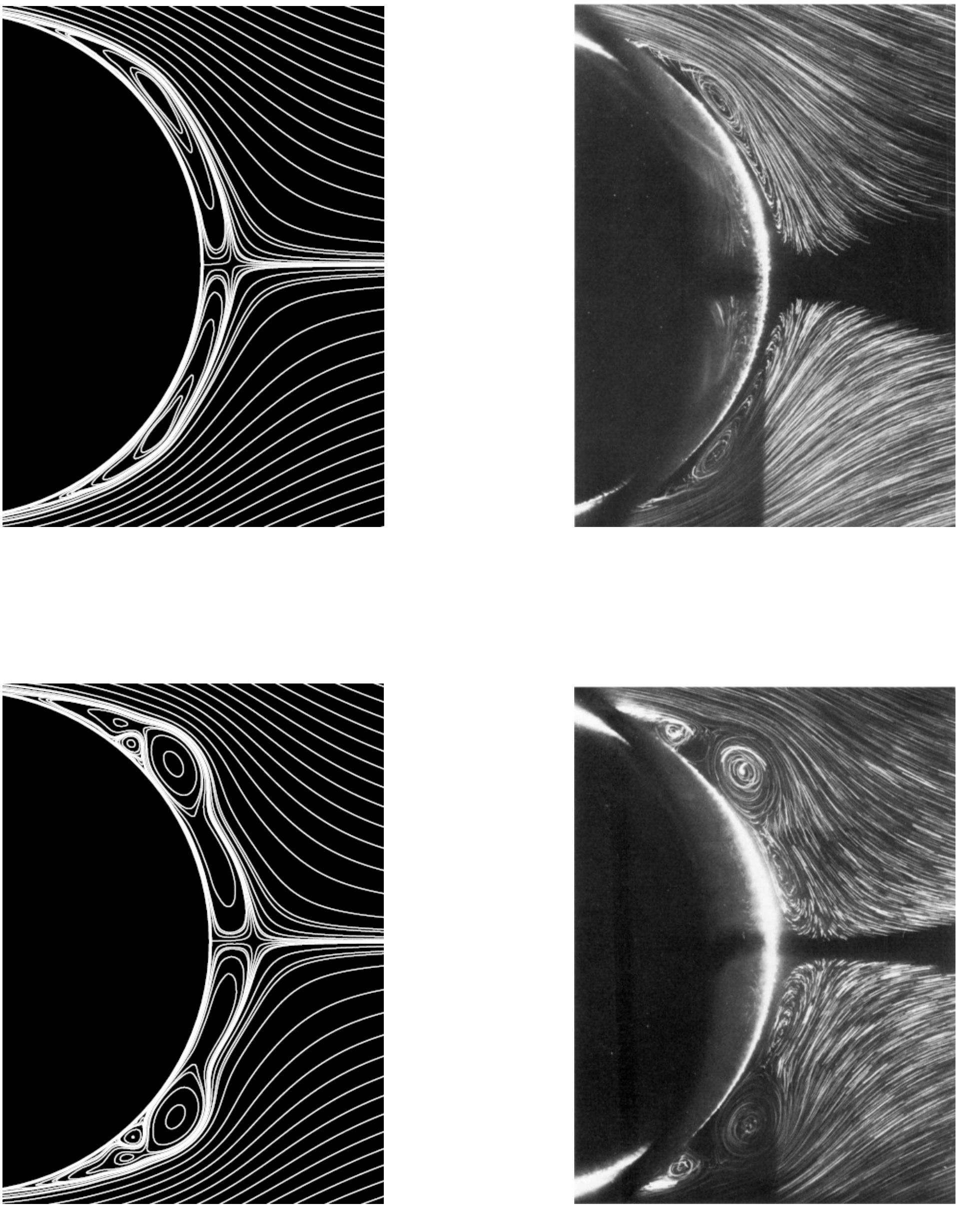

For caption see next page

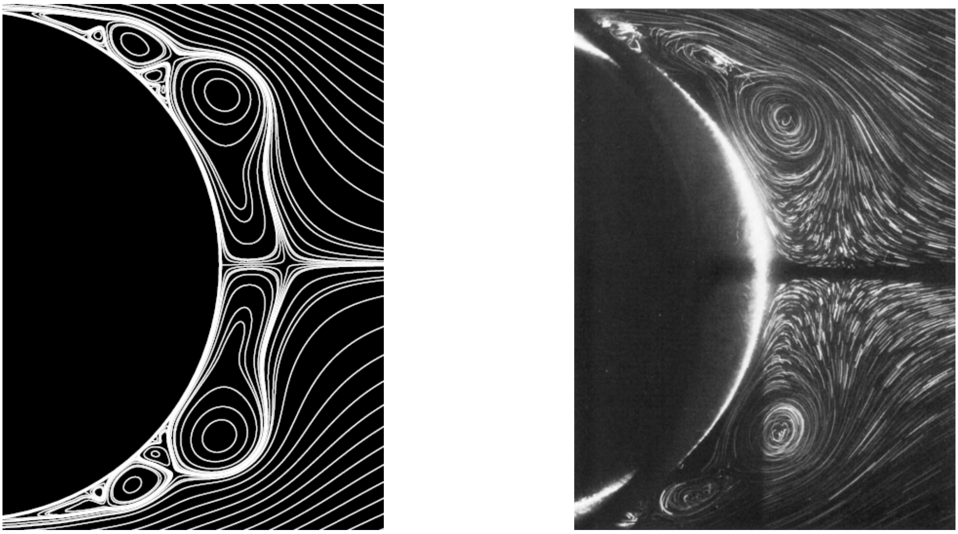

Figure D1: Comparison of the streamlines from the VIC program (left) with the experimental flow visualization of Bouard and Coutanceau (1980) (right) at $Re = 9500$ and $\tilde{t} = 0.75$, 1.00 and 1.25

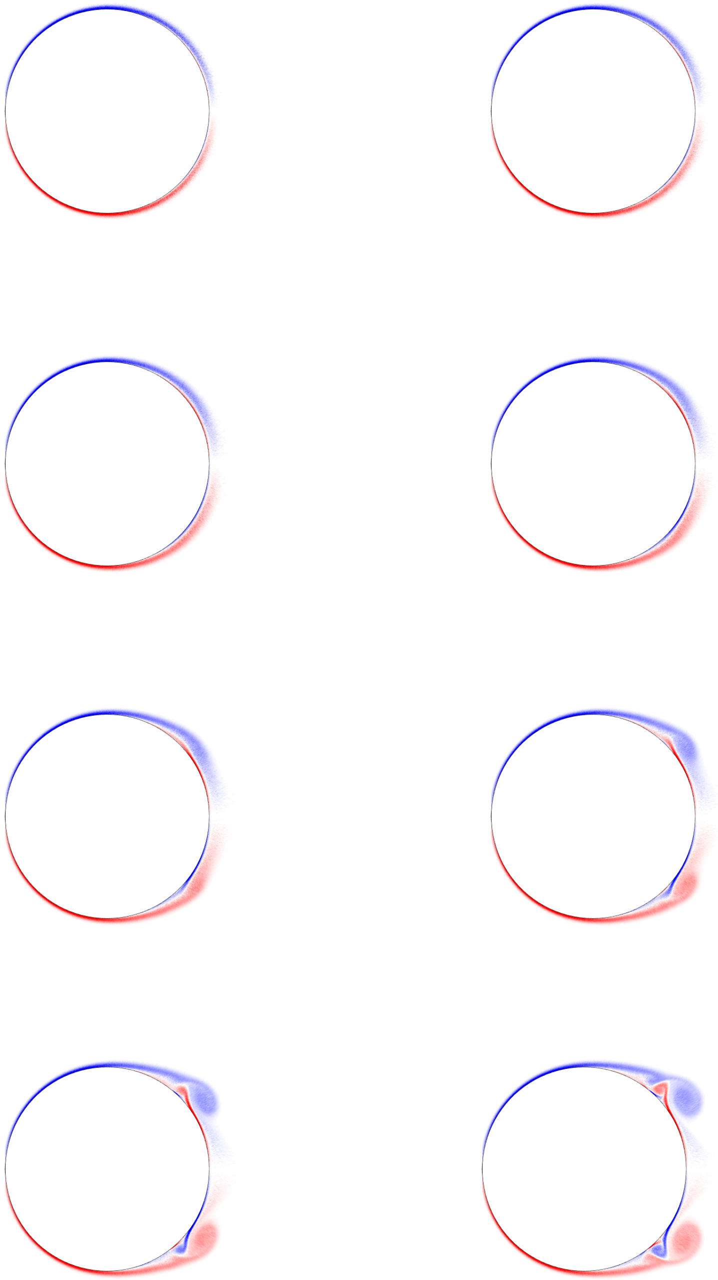

For caption see next page

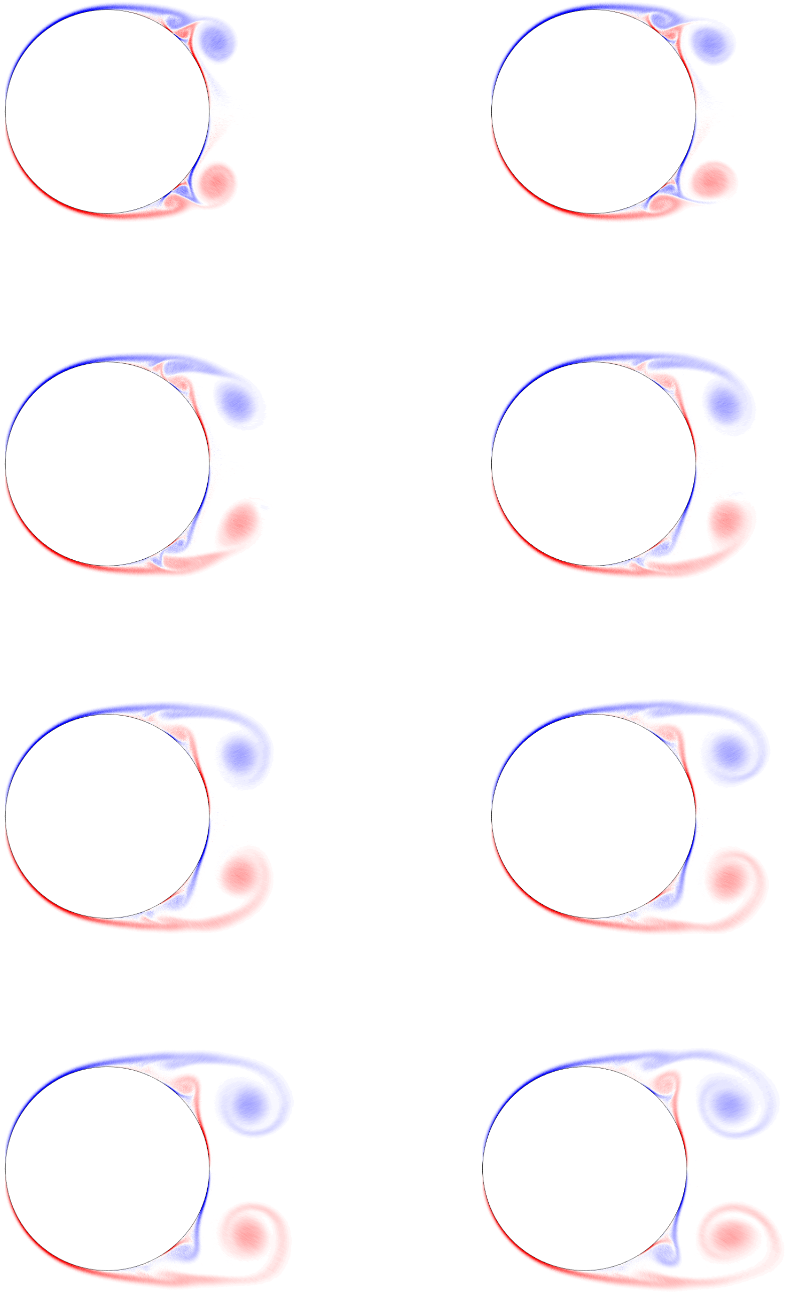

Figure D2: Vorticity field around a cylinder in an impulsively started flow at $Re = 5000$. $\tilde{t} \leqslant 2.5$

Appendix E : Flow visualization for mono-harmonic flow past a circular cylinder

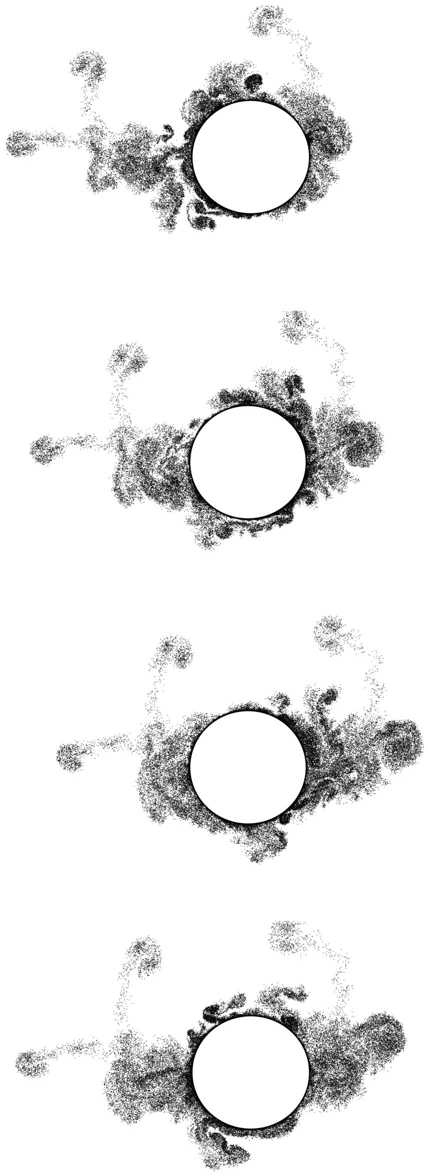

For caption see next page.

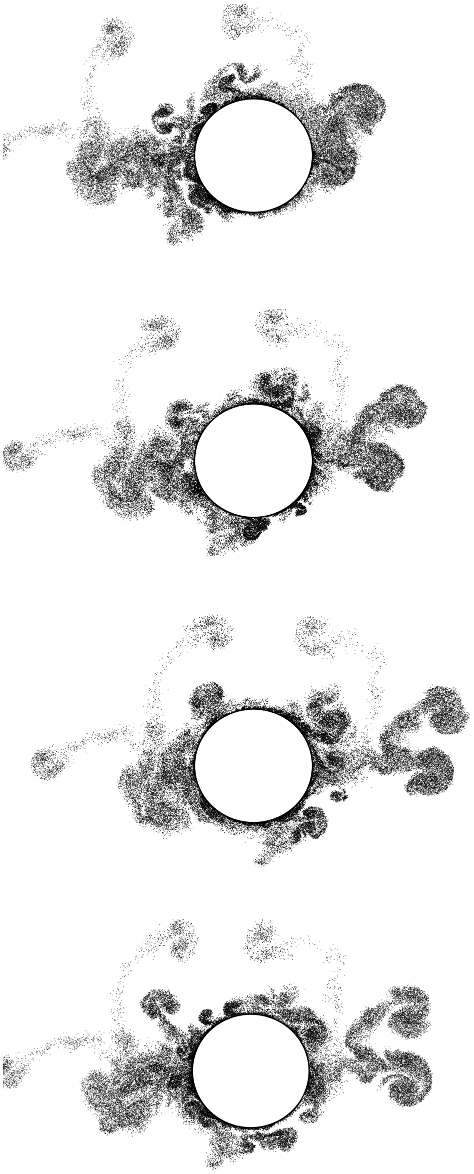

Figure E1: Visualization of flow using point vortex positions at $KC = 2$ and $\beta = 5000$.

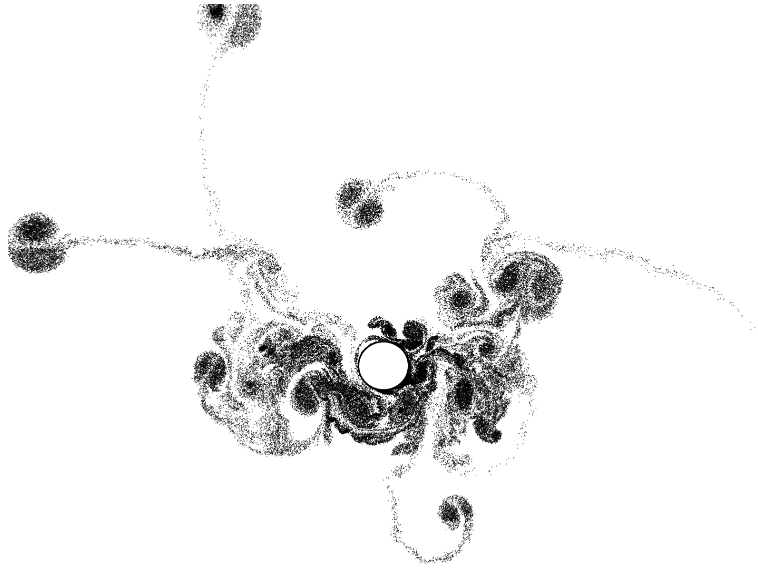

For caption see next page.

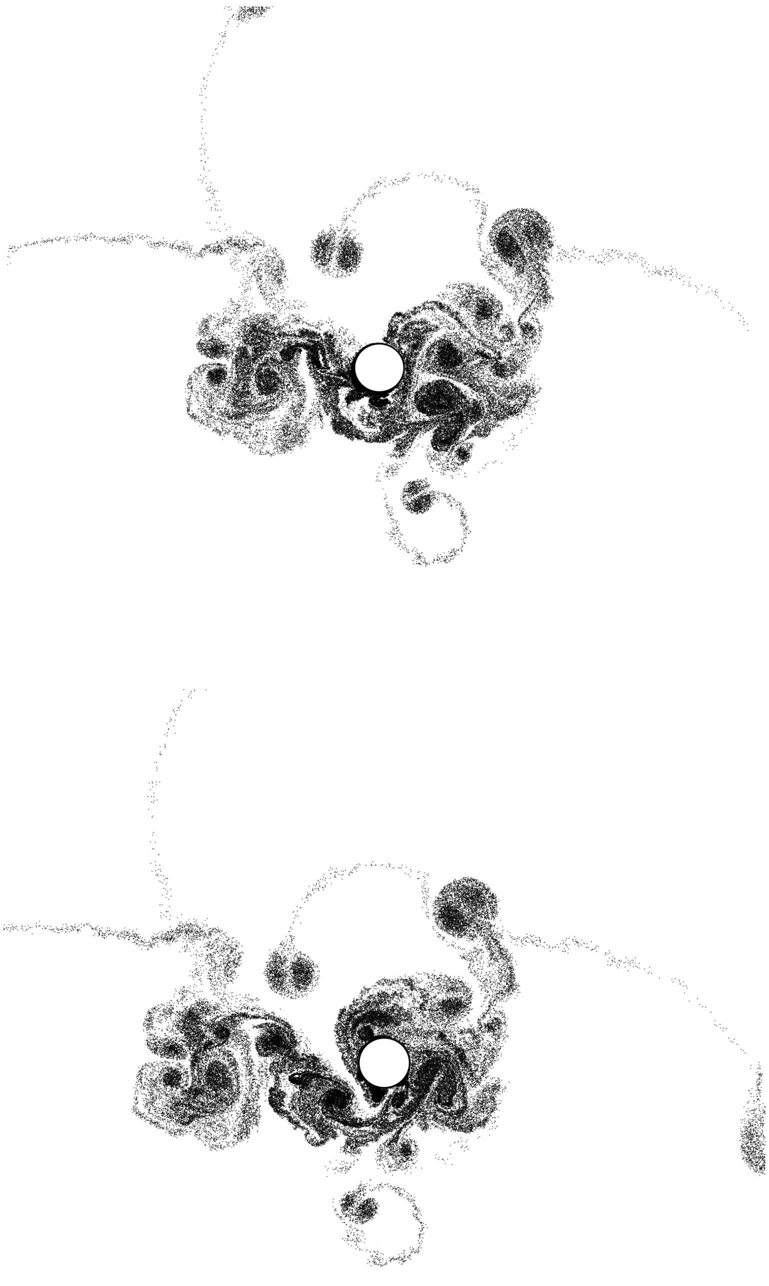

Figure E2: Visualization of flow using point vortex positions at $KC = 6$ and $\beta = 1650$.

For caption see next page.

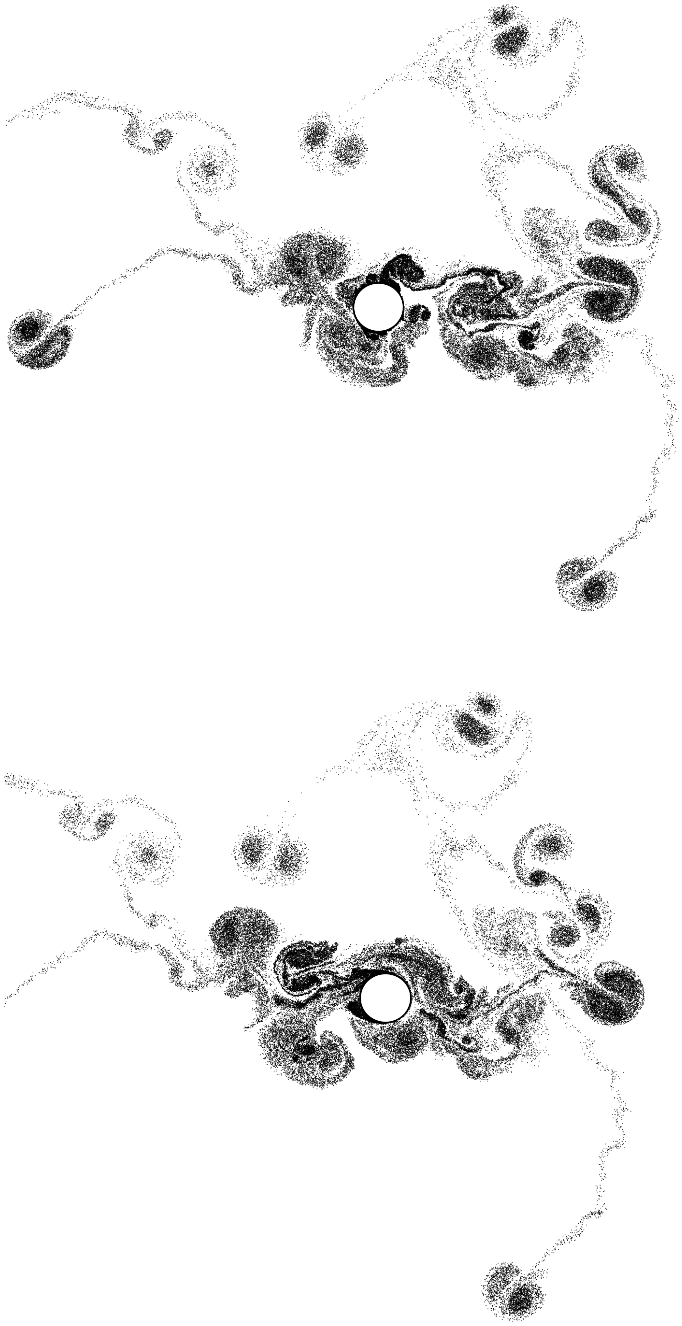

Figure E3: Visualization of flow using point vortex positions at $KC = 8$ and $\beta = 1250$.

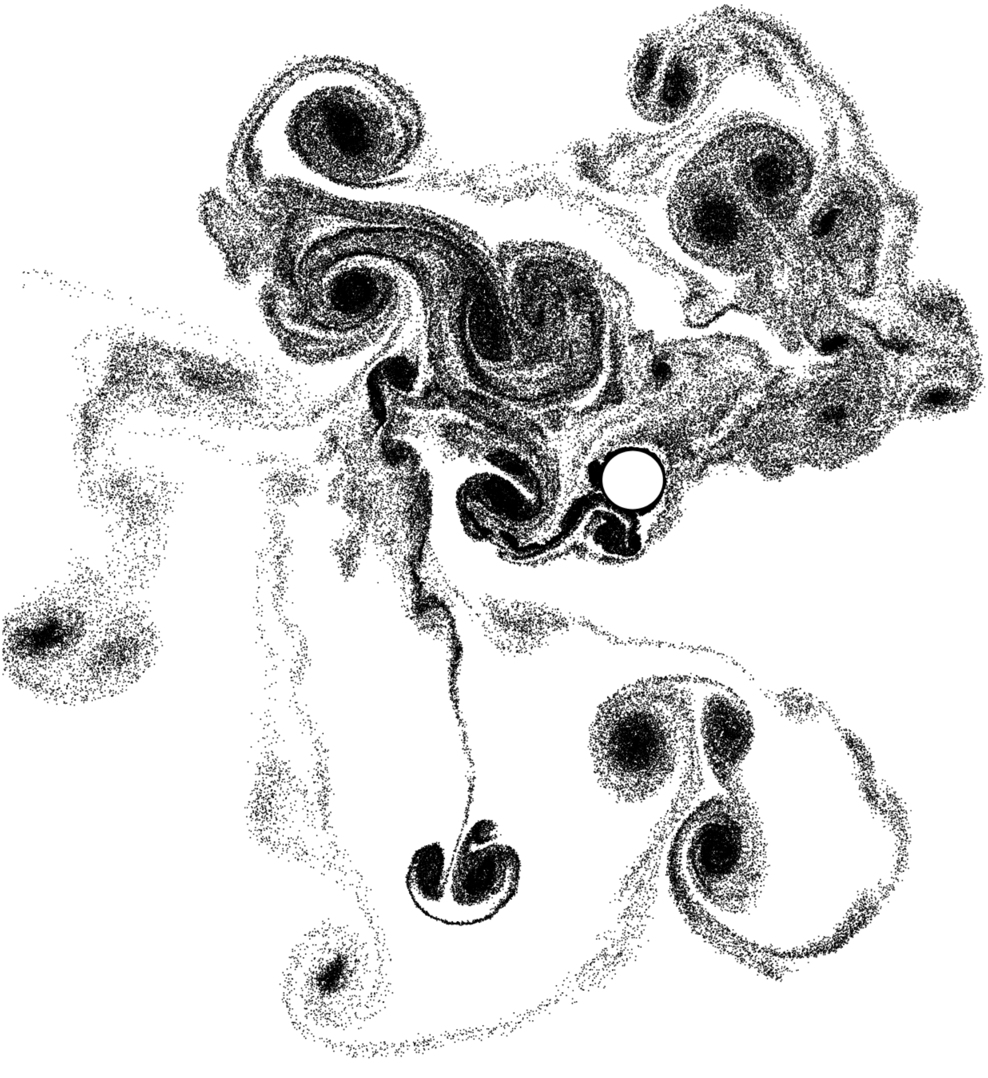

For caption see page 104.

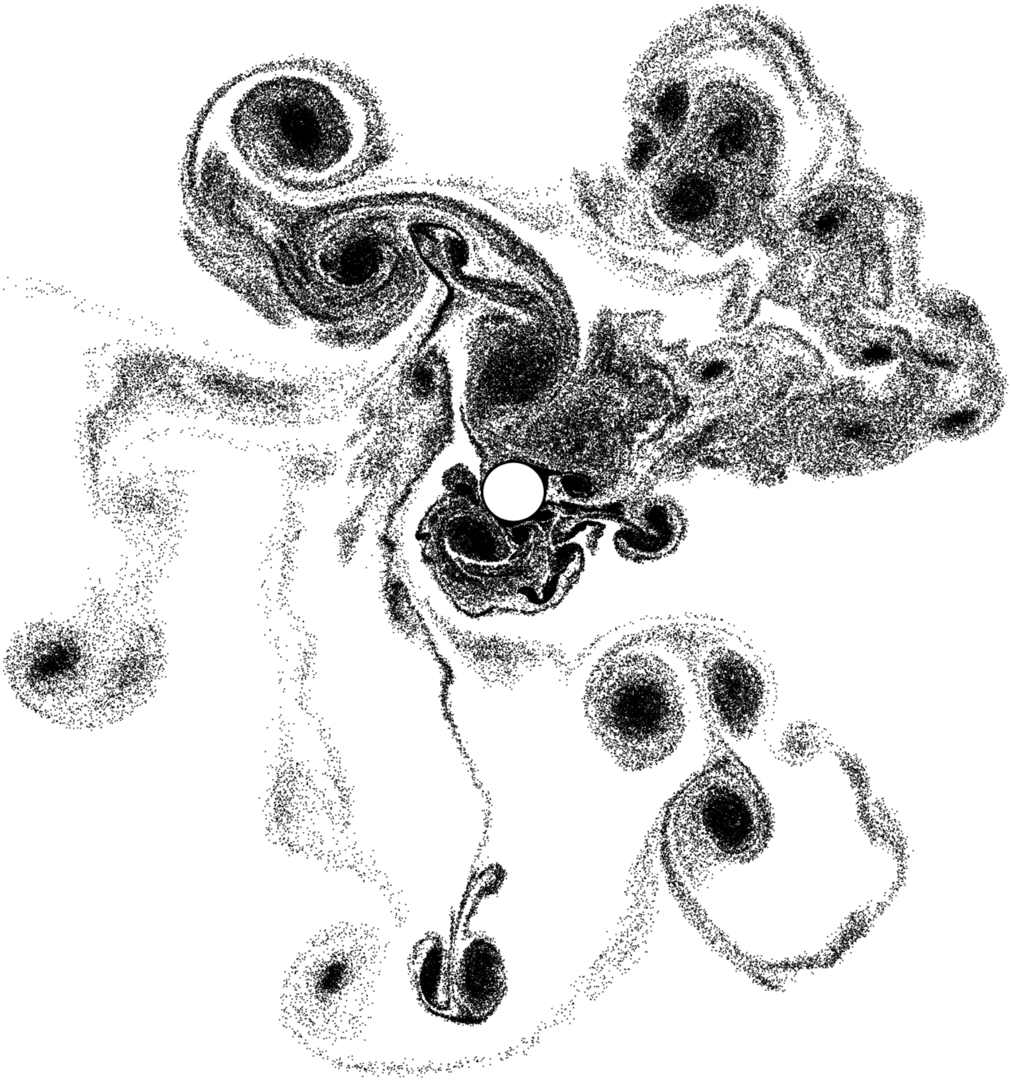

For caption see page 104.

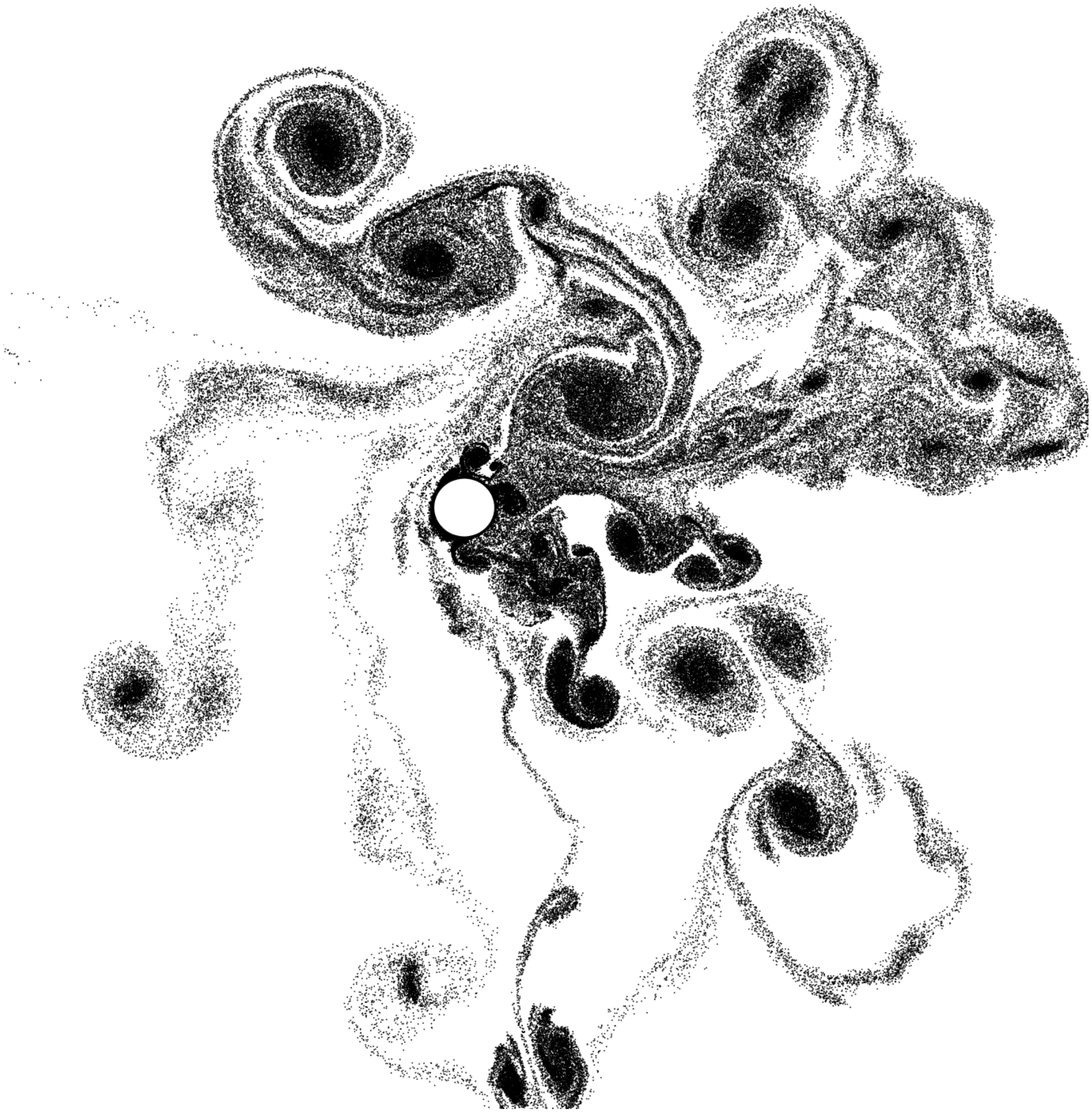

For caption see page 104.

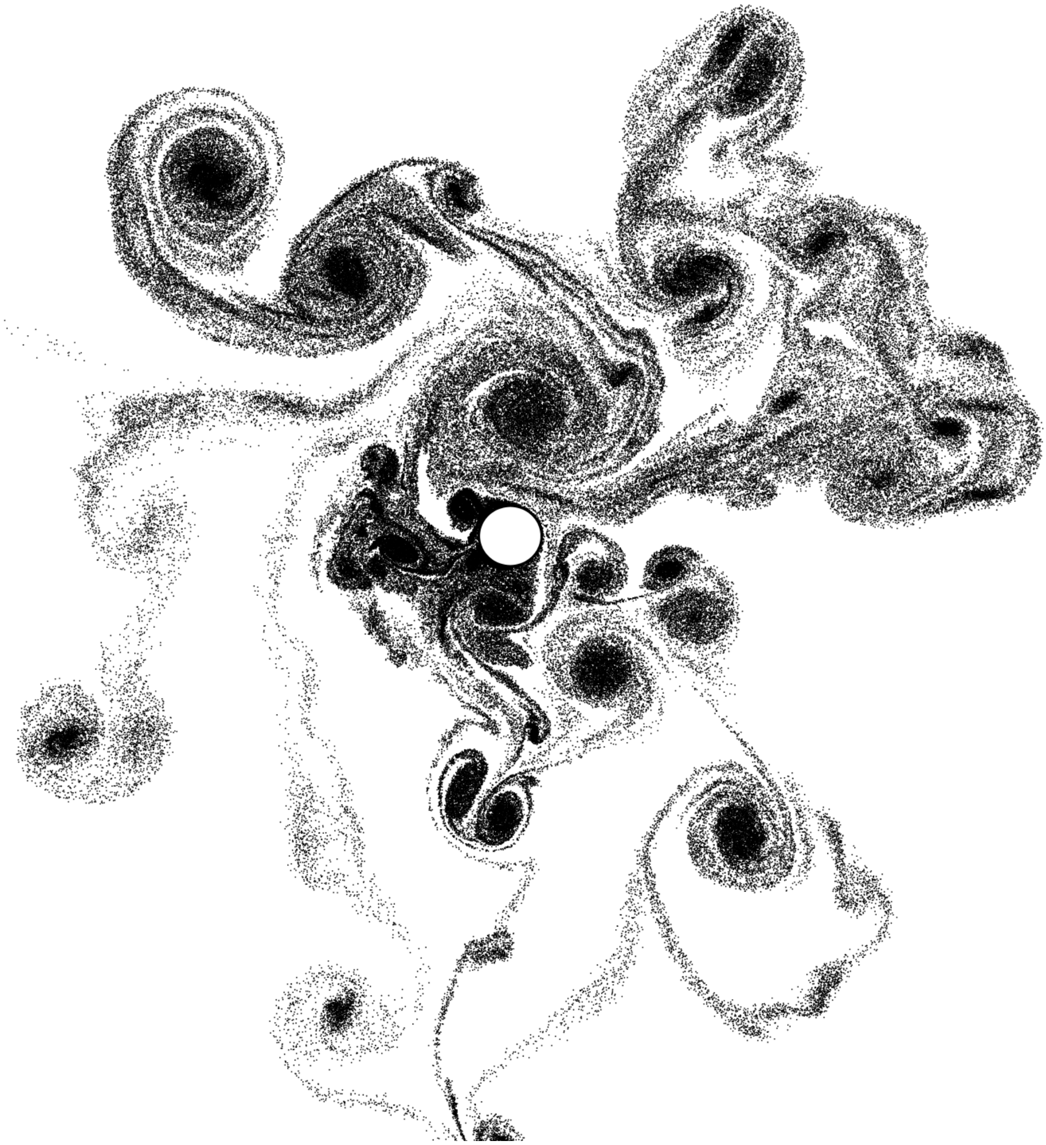

Figure E4: Visualization of flow using point vortex positions at $KC = 12$ and $\beta = 850$.

Appendix F : Load harmonics for $h/a = 5.51$

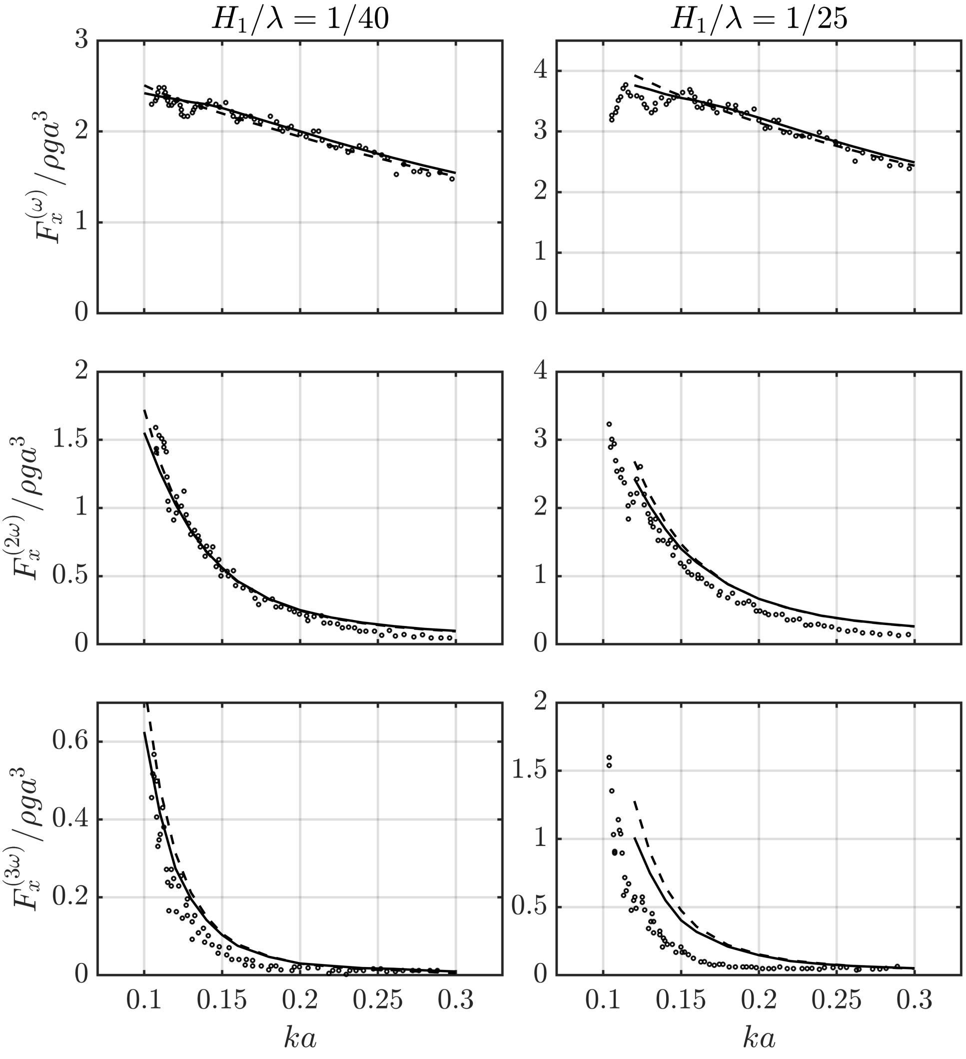

Figure F1: Horizontal force amplitude of the first three harmonics due to regular waves as a function of dimensionless wave number ka for wave steepnesses 1/40 and 1/25. Water depth $h/a = 5.51$. (- - - - -), FNV theory; (———); combined VIC-FNV method; ○, experimental measurements (Kristiansen and Faltinsen (2017))

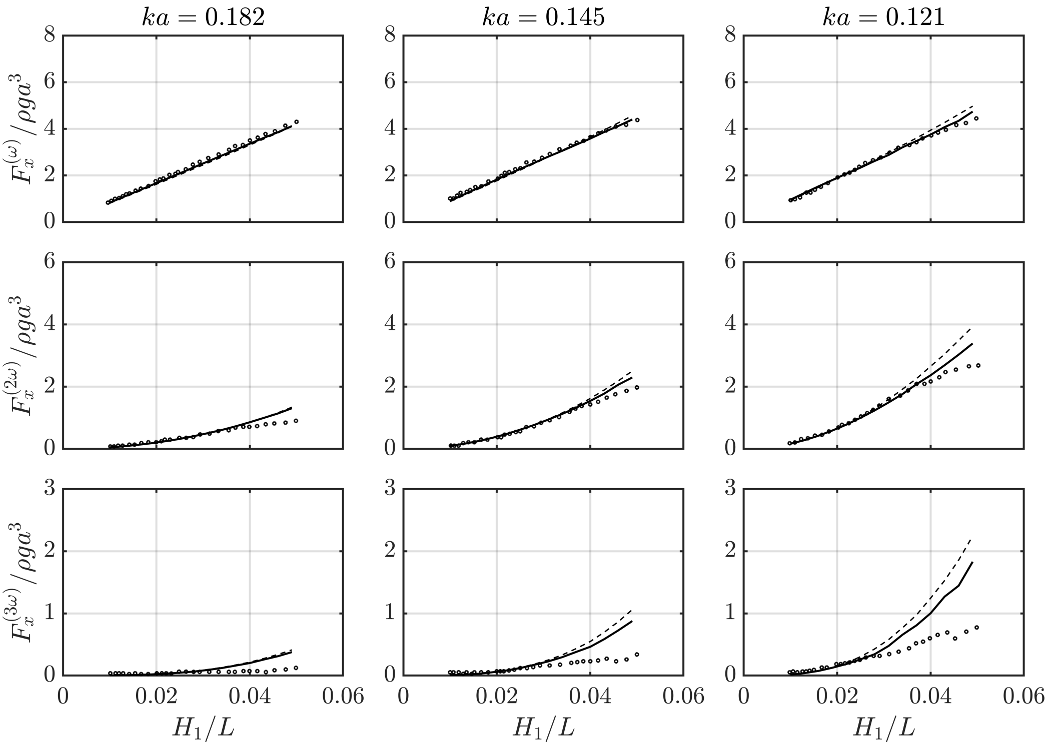

Figure F2: Amplitudes of the first three harmonics of the horizontal force due to regular waves at water depth $h/a = 5.51$ versus linear wave steepness at three non-dimensional wave numbers. (- - - - -), FNV theory; (———), Combined VIC-FNV method; ○, experimental measurements (Kristiansen and Faltinsen (2017)).

Appendix G : Effect of Reynolds number

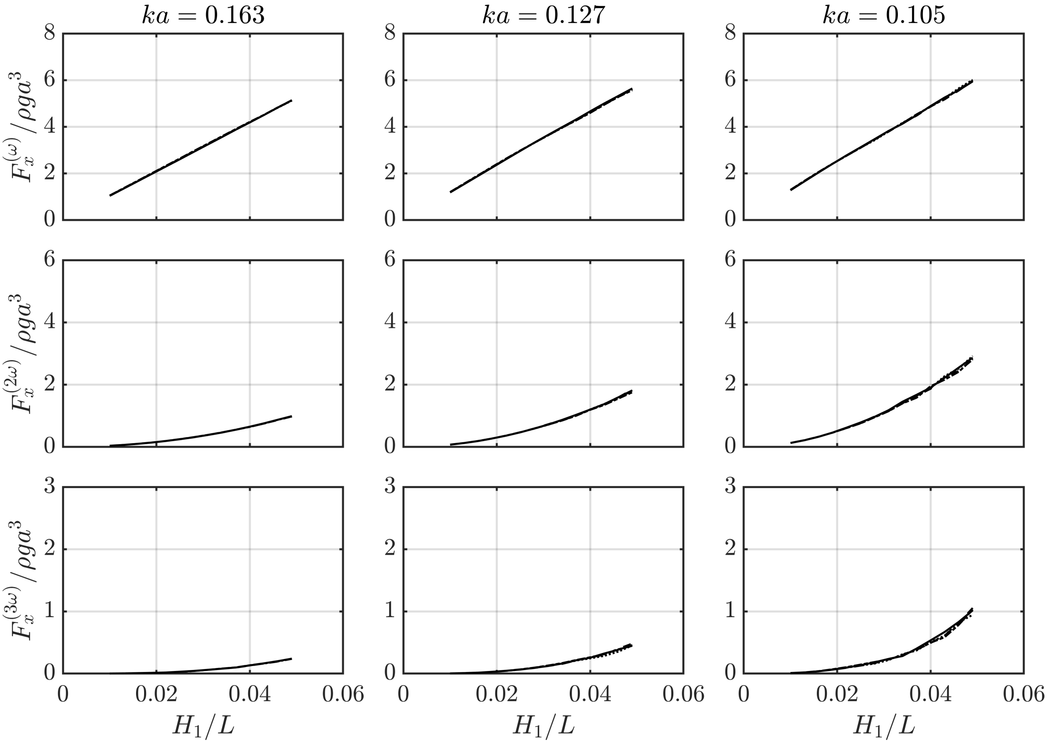

Figure G1: Effect of Reynolds number on the amplitude of the first three harmonics of the horizontal force due to regular waves at water depth $h/a = 7.78$ versus linear wave steepness at three non-dimensional wave numbers. (———), $v_s = 2.59 \cdot 10^{-5}$; (- - - - -), $v_s = 5.18 \cdot 10^{-5}$; (⋯⋯⋯), $v_s = 1.04 \cdot 10^{-4}$; (-·-·-·-·), $v_s = 2.07 \cdot 10^{-4}$.